Ultrasound Speckle Tracking and Color Doppler Elastography for Quantitative Tissue Assessment

著者	Norma Hermawan
学位授与機関	Tohoku University
学位授与番号	11301甲第20135号
URL	http://hdl.handle.net/10097/00135772

Ultrasound Speckle Tracking and Color Doppler Elastography for Quantitative Tissue Assessment

TOHOKU
UNIVERSITY

A dissertation submitted in partial fulfillment
for the degree of Doctor of Philosophy

by

Norma Hermawan

Graduate School of Biomedical Engineering

Tohoku University

2021

Abstract

This dissertation describes an implementation of speckle tracking algorithm for quantitative tissue assessment with clinical application in orthopedics for identifying Adhesive Capsulitis (AC) disease, and the method of mechanically induced shear wave elastography with a color Doppler imaging. The implemented speckle tracking software was capable of visualizing layers of tissue in the shoulder based on their velocity during a movement. In addition, Adhesion Index (AdI) quantity was introduced as a novel measure of shoulder adhesion, which was calculated from the velocity difference between subscapularis and the deltoid muscle of the shoulder. The result suggested that motion limitation on the AC patient could be explained by the AdI because the patient with restricted motion encountered a noticeable adhesion on the subscapularis. On the other part, a method of color Doppler elastography by mechanically induced shear wave is implemented. The capability of the method in resolving elasticity map of homogeneous and non-homogeneous phantom is demonstrated. Since it does not need a precise control to the imaging parameter, it can be implemented in standard commercially available ultrasound (US) machines. The measurement results suggested that the accurate estimation of the shear wave velocity was obtained. The merits of speckle tracking and mechanically induced shear wave elastography methods are that quantitative parameters of tissue character are obtained non-invasively and that all measurement data are obtainable by a standard ultrasound machine. Clinical application in the field of orthopedic surgery is desired in near future.

和文アブストラクト

この論文では、癒着性関節包炎（AC）疾患を特定するための整形外科での臨床応用を伴う定量的組織評価のための実装スペックル追跡アルゴリズム、およびカラードプライメージングを使用した機械的に誘発されたせん断波エラストグラフィの方法について述べている。実装されたスペックルトラッキングソフトウェアは、運動中の速度に基づいて肩の組織の層を視覚化することができ、肩甲下筋と肩の三角筋の間の速度差から計算できる肩甲下筋の新しい尺度として、癒着指数（AdI）量を提案した。肩の動きが制限されている患者は、肩甲下筋に顕著な癒着が認められており、AC 患者の運動制限が AdI によって定量化できることが示された。カラードプラエラストグラフィーは、機械的に誘発されたせん断波を市販の超音波診断装置により可視化する方法で、装置固有の開示されていないパラメータを制御する必要がないため、一般的な市販の超音波診断装置に実装可能である。均質および不均質ファントムを用いた計測により、せん断波速度の正確な推定が得られることが示唆された。超音波スペックルトラッキングおよびカラードプラエラストグラフィーは、非侵襲的に定量的組織性状診断が可能で、すべての測定データが一般的な超音波装置で取得できるので、整形外科領域における将来性が期待される。

Table of Contents

List of Figures

List of Tables

Abbreviations

1^{st} ER	First External Rotation
2^{nd} ER	Second External Rotation
3^{rd} ER	Third External Rotation
AC	Adhesive Capsulitis
AdI	Adhesion Index
a.k.a.	also known as
ARFI	Acoustic Radiation Force Impulse
BBGDS	Block-Based Gradient Descent Search
CDI	Color Doppler Imaging
CFI	Color Flow Imaging
CHL	Coracohumeral Ligament
CW	Continuous Wave
DS	Diamond Search
Eq	Equation
ER	External Rotation
Etc	et cetera – and the rest
GUI	Graphical User Interface
i.e.	id est – that is
IR	Internal Rotation
LDSP	Large Diamond Search Pattern
MAD	Mean Absolute Difference
MRI	Magnetic Resonance Imaging
MSD	Mean Squared Difference

NCC	Normalized Cross-correlation
PRF	Pulse Repetition Frequency
PRI	Pulse Repetition Interval
PVA	Polyvinyl Alcohol
RF	Radio Frequency
ROI	Region of Interest
ROM	Range of Motion
SAD	Sum of Absolute Difference
SDSP	Small Diamond Search Pattern
SSC	Subscapularis
TSS	Three Step Search
US	Ultrasound

Symbols

c_s	speed of source
c_{obs}	speed of observer
d_0	object distance
$E(x, y, t)$	image brightness at the point *(x, y)* in the image plane at time *t*
E_t	partial derivative of image brightness with respect to time *t* axis
E_x	partial derivative of image brightness with respect to spatial *x* axis
E_y	partial derivative of image brightness with respect to spatial *y* axis
f	frequency
f'	precepted frequency
f''	reflected frequency
f_d	Doppler shift in frequency
$f(t)$	a continuous function of time *t*
$\overline{f(t)}$	complex conjugate of *f(t)*
$g(t)$	a continuous function of time *t*
PRF	pulse repetition frequency
T_{PRF}	the time between transmit pulses
u	velocity to the x direction
v	velocity to the y direction
v_D	flow velocity
θ_{th}	threshold angle
v_{th}	threshold velocity

Constants

Density of soft tissue	$\rho_t = 1.1\ g/cm^3$
Euler's number	$e = 2.71828$
Sound speed in a soft tissue	$c_0 = 1540\ m/s$

Chapter 1

Introduction

This dissertation discusses the implementation of speckle tracking to quantitatively assess the shoulder ligament movement, and the implementation of color Doppler method in a commercial ultrasound machine to measure elasticity of biological tissue. In this introduction, I will explain a brief background of the study, objectives, and the writing structure of the dissertation.

1.1 Background

The "tissue characterization" is a general term in medical diagnostics. It may include an attempt to find an empirical evidence or even just a result of fundamental experiments which may not directly point to the diagnostic indices. This field of knowledge is an important part in the biomedical engineering. The more specific tissue assessment constitutes an in-depth objective assessment of the movement functional and strength of the organ or tissues that is required in body movement.

The use of tissue characterization such us in retrieving myocardial velocity and deformation data has been done by Doppler derived method for a long time. The problem with Doppler method in the dynamic analysis is its angle-dependency to the asserted image line. This dimension limitation reduces the measurement reproducibility between studies and observers. As a result, analyzing a tissue deformation or velocity would be complicated and time-consuming. The two-dimension analysis in contrast would reveals more information and resolve angle-dependency problems. Different methods have been developed such as multiple-beam Doppler [1], speckle tracking [2], and sound field spatial modulation [3]. The advance of modern ultrasonography brought those methods feasible for practical research and commercial implementation.

Elastography on the other hand has contributed significant role in tissue assessment since bio-tissues properties may be associated with many diseases. The quantitative measurement is preferable than the previously wide used palpation as a qualitative assessment of the shear stiffness of the tissue which rely on the experience of clinician. Color Doppler techniques were introduced along the other method as a non-invasive quantitative method which retains the accuracy and create the map of elasticity with available apparatus.

One of application of the tissue characterization is in the identification of restricted shoulder movement disease such as Adhesive Capsulitis (AC). In the AC, pain, stiffness, and loss of motion range of the shoulder are main clinical representation in addition to the other symptoms. In a random survey to 9,696 adults of working age, adhesive capsulitis has affected 8.2% among men and 10.1% among women of the population [4]. The etiology of AC is not completely understood. However, its development could be slowed down and even terminated if its severity can be detected accurately and the appropriate therapy is given accordingly [5].

Most of the AC diagnosis are based on clinical evaluation since specific laboratory tests or radiological markers are limited. Its clinical presentation is not specific and often mimics several other painful disorders. X-rays of the AC are usually used to rule out the other cause such as humeral fractures, tendon calcification, osteoarthritis. Magnetic Resonance Imaging (MRI) may show a slight thickening in the joint capsule and the coracohumeral ligament (CHL) as well as helping identify rotator cuff tears [6]. Sonography often excluded AC diagnosis due to lack of specific diagnostic criteria. However, a previous study has shown the prospective of sonography efficacy for diagnosis of AC. It successfully visualized the thickened CHL and access dynamic parameters on the AC patients [7]. Synovial membrane adhesion and shortening have a chance to develop during immobilization of joints [8]. Such adhesion and shortening also induce limited Range of Motion (ROM) [9]. In the previous research, ligaments adhesion [10] and distinct elasticity [11] are shown to have a correlation with the adhesive capsulitis symptoms and both quantities can be visualized by ultrasonography technique.

The ultrasonography is usually preferable since it is inexpensive and non-invasive procedure. The advance of ultrasonography technique such as ultrasound speckle tracking and the color Doppler shear wave elastography may be valuable tools for identifying the disease more precisely.

1.2 Research Objective

The ultimate purpose of the study is to provide reliable methods to perform quantitative assessments of shoulder and provide prognostic information of tissue condition such as ligament contracture. The correlation of tissue condition and the severity of the disease symptoms such as in AC is investigated which in turn may help physician to diagnose and determine the recommended therapy.

In order to realize the objective, two methods to assess tissue health are discussed thoroughly. The first method is discussed in the implementation of speckle tracking for quantifying muscle adhesion which is linked to the AC symptoms. The second method is explained by color Doppler shear wave elastography which is implemented in a commercial ultrasound machine.

1.3 Organization

This dissertation is divided into five chapters. Chapter 1 is Introduction, which describe the objective of the research and its impact. In chapter 2, Speckle tracking method in ultrasonography is discussed thoroughly. The discussion includes the explanation on the nature of ultrasound speckles, the theoretical basis of motion evaluation, various search algorithm and software implementation for shoulder ligament visualization. In Chapter 3, Adhesion Index (AdI) quantity and its measurement method by speckle tracking is introduced. The method is tested to quantify shoulder muscles adhesion in subjects with idiopathic and secondary AC. Chapter 4 discusses about elastography method by color Doppler technique. The theoretical background of using Doppler method for observing a shear wave is explained, including the proposed novel method of elastography by using a commercial ultrasound machine. Finally, the dissertation is concluded and summarized in Chapter 5.

Chapter 2

Diagnostic Ultrasound Speckle Tracking

Speckle tracking is one of a method for tissue characterizing by tracking the motion of ultrasound speckles during a subject movement. In a speckle tracking method, a spatial distribution of gray values which is called speckle pattern constitute the underlying biological tissue such as ligaments. The position of this unique pattern may move following the tissue motion. Tracking this pattern during a tissue movement within 2-D image is the basic principle of the speckle tracking methods.

The speckle tracking techniques are divided into block-matching and optical flow approach. In the block matching approach, the best match of a rectangular patch in the image a frame is sought within a Region of Interest (ROI) in the following frame. The speckle motion is determined based on the maximum similarity of the matching. A map of velocity vector is produced after completing the search on a predetermined ROI.

As an alternative approach, optical flow method makes use of conservation of gray values principles which assuming gray values constancy over time. In this case, the motion of gray values is estimated based on gray value change alongside time and spatial coordinate. Velocity vector cannot be estimated from this principle alone since available parameter is less than required to solve brightness constancy equation which is known as aperture problem. To resolve that, additional parameters such as spatial smoothness and local similarity are introduced which led to many optical flow techniques such as Horn Schunck algorithm [12] and Lucas-Kanade algorithm [13].

Through this chapter, technical explanation about speckle tracking algorithm is described. Block matching speckle tracking fit well with B-mode ultrasound image, thus, it is employed in this research. On the other hand, it still worth to briefly discuss about the optical flow method to give a comparison, even though its application is rather limited for small inter-frame displacement of high-quality images such as MRI. Further discussion about a clinical implementation of speckle tracking to quantitatively access the shoulder motion will be discussed in a separated chapter. Part of this chapter was published in the 2020 42nd Annual International Conference of the IEEE Engineering in Medicine and Biology Society proceeding under a title “Visualization of Shoulder Ligaments Motion by Ultrasound Speckle Tracking Method”.

2.1 The Nature of Ultrasound Speckles

Basically, an ultrasonic imaging is reconstruction of a reflected echo of a transmitted ultrasound pulse. When an ultrasound signal travels in a tissue, it might come across *reflector* or *scatterers*. A reflector is a location within the tissue where ultrasound waves are reflected in a specular fashion. It is formed by tissue transition with different acoustic impedance. On the other hand, scatterers reflect the ultrasound waves in all directions. As a result, the signal that is reflected to the transducer tend to appear weak. It may be formed by a mass with distinct density but smaller than a wavelength. The scatter locations are spreading in the tissue, hence the detected signal by ultrasound transducer is normally a superposition of reflection by multiple scatterers. The different timing between signals makes the constructive or destructive interference on the reflected signals. The constructive superposition will be larger in amplitude, meanwhile the destructive interference will look smaller. The envelope processing to the so-called radiofrequency (RF) signal produces a bright and dark pattern in the image. The spatial distribution of this dark and bright pattern constitutes the constructive and destructive interference due to multiple scatterers in the tissue. The spatial distribution of this dark and bright pattern is commonly defined as speckle.

If the scatterers move along the beam line, the reflection travel time will be increased. However, their relative position within a small scope is fixed so that the interference pattern looks preserved. On the other hand, when the scatterers move perpendicular to the beam line, the particular speckle pattern are moving away. However, when 2-D transducer is used, the speckle pattern is detected by the other beam, as long as the tissue motion is slower than the ultrasound beam motion. A sound velocity 1530 m/s means that tissue motion in the order of cm/s is approximately 10.000 times slower, which is met with the condition. In principle, the preservation of speckle tracking hold when the reflection interference is constant. On the other word, the amplitude and relative time delay between image frame acquisition must be constant. It means that any rotation or deformation as well as out-off plane motion that change the relative position must not happens between acquisitions. Ideally, speckle tracking should be performed with high frame rate images and high-quality images to accurately visualize scatterer motion and avoid image artifacts [14].

2.2 Optical Flow Methods

The first category of tracking the speckle is called optical flow methods. These methods work based on the brightness constancy principle which assumes that surface radiance in a patch is constant over time, which is formalized by

$$\frac{dE}{dt} = 0 \qquad \text{Eq. 1}$$

By chain rule differentiation,

$$\frac{\partial E}{\partial x}\frac{dx}{dt} + \frac{\partial E}{\partial y}\frac{dy}{dt} + \frac{\partial E}{\partial t} = 0 \qquad \text{Eq. 2}$$

If a motion is defined as

$$u = \frac{dx}{dt} \quad \text{and} \quad v = \frac{dy}{dt} \qquad \text{Eq. 3}$$

Then, the object motion can be expressed by an equation with two unknowns

$$E_x u + E_y v + E_t = 0 \qquad \text{Eq. 4}$$

This equation is commonly known as brightness constancy constrain which underly all optical flow methods. Since the equation contains two unknowns, the motion cannot be resolved without introducing additional constraint. As it is initially developed for image compression, the early experiment with the optical flow method is performed to the television frame sequences.

2.2.1 Horn-Schunck method [12]

Horn-Schunck method used smoothness assumption as the second constraint to resolve the motion. This assumption is based on observation on a deformed body where neighboring point will move at similar velocity and smooth variation occurs in whole image. Consequently, the algorithm would be difficult to deal with edge problems. This additional constrain can be implemented by minimizing square of magnitude of the gradient

$$\left(\frac{\partial u}{\partial x}\right)^2 + \left(\frac{\partial u}{\partial u}\right)^2 \quad \text{and} \quad \left(\frac{\partial v}{\partial x}\right)^2 + \left(\frac{\partial v}{\partial u}\right)^2 \qquad \text{Eq. 5}$$

or set the zero value to the Laplacian of u and v,

$$\nabla^2 u = \frac{\partial^2 u}{\partial x^2} + \frac{\partial^2 u}{\partial y^2} \quad \text{and} \quad \nabla^2 u = \frac{\partial^2 v}{\partial x^2} + \frac{\partial^2 v}{\partial y^2} \qquad \text{Eq. 6}$$

In their proposed method, Horn and Schunck decided to use the magnitude of the gradient (Eq. 5) as smoothness measure for their approach. An iterative strategy was implemented to solve the equation pair for all rows and columns of the picture.

2.2.2 Lucas-Kanade method [13]

In contrast to the Horn-Schunck method, the Lucas-Kanade method introduce neighboring approach to resolve the brightness constancy constraint. As an instance, a motion of a pixel is calculated from 3 × 3 neighborhood around the pixel. In that case, 9 linear equations of 2 unknown are set by

$$E_x(x+\delta x, y+\delta y)\cdot u + E_y(x+\delta x, y+\delta y)\cdot v = -E_t(x+\delta x, y+\delta y) \qquad \text{Eq. 7}$$

For

$$\delta x = -1, 0, 1 \quad \text{and} \quad \delta x = -1, 0, 1 \qquad \text{Eq. 8}$$

This system of linear equations can be solved easily by least square method. However, there is a difficult condition when the system of equation is unresolvable, for example when E_x, E_y and E_t are zero for all pixels in the neighborhood. In that case, an exception handler must be implemented.

2.3 Block Matching Algorithm

Another category in the speckle tracking is block matching algorithm. In this algorithm, a square block so-called kernel in a frame is compared with shifted regions of the same size from the previous frame. This procedure is performed repeatedly to a predefined search area. The shift which results in the maximum similarity is selected as the best motion vector for that kernel. Several measures of similarity can be defined such as sum of absolute difference (SAD), mean absolute difference (MAD), mean squared difference (MSD), and normalized cross-correlation (NCC). The vector calculation is repeated for all pixel in a region of interest (ROI) to obtain the in-plane velocity vector field. A dynamic velocity vector field is obtained by repeating this measurement to all frames of the ultrasound image sequence.

2.3.1 Normalized Cross Correlation (NCC)

One of a method to determine similarity between two patches of image is by normalized cross correlation. Correlation is a mathematical operation which is similar with convolution given by Eq. 9.

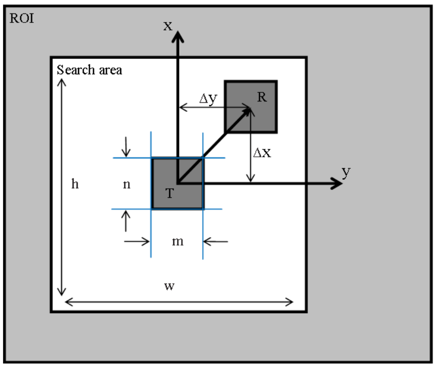

Figure 2.1 Sum of Absolute Differences (SAD) block matching algorithm.

The cross-correlation term is used when the operation is performed between a signal with a template. If operation is matching the signal with itself, it is called autocorrelation. Usually, correlation is used for searching a short pattern a.k.a. feature of a longer signal. When the cross-correlation method is performed in 2-dimensional field, such 2-dimeansional feature can be sought in an area. The cross-correlation output will be highest at places where the image pattern matches the kernel. The normalized cross correlation aligns calculation result in between -1 to 1 value, where 0 means complete uncorrelatedness.

$$[f(t) * g(t)](t) = \left[\overline{f(-t)} * g(t)\right](t) \qquad \text{Eq. 9}$$

2.3.2 Sum of Absolute Difference (SAD)

In contrast to the cross-correlation, the Sum of Absolute Difference (SAD) requires less computation resource since it involves difference operation instead of multiplication. It measures the similarity between image blocks by comparing the intensities in the kernel pixel by pixel. The comparison is done by subtracting each pixel value in a kernel to the corresponding pixel of the paired area and sum the result of calculation for all pixels.

Refer to a SAD block matching illustration in Figure 2.1, the minimum value of SAD over whole searching area determines optical displacement and thus temporal inter-frame velocity vector. In the SAD, equation 1 is called cost function. In this calculation, $w \times h$ is the dimension of the search window, and $m \times n$ is the dimension of the kernel.

$$SAD(\Delta x, \Delta y) = \sum_{i=0}^{m-1} \sum_{j=0}^{n-1} \left| T_{i,j} - R_{i+\Delta x, j+\Delta y} \right| \qquad \text{Eq. 10}$$

$$U = \min_{(\Delta x, \Delta y)} \{SAD(\Delta x, \Delta y)\} \qquad \text{Eq. 11}$$

$$v = r(\Delta x, \Delta y)^T|_U \quad \text{Eq. 12}$$

In this calculation, for $m \times n$ kernel and $w \times h$ search window dimension, there are $(w-m+1) \times (h-n+1)$ possibilities of vector. If all these values are calculated and the best match is determined from the field, it will come into a category called full search block matching algorithm.

2.4 Search Algorithm

The basic block matching algorithm calculates cost function to a whole search area and determines the maximum similarity subsequently. This type of searching strategy is called exhaustive full search block matching algorithm. Despite its high peak signal-to-noise ratio, the method is computationally the most expensive among other search algorithms. The computation requirement increases proportionally to the size of search window. On the contrary, a step search algorithm works by searching for the maximum similarity without trying all possibilities, which in turn reduces the computational requirement significantly. The purpose of search algorithm is to obtain the most efficient search strategy while maintain accuracy of motion detection.

In this section, I have selected four most worthy methods and proposed two novel methods. In general, these four methods can be considered as an example of coarse-to-fine step search as with the 2.4.1, gradient descent step search as with 2.4.2 and the combination of both as with 2.4.3. Downhill simplex method can be considered as gradient method with adaptive step size following the remaining distance to the minimum.

2.4.1 Three-Steps Search (TSS) algorithm [15]

As the name suggest, the three-step search (TSS) algorithm works in 3 steps following the coarse-to-fine strategy. The TSS algorithm is efficient and works accurately when the cost function increases monotonically as it moves away from global minimum without too much distortion. However, If the block with small motion is observed, the efficiency of TSS is reduced significantly. The first step of the algorithm starts the search from the center with a step size S=4 and the search parameter value =7. Hence, eight locations around the center with step size ± S are obtained. Among the eight searched locations, the least cost is selected, and the location is used as a new search origin. The second step reduces step size by half as S=S/2. The third step repeats second steps resulting the step size S=1. When the procedure is completed, the best match is found and for search range 'P'=7 as an instance, the evaluation of 225 points by full search would need 9+8+8=25 points of evaluation by three-step search. The illustration of 3 step search is shown on Figure 2.2 (a).

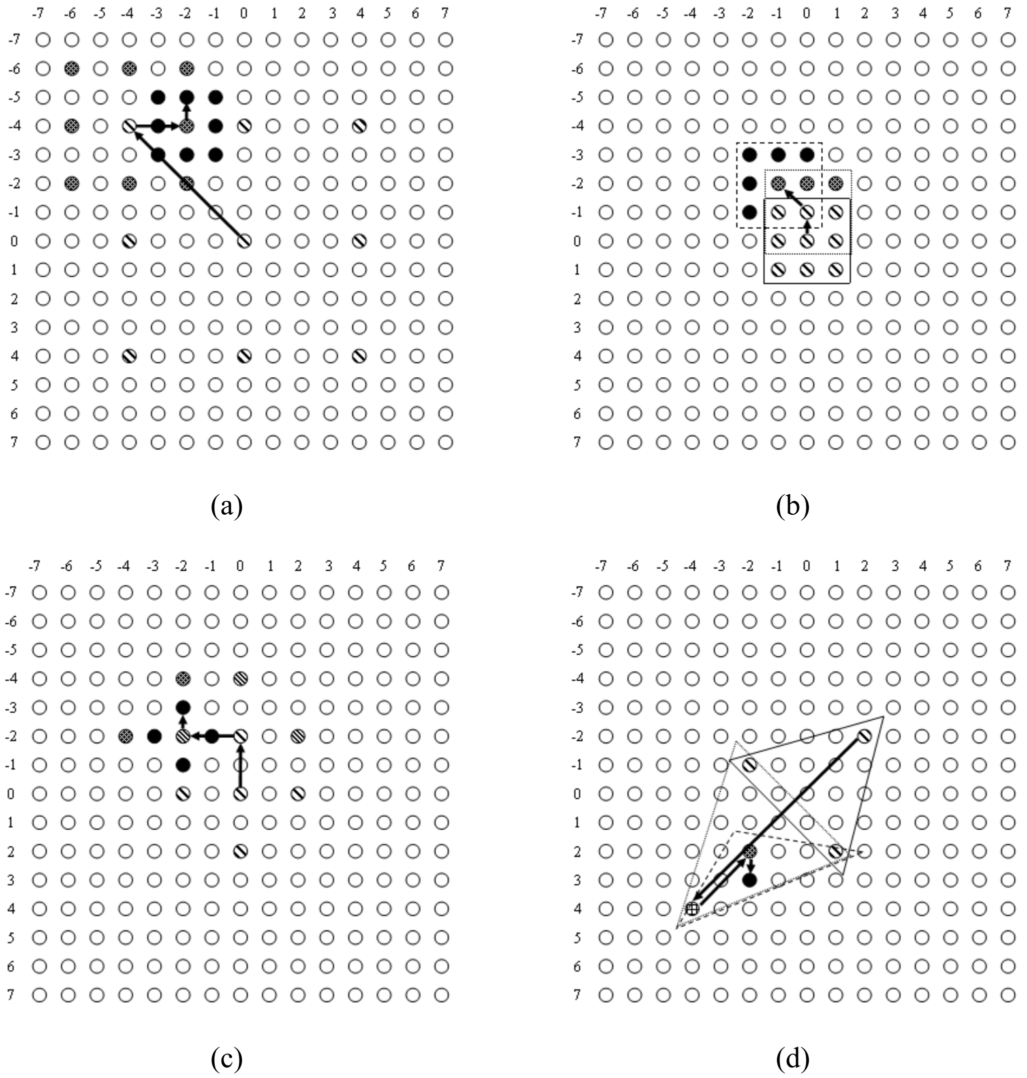

(a) (b)

(c) (d)

Figure 2.2. Various types of search algorithm

2.4.2 Gradient descent algorithm [16]

On the block-based gradient descent search (BBGDS) algorithm, the first step is checking a square block of 3 x 3 pixels where its center is the origin. After evaluating the cost function for all nine points in the checking block, if the minimum occurs at the center, the motion vector points to the center. Otherwise, the center is moved to the best match pixel, and the procedure is repeated to first step. On the second iteration and after, most of the pixels in the checking block have already been evaluated in a previous step. Therefore, the smaller number of evaluations are needed. The search procedure of the BBGDS always moves the search in the direction of optimal gradient descent to the direction where the cost function approaches its minimum. This algorithm works like a ball that rolling on the floor following the lower location. The algorithm works at the maximum efficiency when the minimum location is close to the first origin. However, the algorithm tends to be trapped to a local minimum when much distortion is occurred. The complete illustration of BBGD is shown in Figure 2.2 (b).

2.4.3 Diamond Search (DS) [17]

The proposed DS algorithm consists of two search patterns that is large diamond search pattern (LDSP), and small diamond search pattern (SDSP). The LDSP evaluates nine points around the center composing a diamond shape while the SDSP pattern consisting of five checking points which makes a smaller diamond shape. In the DS algorithm, LDSP is used as a coarse searching procedure until the minimum value of cost function point to the center. Afterward, the search pattern is then switched to SDSP to refine the searching result. The position at the best match among five points of SDSP is decided as the motion vector of the best matching block. This method is similar to the gradient descent method except in the search pattern and combination with coarse to find strategy. This method however can be modified by using larger diamond to provide bigger coverage of search. The illustration of Diamond Search algorithm is shown in Figure 2.2 (c).

2.4.4 Downhill simplex method [18]

This method is originally for function minimization; however, its application is later expanded for block matching search [19]. A simplex is collection of n + 1 points in n-dimensional space. In the downhill simplex search, the simplex is updated in an iterative fashion to get a new point with smaller value until reaching terminating condition. In the case of motion estimation, as with 2-dimentional data, the simplex is a triangle. The search performance is much determined by the simplex initialization around the center. In this case, the performance is good when the motion vector is small. However, the motion vector can be predicted in advance by considering its neighboring vector. Since image processing deals with discrete pixels, the challenge is in the rounding strategy. While rounding to the nearest integer is the simplest method, it may reduce the accuracy. To retain the accuracy and keep the simplicity, the location with the smallest value of cost function among all neighboring point is used to be the newly updated point. The downhill simplex method works based on simplex reflection, expansion, and contraction operations. Figure 2.2 (d) shows an illustration of downhill simplex method.

2.4.5 Coarse-to-fine random search

In a general, coarse-to-fine step algorithm performs better with large displacement, while gradient method will be the best with small displacement. However, the motion cannot be determined in the initial stage whether it is a large motion vector or small motion vector. In addition, both coarse to fine step algorithm and gradient descent algorithm are developed on the assumption that the surface is monotonic to the minimum location of SAD. In many cases, this situation is not always true. When the distortion is high, both methods are prone to be trapped in a local minimum. In this case, the full search approach shows its superiority.

Instead of attempting full search, a random selection to the point of evaluation could be considered. If the random entropy is sufficient, the accurate result is obtained. Coarse to fine strategy can be employed where larger scale of random generator is applied in initial phase, followed by the finer scale. The number of attempts which defines the computational requirement will be a proportional trade off to the accuracy of the search.

2.4.6 Nearest surface minimum estimation

As an opposite to the coarse-to-fine random search, the sum of absolute difference over a region of interest is modeled by a surface equation, such as quadratic polynomial surface.

$$\widehat{SAD} = a\left((x-b_x)^2 + \left(y-b_y\right)^2\right) + c \qquad \text{Eq. 13}$$

The procedure is quite straight forward. First, SAD of four point around a center is calculated. Since Eq. 13 is four variables equation, the coordinate of minimum $\left(b_x, b_y\right)$ can be calculated by direct resolving.

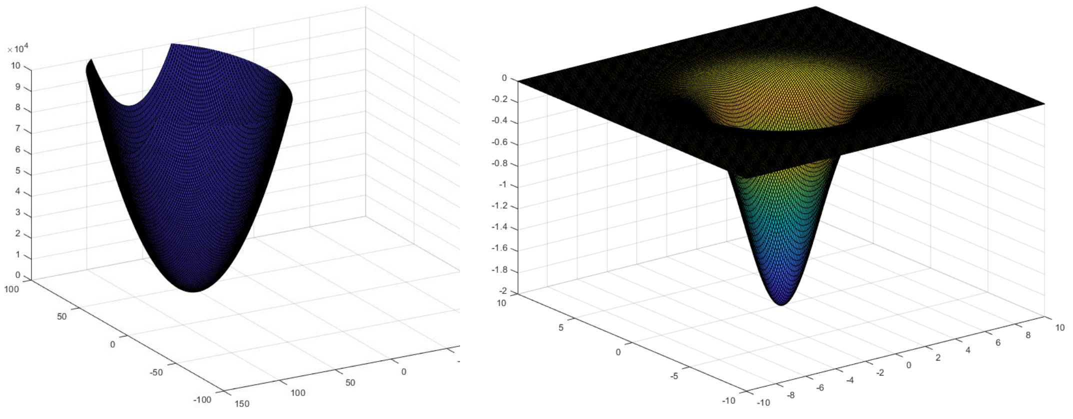

(a) (b)

Figure 2.3. A model of SAD search

When more points are evaluated, the number of equations is more than the unknowns. On that case, the coordinate can be determined by least square approximation. The surface is not limited to quadratic polynomial. Another surface such as gaussian surface can be used. In this case five points are required to determine the minimum position.

$$\widehat{SAD} = ae^{-\left(\frac{(x-b_x)^2+(y-b_y)^2}{2c^2}\right)} + d \qquad \text{Eq. 14}$$

An example of quadratic surface and 2-D gaussian surface is shown by Figure 2.3 (a) and (b) respectively.

2.5 Speckle Tracking Outlier Removal

A dynamic flow vector can be calculated from a measurement of multiple frames in an ultrasound movie. For a given number of frames F_{t-2}, F_{t-1}, F_t, F_{t+1} and F_{t+2}, vector calculation was performed by choosing the middle frame F_t as reference for searching in the two previous frames and the two subsequent frames, giving four velocity fields in total. In the real application, the frame number can be skipped to a predefined number to give an alternative to the speed of measurement. The four-frame velocity vector is usually averaged to remove some glitches and get a smoother dynamic flow vector. However, this averaging will reduce the sensitivity at some degrees. For that reason, I proposed an outlier detection technique based on assumption that particles move smoothly during five frames.

In this case, motion angle range is kept under a tolerance value, that is

$$\max_i\{\theta_i\} - \min_i\{\theta_i\} < \theta_{th} \qquad \text{Eq. 15}$$

and the motion magnitude also must not exceed certain threshold

$$\max_i \frac{|v|_i}{|v|_i'} < |v|_{th} \qquad \text{Eq. 16}$$

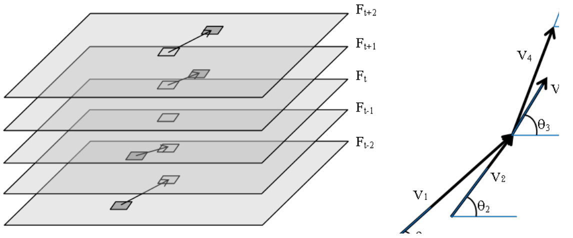

Figure 2.4. Four velocity vectors obtained from five frames

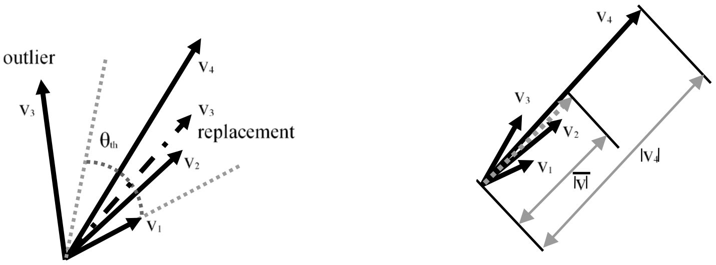

(a) *(b)*

Figure 2.5. Angle and magnitude outlier detection method

The range of calculation must be done in 4 quadrants. Any velocity with phase or magnitude that lays out of the allowed range is considered as an outlier and replaced by average value of the surrounding vectors. Since four vectors exist for each block, only one secluded vector is considered as outlier, but not in the case of two vectors. Figure 2.5 shows an illustration of outlier detection and replacement of a velocity vector sequence based on common angle and magnitude boundary.

Subsequently, the outlier removed velocity vectors are averaged and the results are represented in the form of velocity vector field as well as phase and magnitude color map. The magnitude map brightness and phase offset adjustment provide better visualization appearance and to alleviate eye judgement of a ligament adhesion. Additionally, the velocity is projected to a majority velocity angle to obtain tissue layers visual before slicing to cross-sectional view.

2.6 Software Implementation

I have implemented a signal processing software based on ultrasound speckle tracking for shoulder ligaments velocity visualization. In this implementation, a ROI is selected from frames of an ultrasound image sequences in a DICOM formatted file. Inter-frame small block (kernel) displacements are estimated by sum of absolute differences (SAD) based block matching algorithm. I choose SAD out of optical flow method considering its better fit with noisy ultrasound images source. The kernel size and searching area were tuned experimentally conforming the measurement data. Figure 2.6 shows a complete sequence of described signal processing sequence.

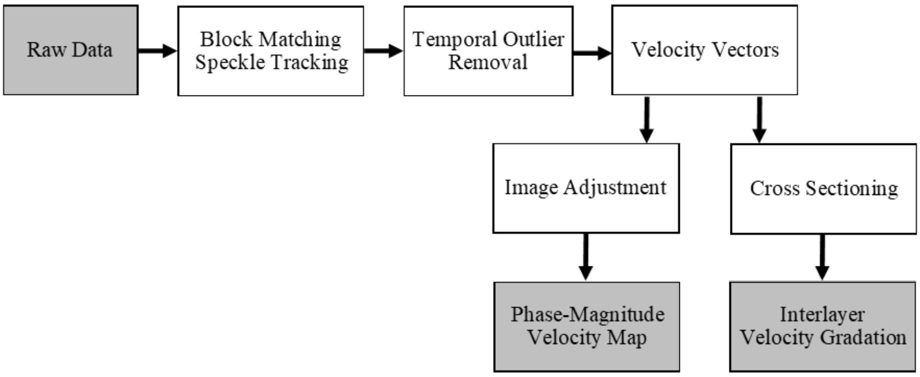

Figure 2.6. Ligament velocity visualization scheme

The algorithm framework was implemented in MATLAB® (R2019a) and the App Designer™ graphical user interface (GUI). In order to obtain faster computation, the most resource demanding SAD algorithm was implemented in precompiled MEX function written in C. The developed software was tuned for the available data samples. However, customization was made possible by GUI adjustment to alleviate separated experiments by different users. Figure 2.7 and Figure 2.8 show the software architecture of the ultrasound ligaments velocity visualization and the home view of software implementation GUI respectively. The completed user guide for the software is attached in the Appendix A.

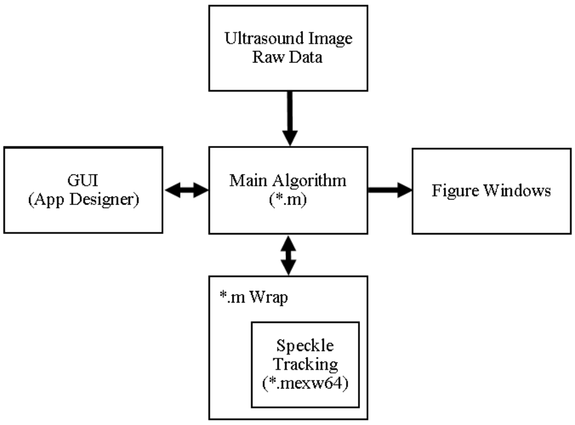

Figure 2.7. Software implementation of speckle tracking US analyzer

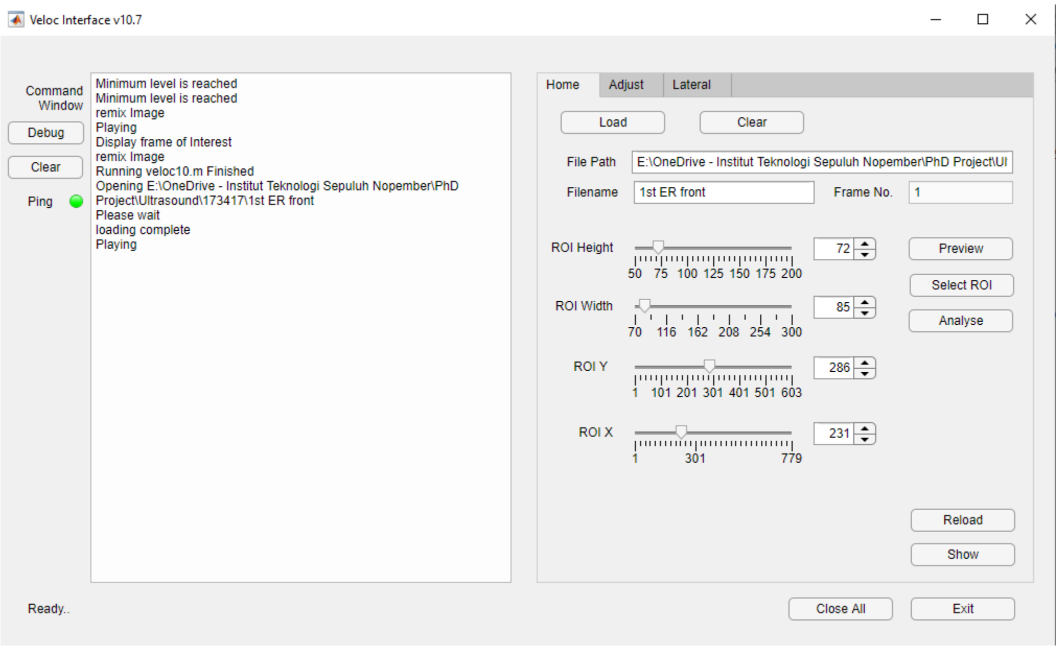

```
Minimum level is reached
Minimum level is reached
remix Image
Playing
Display frame of Interest
remix Image
Running veloc10.m Finished
Opening E:\OneDrive - Institut Teknologi Sepuluh Nopember\PhD
Project\Ultrasound\173417\1st ER front
Please wait
loading complete
Playing
```

File Path: E:\OneDrive - Institut Teknologi Sepuluh Nopember\PhD Project\UI
Filename: 1st ER front
Frame No.: 1
ROI Height: 72
ROI Width: 85
ROI Y: 286
ROI X: 231

Ready..

Figure 2.8. GUI of ligament velocity analyzer software

2.7 Experiments

An experiment was carried out to evaluate the functionality of the software when performing analysis to an ultrasound movie of a shoulder of a healthy subject (male, 34). In this experiment, subject laid in a supine position and the arm was moved from shoulder neutral position as in Figure 2.9 (a) to maximal First External Rotation (1st ER) as in Figure 2.9 (b) and reversely for three cycles. All sequence was completed in about 9.5s producing in total 302 frames of movie.

(a) (b)

Figure 2.9. Measurement during 1st ER

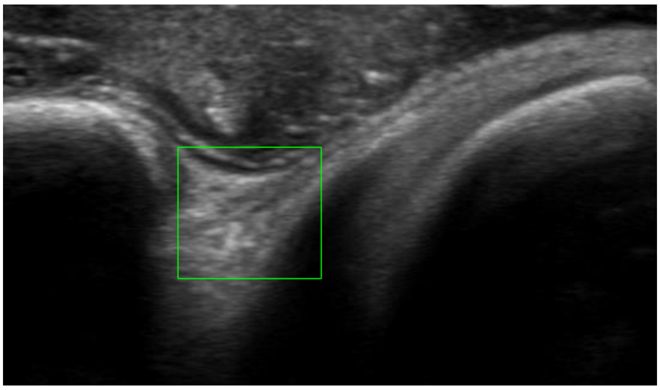

Figure 2.10. Selected ROI

A manual observation has shown that each forward 1st ER movement was completed after approximately 57 frames. The probe was placed vertically in front of shoulder at the best visual of coracoid process, CHL and subscapularis (SSC) muscle. As a comparison, another experiment was carried out to an abnormal subject (male, 55) with adhesive capsulitis symptoms. Due to difficulties, the 1st ER movement was done slower which takes 929 frames of 29 seconds to make two complete cycles. Each movement took different number of frames varied from 79 to 118.

In this dissertation, 1st ER is defined as shoulder rotation in neutral. The Second External Rotation (2nd ER) and Third External Rotation (3rd ER) are defined as external rotation with abduction and external rotation with flexion respectively. Figure 2.11 shows a clear depiction of these movements.

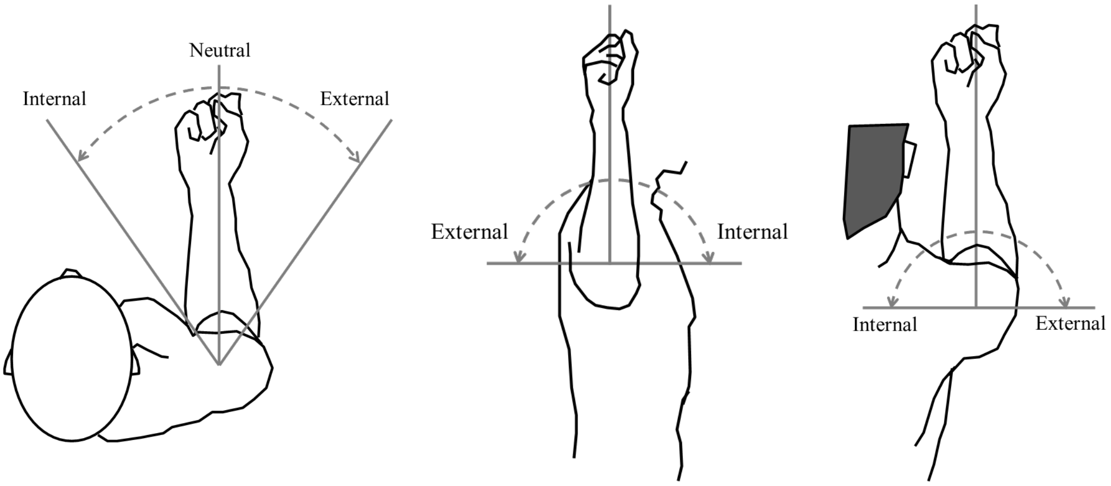

(a) (b) (c)

Figure 2.11. Rotation movement in neutral (a) abduction (b) and flexion (c)

Sample data were acquired with an Aplio i800 TUS-AI800 (Canon Medical Systems Inc.) using a PLI-1205BX linear probe. Images were recorded at 32 fps in 960×1280 resolution of 8 bits true color. Recordings were exported to DICOM formatted files and analyzed by MATLAB® implemented software.

2.7.1 Outlier removal capability

The velocity vectors were calculated from a ROI selection from ultrasound images as shown on Figure 2.10. This area comprises CHL, SSC and Sub-coracoid fat in the area around the coracoid process under covering deltoid muscle.

The ROI of 70x70 pixels of two subject measurements at three significant frames near the end of forward 1st ER movement were selected for each subject. This selection results in total of 29400 block of five-frame vector sequence of the most significant movement on the measurement data. The outlier removal algorithm is implemented to this data by varying the binding angle limit from 10° to 160° with 30° increment step and magnitude scale limit from 1.2 to 2.2 with 0.2 increment step. The average distance of each individual vectors to their mean in the five-frame sequence are averaged for whole 29400 blocks.

This experiment is run to demonstrate a quantitative improvement of outlier removal technique and to obtain an optimum value of magnitude and angle threshold. The resulting velocity vectors are adjusted and represented as phase and magnitude map. Eventually, the working of speckle tracking method to visualize layers of tissues is demonstrated. Image pair of normal and abnormal subject is presented for visual comparison.

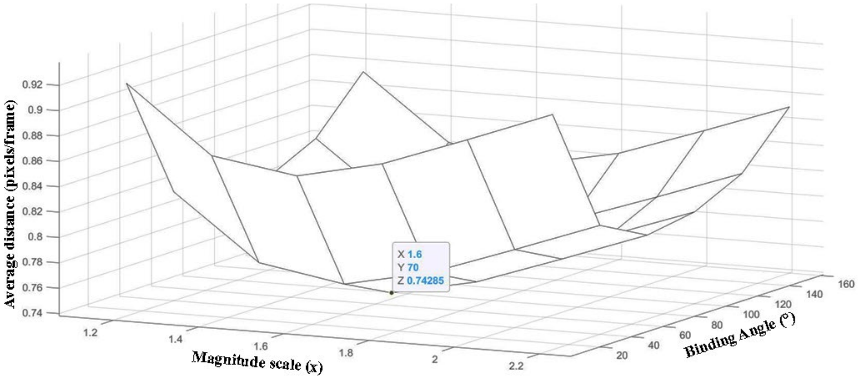

Figure 2.12. Velocity vector deviation

Figure 2.12 shows simulation result of velocity vector deviation by magnitude and angle boundary change with the given set of test data. Velocity vector average deviation is altered by the angle and magnitude variation. The minimum value 0.743 of vector deviation is obtained for angle threshold 70°and the magnitude scale of 1.6. The average distance of original velocity vectors before outlier removal is 1.3079.

Figure 2.13 shows a comparison of velocity map which is obtained from a normal subject with blind averaging method (18a and 18b) and the temporal outlier method (18c and 18d). The left figures (18a and 18c) comprise angle of velocity vectors represented in *hsv* color map. The right figures (18b and 18d) are relative magnitude of velocity vectors represented in grayscale color map.

In this experiment, an evaluation is carried out for the outlier removal criteria by using 5 consecutive frames. The proposed outlier removal technique has improved the vector deviation of up to 43% with optimally selected parameters. There are a few differences of the blind averaging and the temporal outlier removal method that is shown on Figure 2.13. Some spots and irregularities were removed which significantly improved the visual appearance of presented data.

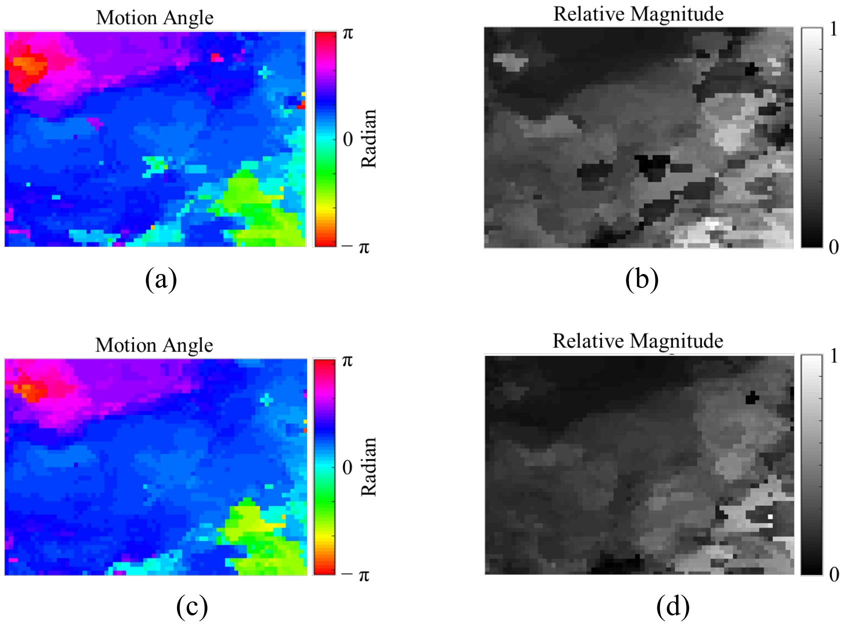

Figure 2.13. Ligament visualization with and without outlier removal

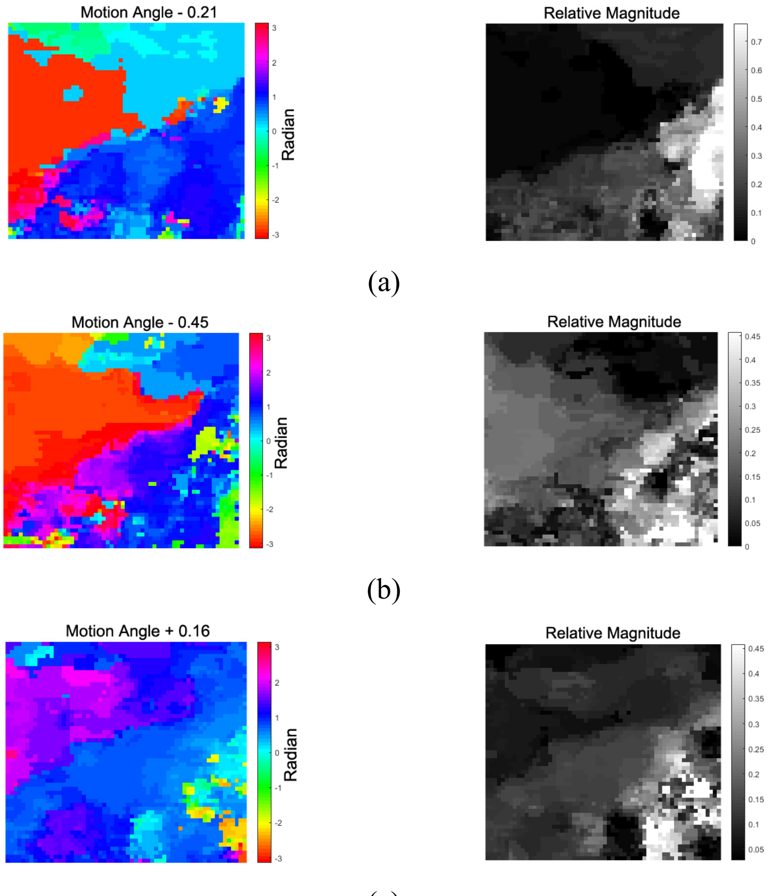

(a)

(b)

(c)

Figure 2.14. Velocity phase and magnitude map of normal subject

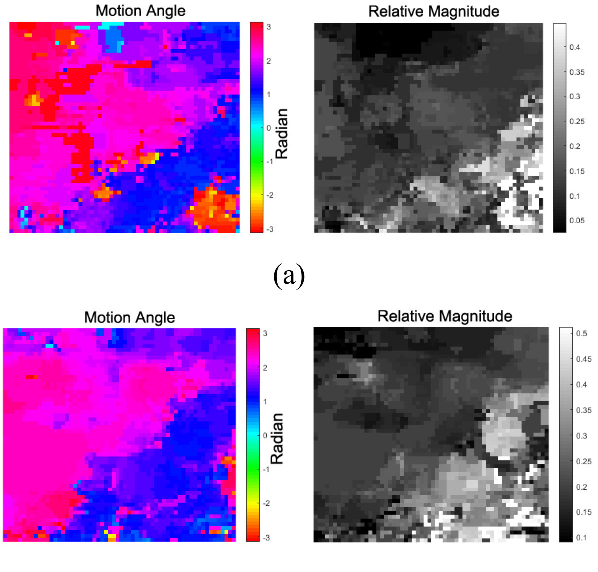

(a)

(b)

Figure 2.15. Velocity phase and magnitude map of abnormal subject

2.7.2 Layers of tissue visualization

Figure 2.14 (a, b and c) show the velocity vectors from frame 84, 87 and 90 which have the most significant observable movement. On the other hand, the evaluation of an abnormal subject with adhesive capsulitis symptoms was carried out resulting velocity visualization from frame 558 and 609 that is shown in Figure 2.15 (a and b).

It can be seen from Figure 2.14 that by using speckle tracking taken from a normal subject, layers of tissue can be identified from their velocity difference. The image top of phase map with mint color in Figure 2.14(a) represents deltoid muscle. In Figure 2.14(b), the sub-coracoid fat triangle is displayed clearly with red color. Figure 2.14 (c) of phase map shows CHL by blue color stretching along diagonal as well as underneath SSC with irregular arctic color impression.

2.8 Discussion

The observation to the subject with adhesive capsulitis symptoms in Figure 2.15 display almost similar images with the normal subject, except the appearance of sub-coracoid fat triangle that looks solid with more homogeneous magenta color. The area of CHL and SSC is less distinguishable for more cases, but the difference is more obvious with the cross-sectional view.

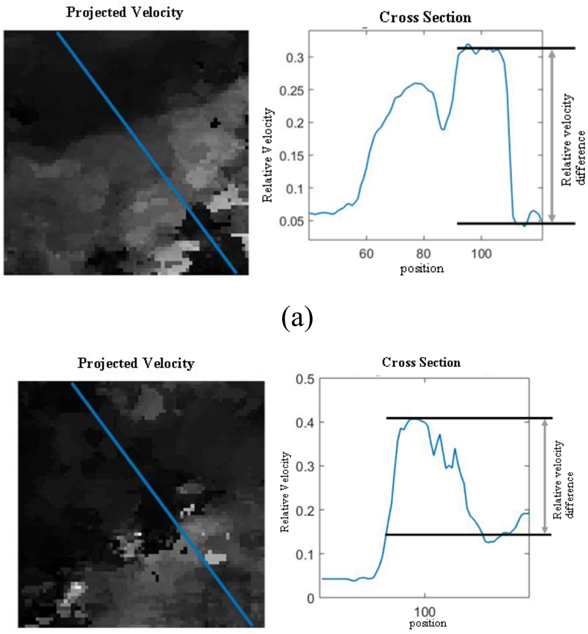

(a)

(b)

Figure 2.16. Cross-section visualization.

Figure 2.16 shows cross-sectional visual along specified cut line from normal subject at magnified area of ROI on frame 90 of the normal subject using bilinear interpolation method. In this view, there is a magnitude transition of about 0.3 on the normal and 0.25 on the abnormal subject. Three different groups of level are observed; thus, it can be deduced that 4 layers of tissue exist along this slicing cut. The magnitude transition at the end of cross-sectional view may indicate SSC and the CHL relative velocity difference, which is slightly different for normal subject and subject with AC symptoms. This difference has indicated a potential of ultrasound speckle tracking method development as a diagnostic tool of AC disease. This examination also indicates that phase information of velocity gives more information clarity than magnitude.

This chapter is closed by a successful implementation of a software for visualizing ligament layers based on speckle tracking algorithm. The method was tested to objectively quantify ligament displacement and layers of tissue. To the best of my knowledge, this is the first implementation of speckle tracking method in orthopedics to visualize the layers of tissue in the shoulder and attempting to analyze abnormality based on it. This method is interesting since the data are analyzed from an ultrasound movie which is obtained with a commercially available ultrasound machine. In the following chapter, further improvement of the method by quantizing shoulder adhesion is discussed.

Chapter 3

Quantitative Assessment of Shoulder Adhesion

Restricted movement of a shoulder is one of Adhesive Capsulitis (AC) symptoms, in addition to the other symptoms. It is usually determined by a physical examination. In this chapter, I will present an analysis result to the shoulder ultrasound movies, to investigate a correlation of the limited shoulder Range of Motion (ROM) and the significance trace of the ultrasound B-mode appearance. The speckle tracking method is used to quantify the velocity difference between shoulder ligaments that may indicate tissue adhesion, which is linked with the movement restriction. The result of experiments is to be published in a scientific journal.

3.1 Shoulder Anatomy

A shoulder is made of three bones those are humerus, scapula, and the clavicle that all together forming a ball-and-socket joint. The head of humerus fits into a shallow socket in the scapula, surrounded by shoulder capsule which is a strong connective tissue. Synovial fluid lubricates the joint and shoulder capsule to help smoothing movement of the shoulder.

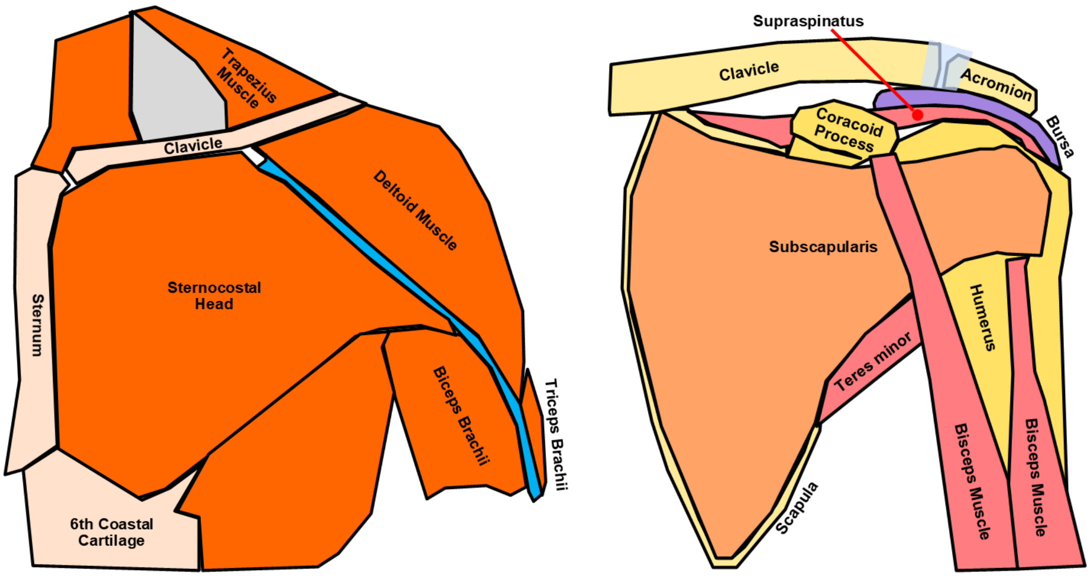

(a) (b)

Figure 3.1. Anatomical image of shoulder

The subscapular fossa of the shoulder is filled by a triangular muscle called the subscapularis which is one of the rotator cuffs muscles that act as a movement stabilizer of humerus head in the glenoid fossa. The outer part of the shoulder is composed of deltoid muscle which can be divided into three parts, i.e., pars clavicularis, pars acromialis and pars scapularis. The anatomical image of shoulder from outside and inside layer is shown in Figure 3.1 (a) and (b) respectively.

In a previous research, it was found that thickening of Coracohumeral Ligament (CHL) [7] and joint capsule [20] makes the joint feel stiff and tight. In a severe condition, unbearable pain emerges, and the shoulder is unable to move.

3.2 Observation of Ligament Adhesion

A limited sliding movement of the supraspinatus tendon was observed by dynamic sonography. The routine examination of the shoulder was performed including the rotator cuff and biceps tendon, with the arm held in a neutral position, maximal internal rotation, and hyperextension. The transducer was placed on the tendon of the supraspinatus muscle longitudinally, and the movement of the supraspinatus tendon was observed when the elbow joint is elevated laterally up to 90 degrees maximum.

Analyzing all true positive cases of adhesive capsulitis showed a disturbed sliding movement of the supraspinatus tendon under the acromion with various degree of limitation [21]. Nevertheless, the result was obtained by qualitative approach.

In this dissertation, ROM is measured from the First External Rotation (1st ER) of the shoulder, which is the most affected motion in the AC. Its examination is often performed during diagnosis of the AC. The internal rotation of humerus involves the subscapularis, pectoralis major and latissimus dorsi that work together. Under a sonography evaluation during the 1st ER motion of a normal shoulder, a subscapularis is observed gliding freely under the deltoid muscle. The free gliding motion can be represented by the high velocity relative to the surrounding tissue. Based on the previous finding, the gliding motion of subscapularis will be investigated. The adhesion is considered when the subscapularis moves at similar speed to the deltoid muscles. In practice, the subscapularis and deltoid muscle velocity ratio may vary from one to another subjects. This parameter will be called Adhesion Index (AdI) which is quantified as a different velocity which can be measured by speckle tracking. The B-mode image of subscapularis is shown in Figure 3.2.

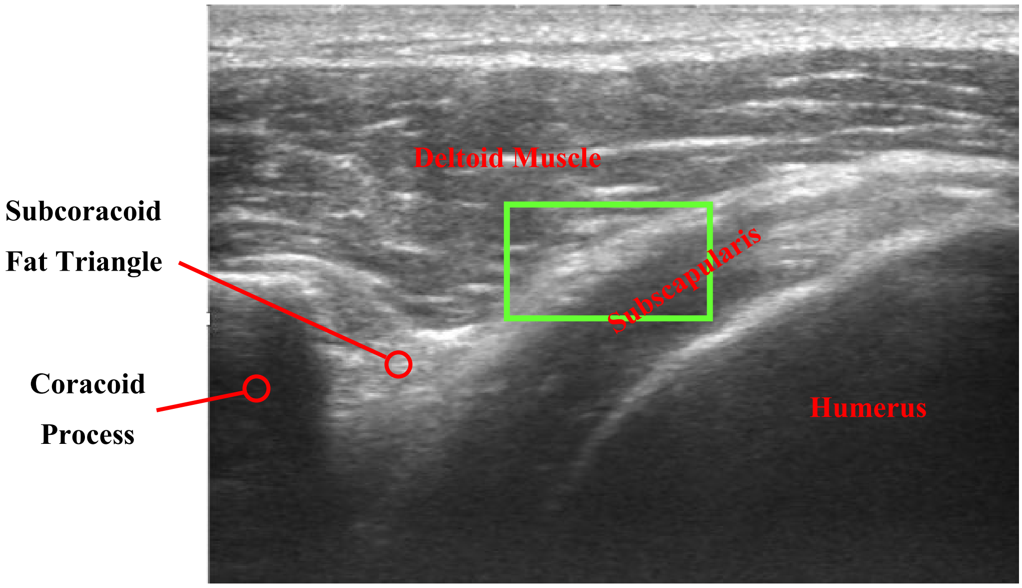

Figure 3.2. B-mode image of subscapularis and the deltoid muscle

3.3 Quantifying Ligament Adhesion

The first step to determine the AdI is performing a speckle tracking to a region of interest which include an area of adhesion between subscapularis and the deltoid muscle as shown in Figure 3.2. My experiment use block size of 8 pixels and frame step size of 2. The region of interest is divided into two parts, that is A and B parts, and the AdI is obtained by calculating velocity ratio between two sub regions (A/B). By this approximation, the AdI is heading towards unity when the severe adhesion occurs. Since velocity is a vector quantity, comparison cannot be performed directly. It can be seen from Figure 3.3 that the velocity vector is unregularized, and thus a regularization must be performed. In this image, the region of deltoid muscle and subscapularis are denoted with A and B respectively.

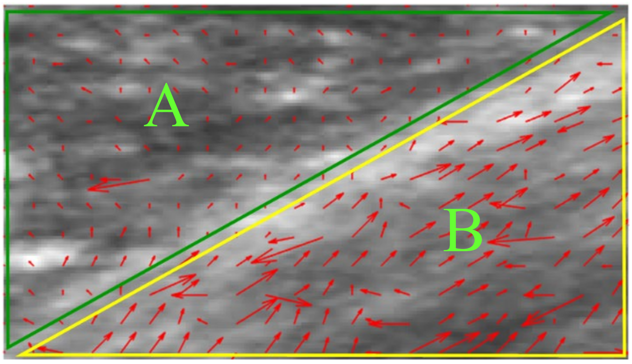

Figure 3.3 Calculated velocity vector by speckle tracking.

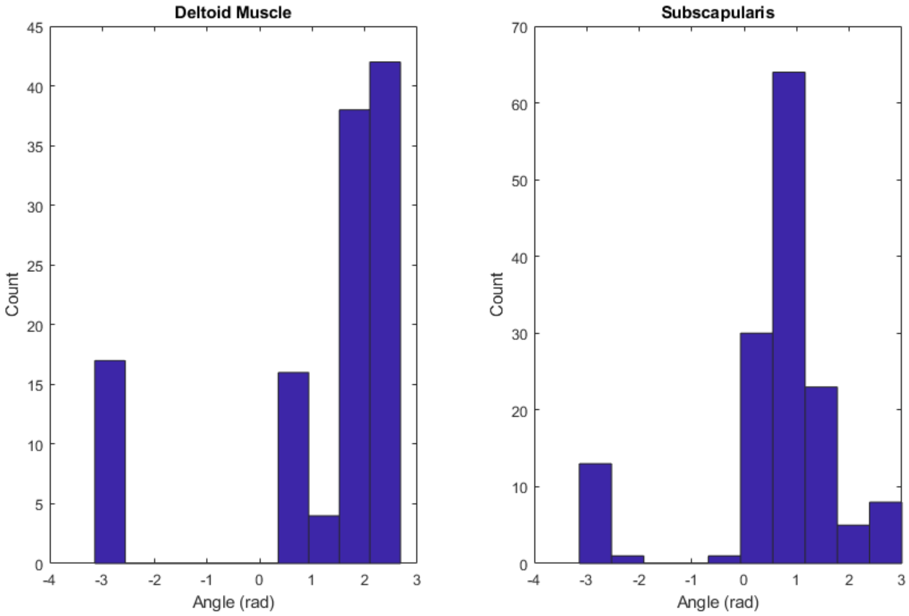

Figure 3.4 Histogram analysis of velocity vector direction

By analyzing histogram of vector direction of region A and B, the majority direction of each region can be determined. On the example in Figure 3.4, deltoid muscle and the subscapularis move at an angle of 2.07 rad and 0.83 rad, respectively. All the velocity vectors for each region are projected to this majority angle to get the approximation of magnitude. After this regularization, the projected velocity vector can be seen in Figure 3.5, meanwhile the magnitude map is shown in Figure 3.6. Afterall, the vectors on the deltoid muscle region are projected once more to the direction of subscapularis motion, and the velocity ratio is obtained by comparing A and B after finishing this calculation. An example in Figure 3.6 is a measurement of a normal subject with an adhesion index of 0.1865.

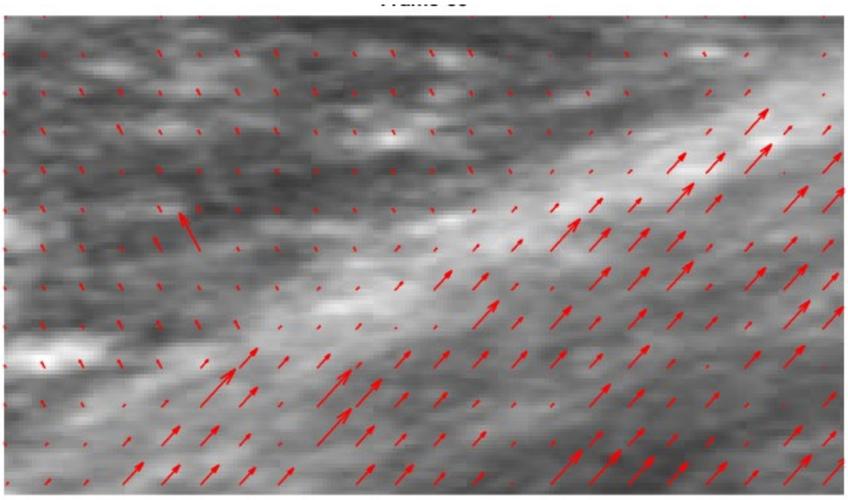

Figure 3.5 Regularized velocity vector

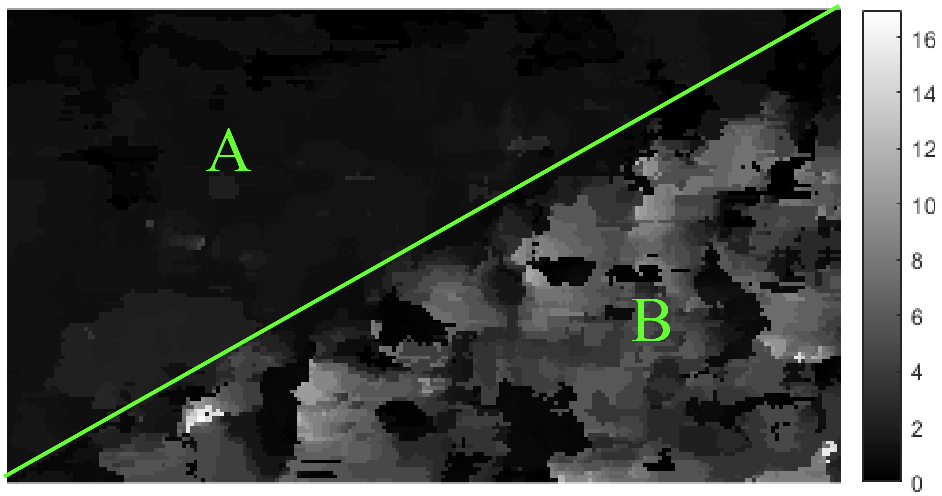

Figure 3.6 Magnitude of regularized velocity vector

3.4 Clinical Study

3.4.1 Study population

In the present study, the shoulder AdI of the AC patients is compared with healthy control subjects. In this study, a total of 26 participants are enrolled. 22 participants are those diagnosed with AC, which 12 among them are further classified to secondary AC due to the associated Rotator Cuff Tears (RCT), and the 10 others are classified as idiopathic AC. The rest 4 participants are normal subjects. All patients complained with shoulder pain and majority are observed with the restricted motion with some exceptions.

Both side of the shoulder of normal subjects are included as control, 6 affected shoulder side of idiopathic AC patient and 8 affected shoulders of secondary AC patients are analyzed after excluding the measurement with severe contracture where the patient lack ability to perform external rotation. The non-affected shoulder of 10 idiopathic AC and 9 secondary AC patients are included when analyzing the relationship between ROM and the subscapularis adhesion. Since adhesive capsulitis shoulder disease is not traumatic and gradually develops with age, it is not uncommon to have adhesion symptoms on both sides of patient shoulder. Therefore, the non-affected side of adhesive capsulitis are not considered as a perfect control, and thus excluded when finding the relationship of symptoms with diagnosis.

All participants underwent B-mode sonography using Aplio i800 TUS-AI800 (Canon Medical Systems Inc.). The measurement data were analyzed by speckle tracking method with a

MATLAB® written program. The study was approved by the Ethics Committee Review Board of Tohoku University, and written informed consent was obtained from all participants.

The following procedure of the measurement is applied to all subject

1. In a sitting position, the arm of subject is moved from 45°internal rotation to the neutral position.
2. The B-mode motion is recorded in the best visual of coracoid process, CHL and subscapularis (SSC) muscle.
3. The recording is played and manually analyzed to determine the frame number at the start and end of the movement.
4. The adhesion index is analyzed for the middle of the movement and ± 3 frames (7 frames in total).
5. Subcoracoid fat triangle is used as a landmark, where the lower left corner of the ROI should overlap the tip of it. By this way, the adhesion index of the subscapularis and the deltoid muscle is measured.
6. The maximum 1st ER is measured separately by goniometer.

Since determining region of interest, the start and the end of the movie are performed manually, the reproducibility of measurement is tested by repeating the procedure from step 3. The result of reproducibility test is presented in the next sub-chapter.

3.4.2 Result

Figure 3.7 shows the velocity analysis of subscapularis and the deltoid muscle in a rectangular ROI of a healthy shoulder. The tissue velocity is represented by arrows pointing to the direction of motion with arrow length proportional to the velocity magnitude. The motion is performed from the 45°IR to the neutral position. Analysis was carried out in the middle frame of the motion and ±3 frames around it. The adhesion index is calculated as a division of deltoid muscle by subscapularis velocity to the direction of motion. In this case, the AdI of exampled normal during middle frame of the movement is 0.17 and the AdI value of ±3 frames around the middle were observed below 0.2. This value is basically interpreted as subscapularis free gliding motion under the deltoid muscle. In this circumstance, subscapularis can be visualized, and the velocity can be easily seen during the movement.

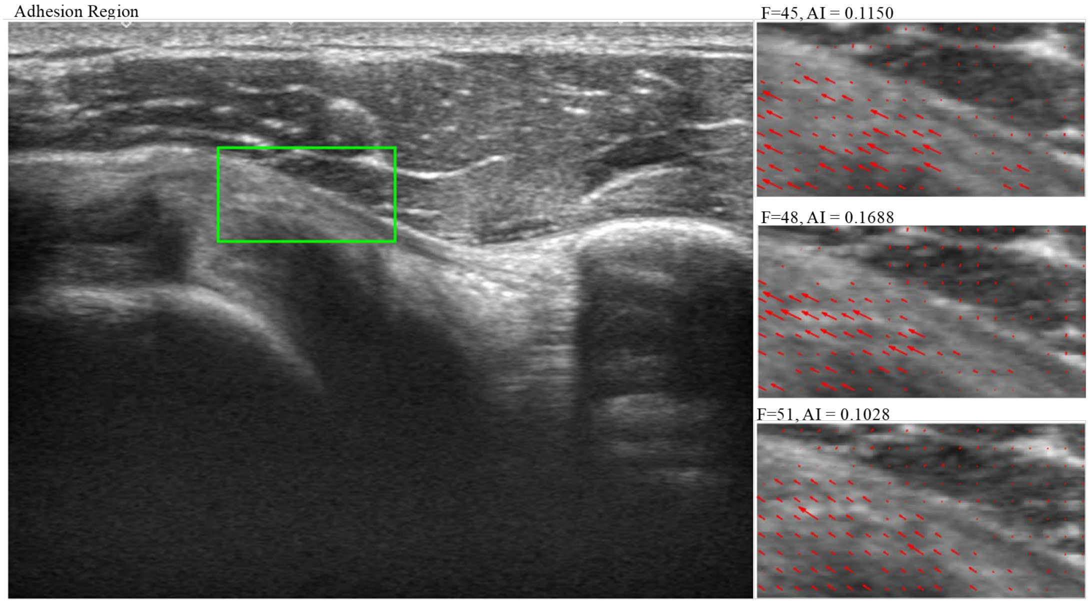

Figure 3.7. Velocity vectors in the 1st ER movement of a normal subject

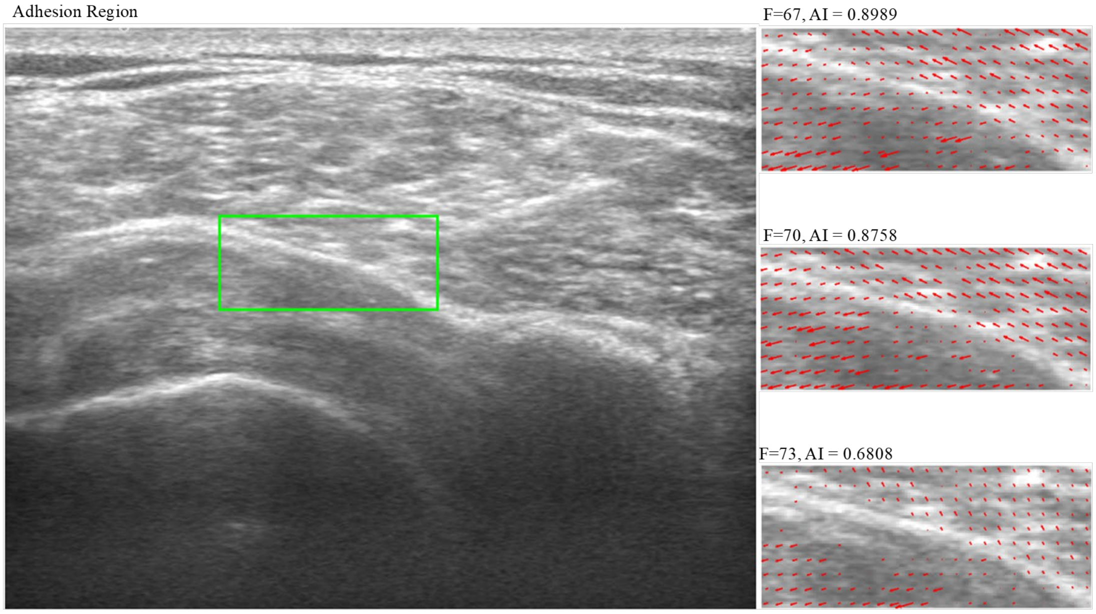

Figure 3.8. Velocity vectors in the 1st ER movement of a patient with an AC

Analysis of ligament adhesion by speckle tracking velocity visualization of participant shoulder with adhesive capsulitis diagnosis is shown in Figure 3.8. The instantaneous velocity flow pattern was analyzed frame by frame using speckle tracking of the B-mode image. In this observation, adhesion index at middle frame is approaching unity. It means that the deltoid muscle moves at almost equal velocity with subscapularis. The AdI value of ±3 frames around the middle are observed higher than 0.6 for majority.

A relationship between ROM and the AdI of all participants is shown by a regression line in Figure 3.9. The AdI is negatively corelated to the ROM with a correlation coefficient of R = -0,489285. The value of ROM measurement for each diagnosis is shown in Figure 3.10.

The shoulder pain and stiffness could be classified further based on the trigger condition. Conditions when motion loss is caused by multiple factors such as rotator cuff tears, calcific tendinitis, glenohumeral or acromioclavicular arthritis, and cervical radiculopathy, rather than the result of isolated capsular restriction, could be classified as secondary AC. Therapy for these conditions should address the specific underlying etiology. On the other hand, the idiopathic (i.e., primary) AC is used for cases without any specific trigger [21].

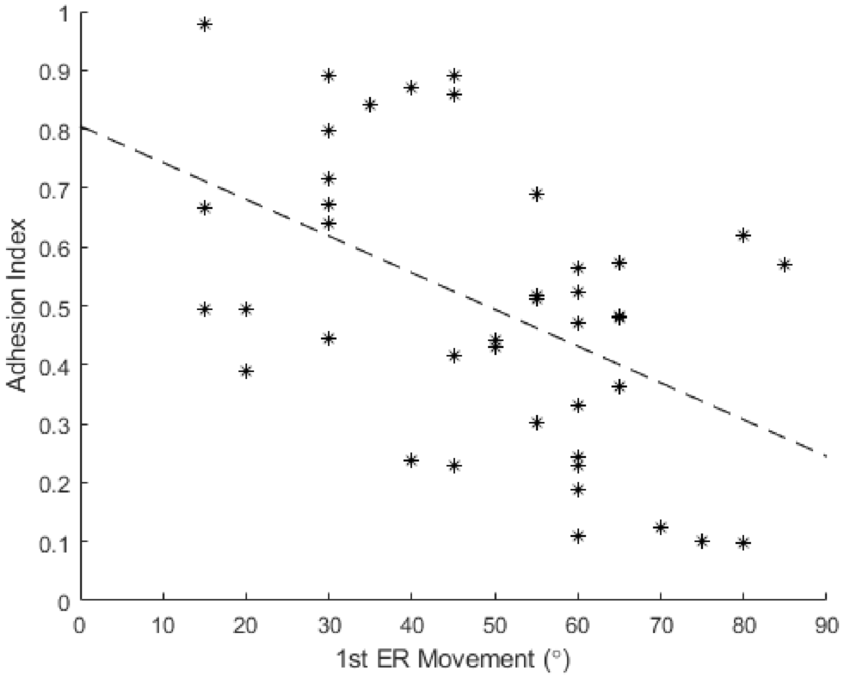

Figure 3.9. AdI and ROM correlation

Table 1. Adhesion index measurement results

Group	AdI	Maximum ER angle (°)
Control	0.37 ± 0.198	66.875 ± 12.48
Idiopathic AC	0.556 ± 0.22	39.17 ± 15.39
Secondary AC	0.544 ± 0.2176	34.375 ± 15.9

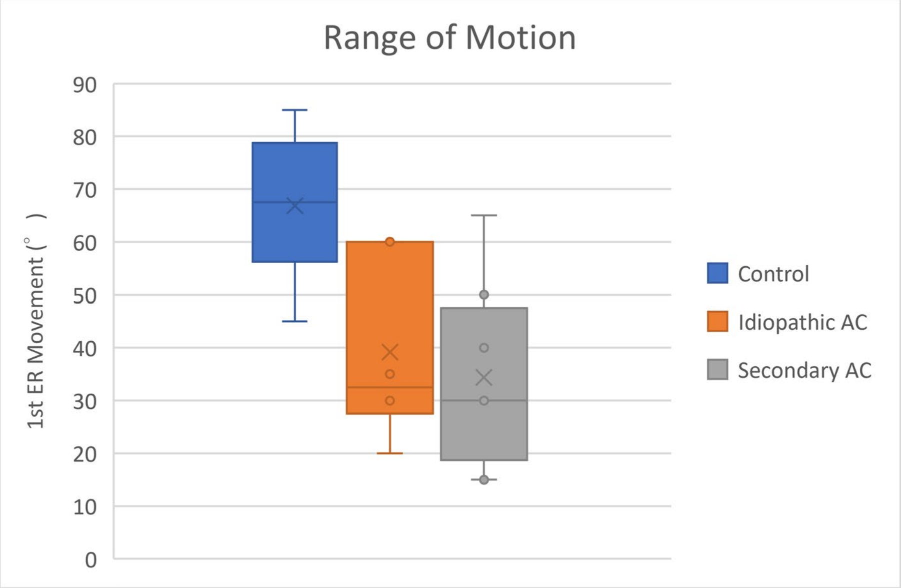

Figure 3.10. ROM chart based on diagnosis names

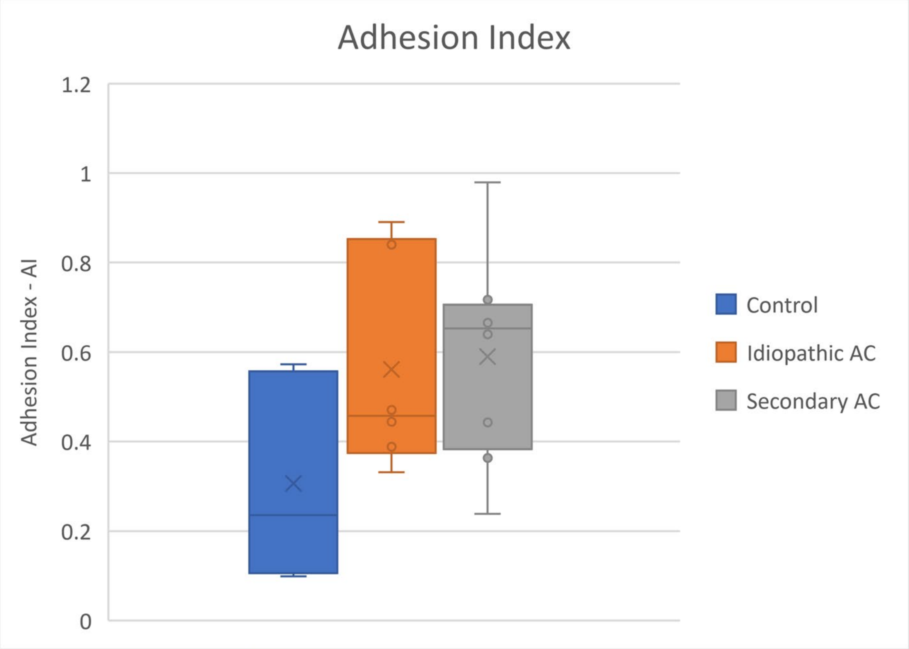

Figure 3.11. AdI chart based on diagnosis names

From the measurement data, it can be seen that the difference between the control and the common AC group is obvious. The AdI average of all AC cases appears higher than control group. In order to conclude the significance of this finding, I will analyze the difference between AdI mean of the common AC group and the control group by t test. The summary statistics are given by **Error! Not a valid bookmark self-reference.**.

Table 2. Statistical summary of AdI measurement

Group	**n**	$\overline{\boldsymbol{x}}$	**s**
AC	14	0.577	0.227
Control	8	0.3	0.21

The AdI value of AC patient is expected to be higher than control. Therefore, the hypotheses are set by

$$H_0 : \mu_1 = \mu_0$$
$$H_a : \mu_1 > \mu_0$$

The two-sample t test statistic is

$$t = \frac{\bar{x}_1 - \bar{x}_0}{\sqrt{\frac{s_1^2}{n_1} + \frac{s_0^2}{n_0}}} = \frac{0.577 - 0.3}{\sqrt{\frac{0.227^2}{14} + \frac{0.21^2}{8}}}$$

$$= 2.8890$$

The P-value for the one-sided test is P(T $\geq$ 2.8890). The degrees of freedom k = 7 are approximated from the smaller of $n_1 - 1 = 13$ and $n_2 - 1 = 7$. From statistical table interpolation of the 7 degrees of freedom, P (T $\geq$ 2.8890) = 0.011675. This calculation is a convincing evidence that AdI value is higher in the patient with AC (t = 2.8890, df = 7, P < 0. 011675) [22].

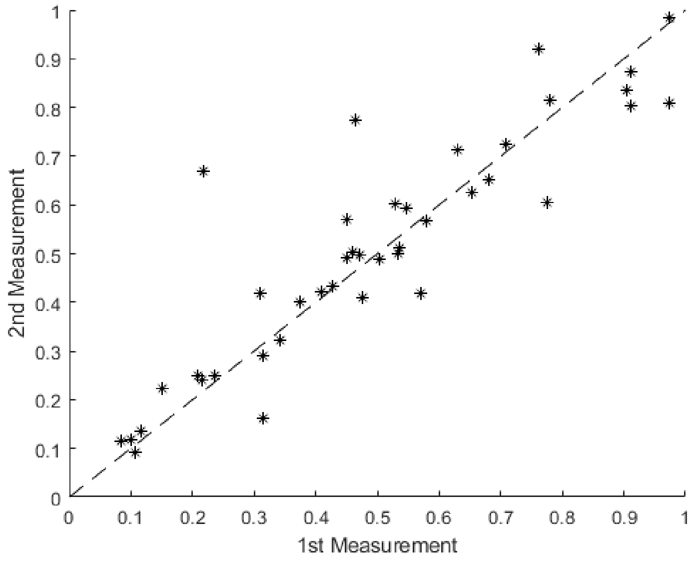

Figure 3.12 Comparison of two AdI measurements

At last, I would like to present a comparison of two measurement of the same data, by the speckle tracking method. Figure 3.12 compares two measurements of the same data. From the difference between two measurements in Figure 3.13, it can be seen that the mean difference is $\bar{d} = -0.0159$ and the standard deviation is s = 0.1118. The 4.88% data points that lay outside the 2s range of the mean difference, which is less than 5% means that the procedure has good reproducibility as suggested by Bland-Almant [23].

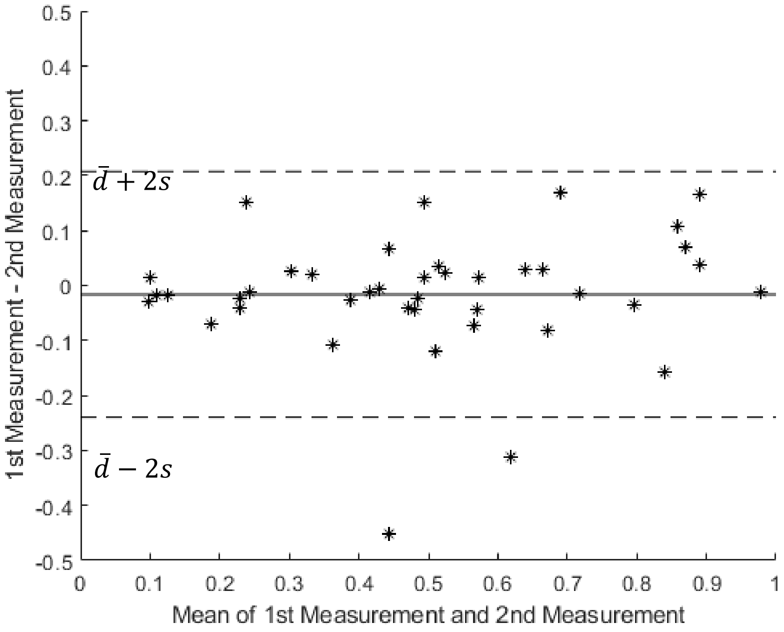

Figure 3.13 Difference between two AdI measurements of the same data

3.5 Discussion

As a summary, the 2D velocity map of shoulder movement were visualized. Adhesion severity between the subscapularis and the deltoid muscle was quantified by speckle tracking method. An experiment was performed in healthy participants as well as patients with idiopathic and secondary AC. It is shown that patient with AC encounters a noticeable adhesion on the subscapularis. In general, the subscapularis adhesion is correlated with the ROM. However, this finding does not show a significant difference of idiopathic and the secondary adhesive capsulitis group. This is justifiable since the AdI is not meant to substitute additional modality to identify the associated stiff and painful shoulder source such as MRI for Rotator Cuff Tears (RCT). The relatively high deviation could be an evidence that the subscapularis adhesion is not the only source of the limited ROM, thus, the restricted motion is not a unique representation of the AC disease. Nevertheless, AdI could be considered as a better measure than physical examination, since it rules out the pain caused ROM limitation.

It does not seem that high AdI always lead to AC since synovium and capsule thickening also contribute, but high AdI makes ROM restriction severe even in asymptomatic population. It is also important to find signs that the asymptomatic population progresses symptomatically. Even in cases of RCT, there are more cases with no symptoms, and the rupture progresses without being noticed [24].

If adhesions are found early and can be prevented from progressing, they may also prevent the next stage, such as joint capsule thickening due to immobilization. Even with the limited size of the sample, the correlation between AC symptoms and the subscapularis adhesion could be presented. It is demonstrated that the speckle tracking method provides additional insights about muscle adhesion in the shoulder. In the future, the speckle tracking algorithm may be developed as an essential tool for quantitative assessment of the shoulder movement function.

In this chapter, novel method to quantitatively analyze AC is based on ultrasound speckle tracking is described. The method is capable of quantifying subscapularis adhesion, by analyzing the ultrasound movie of shoulder movement. Relationship between subscapularis adhesion and the ROM as well as associated AC is shown. The application of speckle tracking in orthopedics is prevailing and the measurement suggested that AdI explained the origin of motion limitation, which could be a potentially better substitute for physical ROM assessment since it rules out pain caused motion limitation in the examination. However, the method has a limitation in which subscapularis AdI value cannot distinguish secondary from idiopathic AC without introducing additional modality.

Chapter 4

Color Doppler Shear Wave Elastography

Elasticity is an important property of biological tissue. It is commonly known that many diseases are associated with a distinct elasticity. In a research, Coracohumeral Ligament (CHL) elastic modulus of the symptomatic shoulder of Adhesive Capsulitis (AC) patient was found significantly greater than that of the unaffected shoulder [11]. However, that research used acoustic radiation force induced Shear Wave Elastography (SWE) measurement method which requires a special device with a very fast imaging capability. Therefore, development of a novel elastography method that can be implemented in a common commercial machine is a quite important.

There are numerous methods to assess tissue elasticity, such as by measuring attenuation and velocity of shear wave propagation as in vibrational sono-elastography [25] and color Doppler elastography [26] respectively. In this chapter, I will discuss in detail about mechanically induced shear wave color Doppler elastography, and its implementation with a modern commercial ultrasound machine. Parts of this chapter are to be published in the 2021 43rd Annual International Conference of the IEEE Engineering in Medicine and Biology Society (EMBC 2021) under a title "Binary Pattern Color Doppler Shear Wave Elastography" and in a scientific journal.

4.1 Propagation of Shear Wave in Soft Tissue

Biological tissue has a dispersive property which means that tissue displacement and shear wave propagation by a mechanical vibration depend on their frequency. A shear wave propagates inside a tissue in a complicated fashion and its property are approximated by several models such as Kelvin-Voigt (Voigt) model, Maxwell model, and Zener model [27]. A tissue is said to be isotropic if its properties remain the same when tested in different directions. In this case, a tissue can be approximated by a Voight model.

4.1.1 Voigt model

The merit of using Voigt model for modeling soft tissue is its simplicity and effectiveness. In a Voigt model, a biological tissue is modeled as a parallel connection of a purely elastic spring μ_1 and a purely viscous damper μ_2 as shown in Figure 4.1.

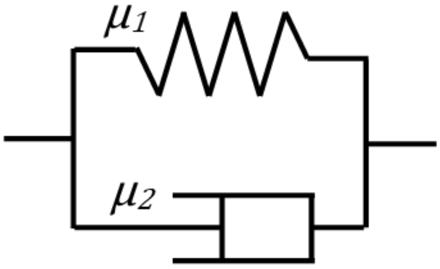

Figure 4.1. Voigt model of biological tissue

In this approximation, elasticity effect is dominant at very low frequency the tissue motion, while viscosity affects very high frequency motion [27]. Both elasticity and viscosity give an equal contribution in the tissue motion, hence, ignoring one of them will result in erroneous estimation. However, in typical cases when one parameter is much dominant, simpler approximations are close to the correct solution. Solution derivations of the sound wave equation for Voigt tissue is documented in detail [28]. In this solution, the shear wave velocity can be calculated by

$$v_t = \sqrt{\frac{2(\mu_1^2 + \omega^2\mu_2^2)}{\rho\left(\mu_1 + \sqrt{\mu_1^2 + \omega^2\mu_2^2}\right)}} \qquad \text{Eq. 17}$$

In this equation, the elasticity μ_1 and viscosity μ_2 are frequency independent constants. Therefore, when a tissue elasticity is much dominant that its viscosity, the shear wave velocity can be approximated by,

$$v_t = \sqrt{\frac{\mu_1}{\rho}} \qquad \text{Eq. 18}$$

A typical value of soft tissue parameter may be used for approximation such as $\rho = 1.1\ g/cm^3$. Since shear wave velocity is proportional to square root of elasticity, the measurement of tissue elasticity is performed by calculating a shear wave velocity. In this research, the measurement of shear wave velocity is performed by color Doppler imaging technique.

4.2 Color Doppler Techniques

Color Doppler Imaging (CDI) is a method for visualizing tissue motion in a body. The Color Flow Imaging (CFI) is likely a more specific term of CDI for blood flow imaging. In this dissertation, CDI and CFI are used interchangeably for the same intention.

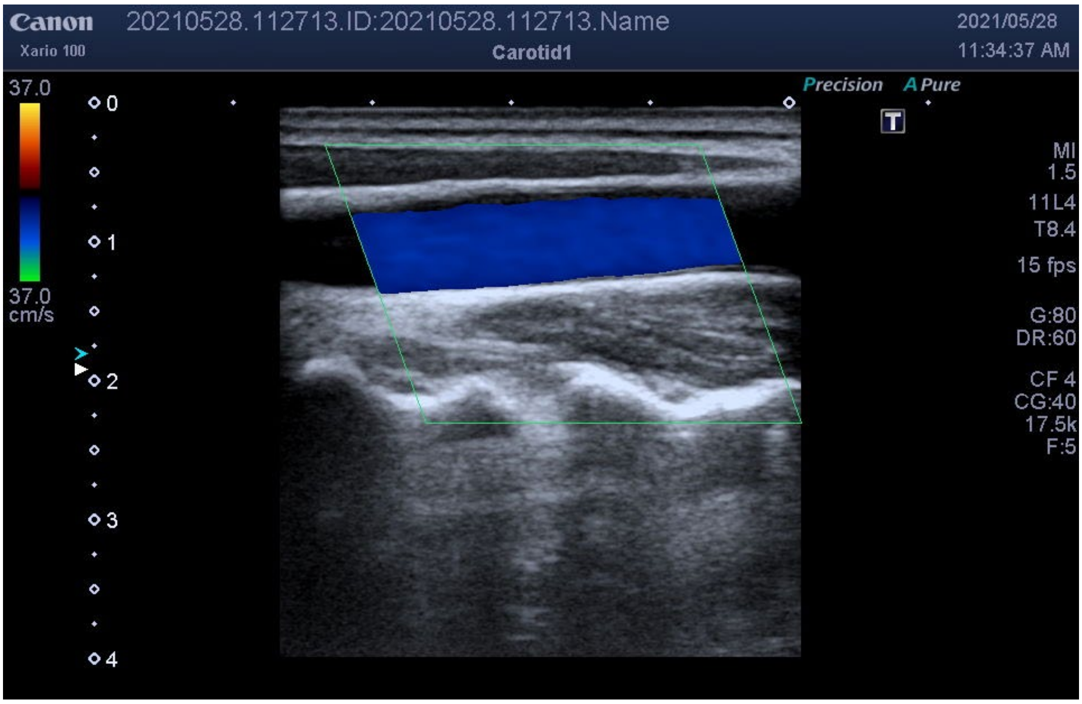

Figure 4.2. Color Doppler image of a carotid vessel

CDI works based on pulse Doppler method where an object velocity is estimated from phase difference of a successive ultrasonic wave at a given duration. On the CDI display, a 2D map of estimated particle velocity is visualized by color picture with a velocity scale. Blood flow toward the transducer is usually visualized as red color, while blue color is used for blood flow away from the transducer. The color intensity constitutes velocity magnitude, that is darker color for the lower velocity. Usually, the color Doppler image overlays a gray scale B-mode image. A color Doppler image of carotid vessels is shown in Figure 4.2. CDI is also used for measuring shear wave velocity or elastography. In the following sub-chapter, I will review the fundamental principles of Doppler flow techniques.

4.2.1 The Doppler effects

Doppler effect is described as perceived change in frequency due to relative motion of sound source and observer. The perceived frequency of a sound can be seen as effective periodicity of the wavefronts. If the source is approaching the observer with a velocity (C_S) in a medium with a speed of sound (C_0) then the arriving wavefront appear denser, giving an impression of higher acoustic frequency. On the other hand, sound velocity appears higher as an observer moves towards sound source at a speed C_{obs} [29].

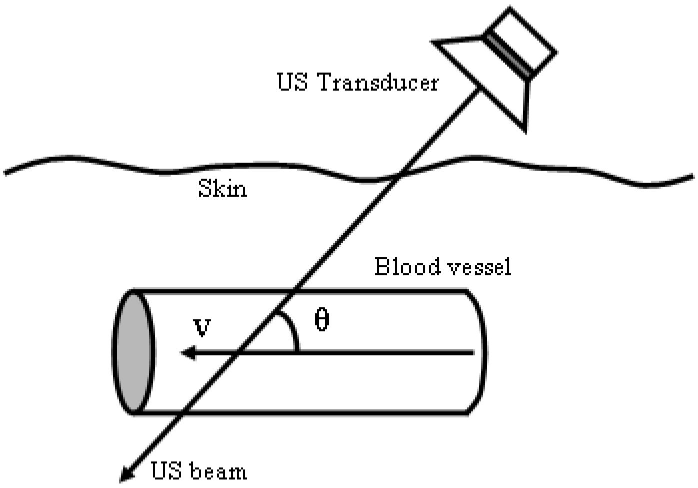

Figure 4.3. Blood flow measurement by Doppler technique

Both given examples can be formalized in a compact equation that covers all cases of motions, which may differ by an angle

$$f' = f\left(\frac{c_0 \pm c_{obs}\cos\theta}{c_0 \pm c_S\cos\theta}\right) \qquad \text{Eq. 19}$$

The measurement of blood flow with continuous wave (CW) Doppler is quite straight forward. A transducer consisted of two piezoelectric elements send an ultrasonic wave and receive its reflection at same time. For a blood velocity much smaller than sound speed, it is sufficient to approach [30]

$$f'' = f\left(1 - \frac{2v\cos\theta}{c}\right) \qquad \text{Eq. 20}$$

Therefore, Doppler shift frequency is

$$f_d = \frac{2v\cos\theta}{c} f \qquad \text{Eq. 21}$$

The received signal consisted of carrier frequency and other spurious signals in addition to the Doppler-shifted echo. Therefore, a signal processing involves amplification, demodulation, and band-pass filtering. It is obvious that the blood flow velocity is proportional to the Doppler shift echo. A typical diagram of CW flow meter is shown in Figure 4.4 [31].

4.2.2 Pulsed wave Doppler

The continuous wave Doppler is unable to differentiate reflection from two source in a same line of beam, such as overlapped artery and vein. This is commonly known as major limitation of the CW Doppler method. Pulsed wave Doppler which was capable to control the active region of measurement was proposed to overcome this issue. A pulsed Doppler system sends ultrasound pulses with a given length repetitively to a target at a certain range. Unlike the CW model of Doppler-shifted wavefronts, finite length pulses are used. For a transmitted waveform, $z_A(t)$, it is shown that the received Doppler shifted output signal has the form of [32]

$$z_B(t) = z_A\left[\boldsymbol{\Psi}\left(t - \frac{2d_0}{\Psi c}\right)\right] = z_A\left[\boldsymbol{\Psi}t - \frac{2d_0}{c_0}\right] \qquad \text{Eq. 22}$$

where d_0 is the distance to the target, and the Doppler scaling factor Ψ is

$$\boldsymbol{\Psi} = \mathbf{1} - \frac{2v\cos\theta}{c_0} = 1 - \delta_D \qquad \text{Eq. 23}$$

In CW Doppler, the Doppler-shifted received frequency is compared to the transmitted frequency; however, in range-gated pulsed Doppler, each received echo is compared to a similar echo resulting from the previous transmission. The relative delay between Doppler-shifted echoes from consecutive pulses is simply calculated by

$$t_d = \frac{2\Delta z}{c_0} = \frac{2T_{PRF}\, v\cos\theta}{c_0} = T_{PRF}\delta_D \qquad \text{Eq. 24}$$

where Δz is the distance traveled away from the transducer.

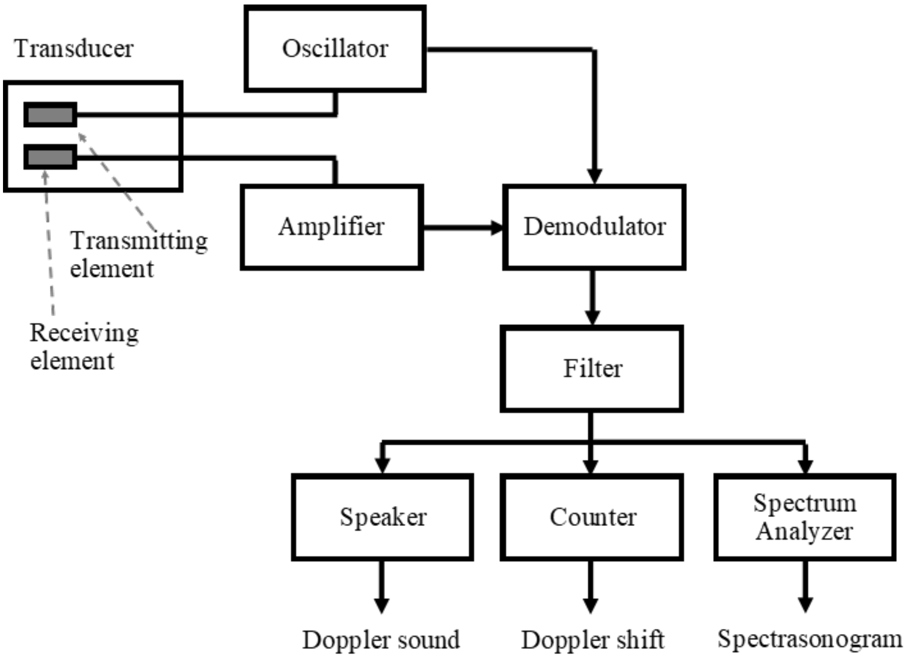

Figure 4.4. Continuous Wave (CW) Doppler block diagram

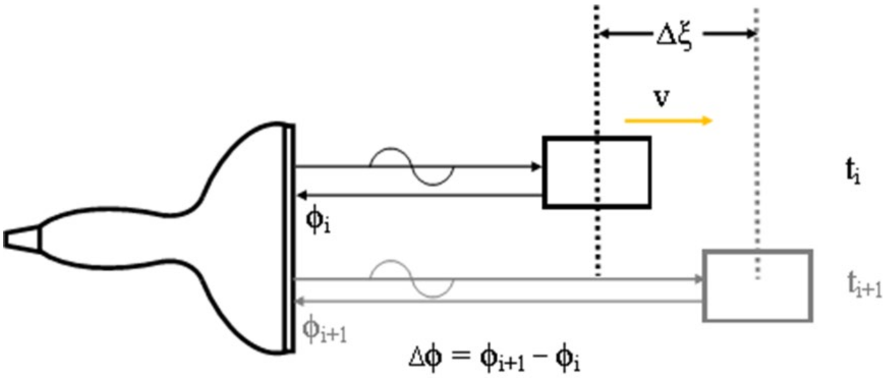

Figure 4.5. Pulsed wave Doppler illustration

As an alternative to the measurement of Doppler frequency shift, Doppler time-shift-based approach that calculate time domain cross-correlation are proposed [33] [34]. The basic principle is that the position of a cross-correlation gives the measurement of the Doppler time shift by red blood cell scatterers [35]. An autocorrelation function R_n is maximum when time shift is match $\tau = \tau_D$. When the time between repetitions is T_{PRF}, the Doppler velocity from the Doppler time shift equation is

$$v = \frac{c_0 \tau_D}{2T_{PRF} \cos\theta} \qquad \text{Eq. 25}$$

Furthermore, when the time shift is shorter that an ultrasonic wavelength, the estimation based on phase shift is considered more accurate. An ultrasonic phase shift can be used as it is proportional to scatterer displacement or velocity.

When two pulses of ultrasonic waves are transmitted in a sequence, the Doppler phase shift between the pulses can be analyzed. The phase shift analysis is based on the principle that when the second pulse hits a moving scatterer, the scatterer has been displaced farther or closer from the probe, and the second pulse echo will be in a different phase from first pulse. The displacement of scatterer will be a proportional function of the scatterer velocity and the pulses time interval.

Therefore, the phase analysis is based on the phase shift from a pulse sequence, instead of the apparent wavelength change by the motion of the source or observer. The phase shift from subsequent pulses can be viewed as the wavelength change in a continuous wave, therefore, both phenomena are intuitively equal. A scatterer motion of at a distance d is equal to the elapsed time multiplied by scatterer velocity. In the case of flow measurement, the displacement by scatterer velocity is doubled (2d) since a scatterer acts as a reflector which is a receiver and source at the same time.

In a pulsed Doppler, the time between the two pulses represent Δt = 1/PRF. By shooting multiple pulses in the same direction, a new signal with one sample from each pulse is produced. The Doppler curve from this signal will be a new curve with the frequency equal to the Doppler shift. In this case, as a wavelength λ equals 2π, the displacement (2d) of second pulse in relation to the first pulse relative to λ equals the phase shift Δϕ relative to 2π. Therefore,

$$\frac{2d}{\lambda} = \frac{\Delta\phi}{2\pi} \ . \qquad \text{Eq. 26}$$

As $d = v{*}\Delta t$, and $\lambda = c/f$,

$$\frac{2v\Delta t f_0}{c} = \frac{\Delta\phi}{2\pi} \ . \qquad \text{Eq. 27}$$

a phase shift can be expressed as a proportional function of velocity

$$\Delta\phi = \frac{2\pi f_0}{c} 2v\Delta t \ . \qquad \text{Eq. 28}$$

One of an effective method to obtain phase difference of an ultrasonic pulse sequence from a quadrature detector is described by autocorrelator technique.

4.2.3 Autocorrelator technique

In the original article of autocorrelation method, it is explained that The phase ϕ of ultrasound echo is obtained as the argument of $R(T, t)$, that is

$$\phi(T,t) = tan^{-1}\frac{R_y(T,t)}{R_x(T,t)} \ , \qquad \text{Eq. 29}$$

where

$$\begin{aligned} R(T,t) &= \int_{t-nT}^{t} z_1(t')dt' \\ &= R_x(T,t) + jR_y(T,t) \ . \qquad \text{Eq. 30} \end{aligned}$$

In this equation,

$$z_1(t) = z(t) \times z^*(t-T) \ , \qquad \text{Eq. 31}$$

While an ultrasonic wave is composed of a complex signal and its conjugate

$$z(t) = x(t) + jy(t)$$

$$z^*(t-T) = x(t-T) - jy(t-T) \quad . \qquad \text{Eq. 32}$$

When it is interpreted in the discrete integration, for N packet size of successive ultrasonic wave, the average phase shift could be obtained by autocorrelator [36].

$$\Delta\phi_i = \begin{cases} \tan^{-1}\frac{E_U}{E_L} + \pi & \text{if } E_U > 0, E_L < 0, \\ \tan^{-1}\frac{E_U}{E_L} & \text{If } E_L > 0, \\ \tan^{-1}\frac{E_U}{E_L} - \pi & \text{if } E_U < 0, E_L < 0, \end{cases} \qquad \text{Eq. 33}$$

where

$$E_U = \sum_{i=-\frac{N}{2}}^{\frac{N}{2}} I_i Q_{i+1} - I_{i+1} Q_i \quad \text{, and}$$

$$E_L = \sum_{i=-\frac{N}{2}}^{\frac{N}{2}} I_{i+1} I_i + Q_{i+1} Q_i \quad . \qquad \text{Eq. 34}$$

The autocorrelator integration duration is given by $T_a = N\Delta t$. Therefore,

$$\Delta t = \frac{T_a}{N} \quad . \qquad \text{Eq. 35}$$

4.3 Doppler Measurement of Sinusoid Vibration

The key concept of color Doppler elastography is by using Color Flow Imaging (CFI) to visualize tissue vibration instead of blood flow in two-dimensional map. In a pulsed wave Doppler method, a sequence of ultrasound pulses with an interval Δt is radiated. When this pulse is reflected by a flow with a velocity v, the phase of received ultrasonic wave is shifted proportionally to the flow velocity

$$\Delta\phi_i = \frac{2\pi f_0}{c} 2 v_i \Delta t \quad . \qquad \text{Eq. 36}$$

Therefore, a flow velocity is estimated from ultrasound phase shift by

$$\hat{v} = \frac{c}{4\pi f_0 \Delta t} \Delta\phi_i \quad . \qquad \text{Eq. 37}$$

Suppose a Color Doppler Imaging (CDI) method is applied to observe a propagating shear wave with a sinusoid displacement

$$\xi_i = \xi_m \sin(\omega_b t + \phi_b) \quad , \qquad \text{Eq. 38}$$

where ξ_m is maximum displacement and $\omega_b = 2\pi f_b = \frac{2\pi}{T_b}$ is shear wave angular frequency. The phase of the received ultrasonic wave is

$$\phi_i = \phi_0 + \frac{2\pi f_0}{c} * 2\xi_i \quad , \qquad \text{Eq. 39}$$

and the received RF signals by a quadrature detector are

$$I_i = a\cos\left(\phi_0 + \frac{4\pi f_0}{c} * \xi_i\right) \quad \text{and}$$

$$Q_i = a\sin\left(\phi_0 + \frac{4\pi f_0}{c} * \xi_i\right) \quad . \qquad \text{Eq. 40}$$

In general, the flow velocity is estimated as a function of autocorrelator integration duration T_a and shear wave angular frequency ω_b (see Appendix),

$$\begin{aligned} \hat{v} &= \frac{2c}{4\pi f_0 T_a} \frac{4\pi f_0}{c} \xi_m \cos(\omega_b t + \phi_b) \sin\left(\omega_b \frac{T_a}{2}\right) \\ &= \frac{2\xi_m \cos(\omega_b t + \phi_b) \sin\left(\omega_b \frac{T_a}{2}\right)}{T_a} \quad . \end{aligned} \qquad \text{Eq. 41}$$

Since velocity is a derivative of displacement, which is

$$\begin{aligned} v &= \frac{d\xi}{dt} \\ &= \frac{d\xi_m \sin(\omega_b t + \phi_b)}{dt} \\ &= \omega_b \xi_m \cos(\omega_b t + \phi_b) \quad , \end{aligned} \qquad \text{Eq. 42}$$

the Eq. 41 can be substituted to Eq. 42 to get the real velocity from the measurement by

$$v = \hat{v} \frac{T_a \omega_b}{2\sin\left(\omega_b \frac{T_a}{2}\right)} \quad . \qquad \text{Eq. 43}$$

Multiple value of v can be measured by a single measurement since T_a can be altered by changing the number of pulses that is used in the calculation. In this case, the real velocity is approximated by least square method.

In a very high PRF relative to the shear wave frequency so that $T_a \approx 0$, the estimated velocity is approaching the real velocity v. On the other hand, when autocorrelator integration duration T_a is an integer multiple of shear wave period T_b, the estimated velocity is approaching zero. An exception to this situation is when the vibration amplitude is larger than λ/8 and the packet size is a multiple of 4. In this case, the estimated velocity can be either zero or maximum velocity as suggested by binary pattern color Doppler elastography [37].

Now, the ratio of the real vibration velocity and the measured velocity is given by

$$\beta_v = \frac{\hat{v}}{v}$$

$$= \frac{2 \sin\left(\omega_b \frac{T_a}{2}\right)}{T_a \omega_b} \quad , \qquad \text{Eq. 44}$$

which is a function of normalized integration time T_a/T_b. It is worth noting that T_a is a parameter belong to the color Doppler imaging system, while T_b is a property of the shear wave. Since T_a only affects the amplitude of velocity estimation without any impact to the phase, it does not affect the estimation of shear velocity. This formalization implies that any color Doppler imaging system can be used to visualize a shear wave propagation as long as its autocorrelator integration time T_a is not an integer multiple of shear wave vibration period, except on the binary pattern elastography. Nevertheless, the velocity estimation error can be corrected by β_v factor when T_a and T_b are known. Figure 4.6 reveals graphical plot of velocity ratio β_v in respect to the normalized autocorrelator integration time T_a/T_b.

Since the ultrasound phase shift is calculated by arctan function, it is mandatory to keep $-\pi/2 < \Delta\phi_i < \pi/2$ to avoid aliasing. Therefore,

$$-\frac{\pi}{2} < \frac{2\pi f_0}{c} 2 v_i \Delta t < \frac{\pi}{2} \quad . \qquad \text{Eq. 45}$$

This is equivalent to

$$v_m < \frac{\lambda}{8\Delta t} \quad .$$

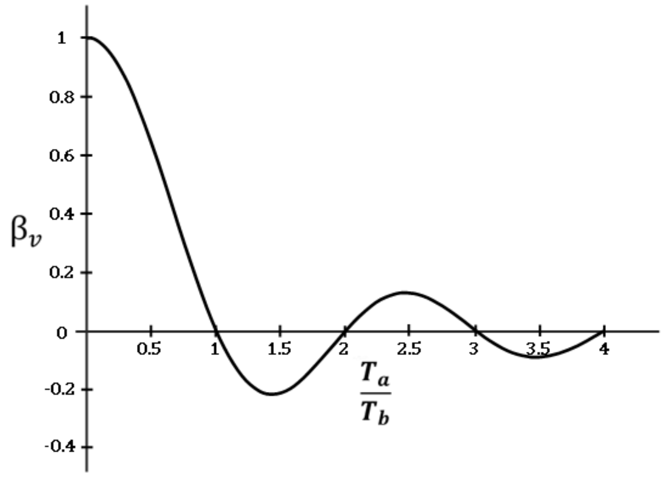

Figure 4.6. Velocity index as a function of normalized acquisition time

Since velocity is derivative of displacement, the constraint for maximum shear wave displacement is

$$\omega_b \xi_m < \frac{\lambda}{8\Delta t} \quad . \qquad \text{Eq. 46}$$

This region of operation belongs to small displacement method since it involves small amplitude of vibration to avoid aliasing.

4.4 Elastography by Means of Color Doppler Imaging

As aforementioned, elasticity of a material can be calculated by measuring shear wave velocity propagating in it [26]. It was found that two interfering shear waves could produce either static or moving pattern with which the shear wave wavelength can be calculated from its spacing or apparent velocity [38]. It was some years before the theory of crawling wave was expanded, and the shear velocity estimation and imaging technique was improved. That crawling wave method used two vibrators to produce the interference pattern [39].

A shear wave could be induced inside a tissue from a high-intensity ultrasonic wave which is produced by an ultrasonic wave transducer. That shear wave velocity is then measured by an ultrasound imaging system with a high frame rate, leading to the Acoustic Radiation Force Impulse (ARFI) imaging method [40]. Since the induced shear wave frequency is typically higher than the pulse repetition frequency (PRF), a high frame rate is needed for that system. A shear wave wavefront mapping using ultrasound Color Doppler Imaging (CDI) was proposed to overcome the high frame rate requirement. In that method, a sequence of binary color flow images is produced, and shear wave velocity and propagation direction map are reconstructed accordingly. By that method, a relatively high shear wave frequency in respect to the PRF of a general-purpose ultrasound imaging system can be recovered. However, that method requires precise control to the pulsed Doppler autocorrelator packet size as well as shear wave displacement amplitude and frequency condition [37].

The captured shear wave shadow by a commercial US machine suggested that interference pattern on a CDI image can be produced by the propagating shear wave and the ultrasonic transducer array scanning process. The frequency of that interference pattern is proportional to the shear wave wavenumber. However, the correct value of the shear wave wavenumber cannot be determined before removing the scanning delay effect. In this sub-chapter, I will discuss a theory on CDI image formation, when it is used for observing a shear wave. From the theory, a shear wave imaging system with one vibrator without a strict constraint on the shear wave displacement amplitude and frequency condition as well as autocorrelator packet size can be implemented. As a result, a shear wave velocity map can be recovered from a typical scanning array transducer leading to a more practical imaging system. This method could be developed to be used in clinical practice for detecting tissue elasticity related disease.

A typical CDI system is optimized for low velocity blood flow. When this type of system is used for detecting high frequency sinusoid tissue vibration, it displays a deviated value due to ultrasound phase estimation error and scanning process of ultrasonic transducer array. The ultrasound phase estimation error results in lower flow velocity estimation, while the scanning process of ultrasonic transducer array causes incorrect shear wave reconstruction. A theory to estimate vibration amplitude by on phases operations has been described [41]. However, it is not applicable for most general-purpose ultrasound system since the phase difference of individual pulses are not available.

A hardware of color Doppler shear wave elastography is shown in Figure 4.7. It consists of a mechanical vibration source assembled near an ultrasound array transducer. A shear wave is externally induced by a vibration source and propagated in the medium. When a common Color Doppler Imaging (CDI) system is used, a sequence of ultrasonic pulses is radiated to the medium. The phase of reflected signal by this medium is shifted proportionally to the sinusoidal displacement of the shear wave. A quadrature detector catches this signal and produces complex valued output.

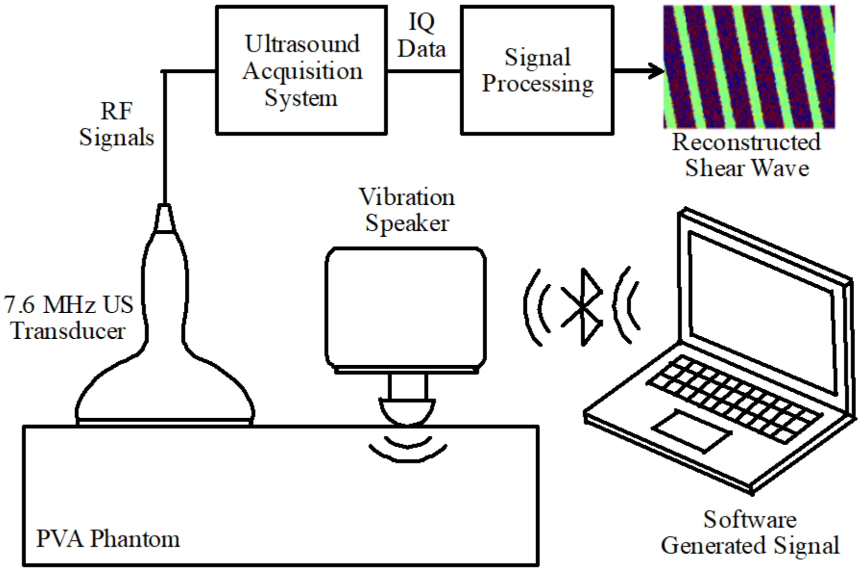

Figure 4.7. Hardware setup in color Doppler elastography.

4.4.1 Binary pattern color Doppler image

The binary pattern shear wave elastography can be considered as a special case of color Doppler elastography, where a special condition of shear wave frequency and amplitude is required. Under the given condition, the flow velocity appears as binary pattern on the color Doppler image.

According to the reference, the shear wave frequency condition f_b is given by

$$f_b = \frac{1}{2}\left(m - \frac{1}{2}\right)\frac{1}{\Delta t} \quad , \qquad \text{Eq. 47}$$

where Δt is successive ultrasonic pulses repetition interval of color flow velocity estimation, and m is a non-negative integer value. The displacement amplitude requirement is derived from a condition when the estimated flow velocity is the maximum, leading to

$$\frac{1}{8}\lambda < \xi_0 < \frac{3}{8}\lambda \quad . \qquad \text{Eq. 48}$$

Under the two conditions the shear wave map is reconstructed from repeating pattern of zero and maximum flow velocities in Color Doppler Image (CDI) system.

Since shear wave displacement is assumed as a sinusoid, the output signal of quadrature detector become

$$I_i = a\cos\left(\phi_0 + \frac{4\pi f_0}{c}\xi_0 \sin(\omega_b t + \phi_b)\right) \quad \text{and} \qquad \text{Eq. 49}$$

$$Q_i = a\sin\left(\phi_0 + \frac{4\pi f_0}{c}\xi_0 \sin(\omega_b t + \phi_b)\right) \quad .$$

By the autocorrelation, the value of velocity can be calculated for the given vibration frequency by

$$\hat{v} = \frac{c}{4\pi f_0 \Delta t}\tan^{-1}\frac{E_U}{E_L} \quad , \tag{Eq. 50}$$

where

$$E_U = \sum_{i=-\frac{N}{2}}^{\frac{N}{2}} I_i Q_{i+1} - I_{i+1} Q_i \quad \text{and}$$
$$E_L = \sum_{i=-\frac{N}{2}}^{\frac{N}{2}} I_{i+1} I_i + Q_{i+1} Q_i \quad . \tag{Eq. 51}$$

It can be seen from the formula that the pattern of binary flow velocity can be simulated as a function of maximum displacement ξ_0 and vibration phase $\omega_b t + \phi_b$. The value of maximum velocity

$$v_{max} = \frac{c}{4 f_0 \Delta t} \quad . \tag{Eq. 52}$$

was derived when E_L is negative and E_U is zero. This is correct when $E_U = 0^+$. However, in the case of $E_U = 0^-$, the value of v_{max} becomes negative since calculation of *atan* division move abruptly from quadrant II to the quadrant III. This principle explained the mixture of positive and negative value of binary pattern in the simulation.

4.4.2 Elastography with a commercial US machine

In more generalized cases, when color Doppler imaging is carried out by a commercial ultrasound machine, the velocity estimation of a propagated shear wave in a medium on the (x, z) plane by an ultrasonic transducer array is expressed by

$$\hat{v}(x,z) = \frac{2\xi_m \sin\left(\omega_b \frac{T_a}{2}\right)}{T_a}\cos(2\pi f_b t + 2\pi K_x x + 2\pi K_z z + \phi_b)\cos(\alpha) \quad , \tag{Eq. 53}$$

where α is angle of incidence between ultrasound beam and the shear wave displacement, which is perpendicular to the shear wave propagation direction. Therefore,

$$\hat{v}(x,z) = \frac{2\xi_m \sin\left(\omega_b \frac{T_a}{2}\right)}{T_a}\cos(2\pi f_b t + 2\pi K_x x + 2\pi K_z z + \phi_b)\cos\left(\tan^{-1}\frac{K_z}{K_x}\right)$$

$$= \frac{2\xi_m \sin\left(\omega_b \frac{T_a}{2}\right)}{T_a} \cos(2\pi f_b t + 2\pi K_x x + 2\pi K_z z + \phi_b) \frac{K_x}{\sqrt{{K_x}^2 + {K_z}^2}} \quad . \qquad \text{Eq. 54}$$

It can be seen that shear wave velocity could be determined from measurement of wavenumber K_x and K_z in spatial dimension. However, line scanning in ultrasound imaging process changes the appearance of color Doppler image which obscures K_x and K_z. For instance, a 1 mS transmit interval between each scanning line when imaging 200 Hz shear wave vibration means that after 5 transmissions, the medium has completed a cycle of vibration. Consequently, the 6th line has a same phase with 1st line, meanwhile prevalent phase shifts occur to all beams in between. Let

$$\frac{2\xi_m \sin\left(\omega_b \frac{T_a}{2}\right)}{T_a} \frac{K_x}{\sqrt{{K_x}^2 + {K_z}^2}} = v_m$$

and shear wave initial phase $\phi_b = 0$. If ultrasound beam scanning has a lateral transmission delay of ΔT_p per unit length (unit: s/m), there is a shear wave wavenumber shift on lateral direction that is observed in the flow velocity map, that is

$$\begin{aligned} \hat{v}(x,z) &= v_m \cos\left(2\pi f_b\left(t + x\Delta T_p\right) + 2\pi K_x x + 2\pi K_z z\right) \\ &= v_m \cos\left(2\pi f_b t + 2\pi f_b \Delta T_p x + 2\pi K_x x + 2\pi K_z z\right) \quad . \qquad \text{Eq. 55} \end{aligned}$$

It can be seen from Eq. 55 that the shear wave appears denser or sparser on the CDI images, depending on the sign of ΔT_p which physically means the scanning direction.

Consider a sequence of CDI images, with a framerate of *R* is used. Now, the velocity as a function of frame number *n* and framerate given by

$$\hat{v}(x,z) = v_m \cos\left(2\pi f_b \left(\frac{n}{R}\right) + 2\pi(f_b \Delta T_p + K_x)x + 2\pi K_z z\right) \quad .$$

In a condition when frame interval is even multiple of half shear wave period which gives

$$\frac{1}{R} = (2k)\frac{1}{2f_b} \quad ,$$

then

$$\hat{v}(x,z) = v_m \cos\left(2kn\pi + 2\pi(f_b \Delta T_p + K_x)x + 2\pi K_z z\right) \quad . \qquad \text{Eq. 56}$$

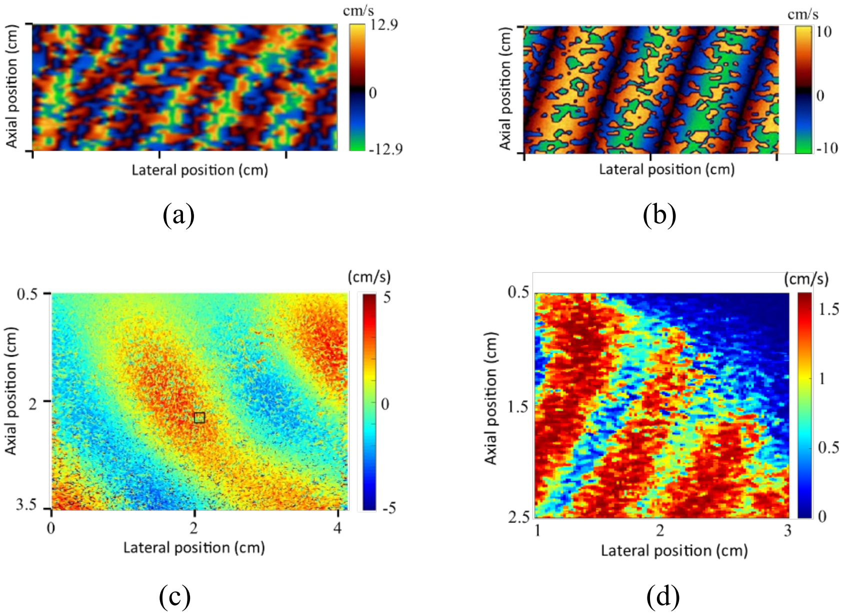

(a) (b)

(c) (d)

Figure 4.8. Color Doppler images of shear wave by different methods

Since phase shift of each subsequent frame is a multiple of 2π, the color Doppler image will display same pattern in all frames. On the other hand, when frame interval is odd multiple of half shear wave period,

$$\frac{1}{R} = (2k+1)\frac{1}{2f_b} \quad ,$$

then

$$\hat{v}(x,z) = v_m \cos\big((2k+1)n\pi + 2\pi(f_b \Delta T_p + K_x)x + 2\pi K_z z\big) \quad . \qquad \text{Eq. 57}$$

In this condition, the subsequent color Doppler frames will appear as the same sinusoid but with inverted sign. As a result, when the two subsequent frames are combined, the algorithm may detect ambiguity of the sinusoid sign. It might come out as modulated sinusoid surfaces with a proportional wave number to the observed shear wave. If absolute value of $\hat{v}$ is taken, the shear wave wavelength can be calculated from twice of the strips followed by scanning delay compensation.

This principle apparently underlies a typical flow imaging result of vibrating phantom with a commercial ultrasound machine. Color Doppler measurement to a shear wave by a commercial ultrasound machine as seen in Figure 4.8 (a) much resembled a simulated interleaved color Doppler image in Figure 4.8 (b), rather than what in the high frame rate imaging of small displacement vibration in Figure 4.8 (c) or binary pattern CDI in Figure 4.8 (d). At this point, the shear wave wavenumber can be resolved only if scanning delay ΔT_p is known, which can be obtained from calibration. From both Eq. 56 and Eq. 57, the sinusoid surface can be recovered by envelope processing to become

$$\hat{v}_r(x,z) = v_m \cos\left(\phi_t + 2\pi(f_b \Delta T_p + K_x)x + 2\pi K_z z\right) \quad . \qquad \text{Eq. 58}$$

The relationship between the actual shear wave wavenumber and the observed wavenumber under the effect of ΔT_p are given by

$$K0_z = K_z$$

$$K0_x = K_x + f_b \Delta T_p \qquad \text{Eq. 59}$$

4.4.3 Phase spectrum signal processing

A typical phase spectrum signal processing is shown in Figure 4.9. In a research purpose ultrasound machine, IQ data are decomposed, and the spectrum of the moving images are analyzed. The flow velocity reconstruction follows the pulse Doppler method which is derived from the autocorrelation techniques [36]. By repeating the process to all area, the shear wave velocity map is recovered. Instead of IQ data, a commercial ultrasound machine produced a color Doppler measurement in the form of DICOM formatted movie file. In the signal processing, the envelope detection takes an absolute value of the CDI images, resulting in strip patterned movies.

The same spectrum analysis is performed along time dimension for every pixel of CDI image and the fundamental frequency is determined. On that fundamental frequency, the phase spectrum is obtained for each pixel. The value of wavenumber is calculated from spatial derivative of the phase map followed by a compensator to remove the effect of scanning delay on the lateral direction. The shear wave velocity and propagation direction are obtained at the end of the processing.

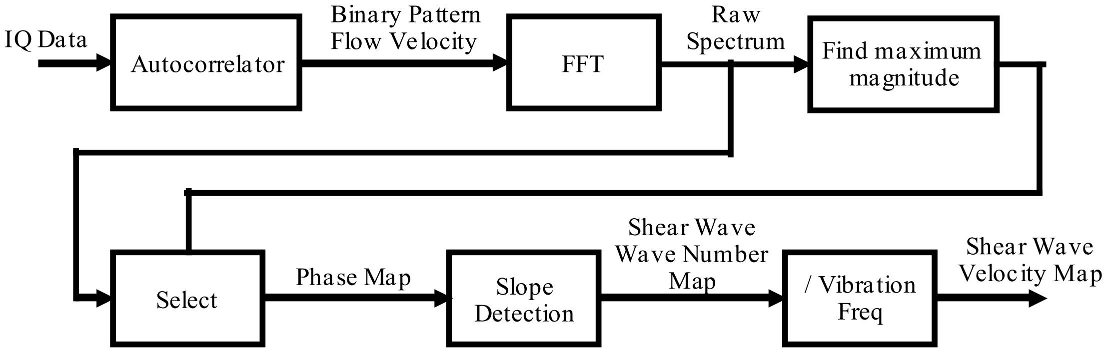

Figure 4.9. Signal processing framework of color Doppler elastography

4.5 Experiments

In this sub-chapter, I will present experiment results as a proof of theoretical concept about amplitude deviation due to autocorrelator acquisition time, binary pattern simulation on the shear wave wavefront mapping by different amplitude, binary pattern elastography of homogeneous phantoms, and mechanically induced color Doppler elastography of homogeneous and non-homogeneous phantom. The first experiment was performed to demonstrate the relation between autocorrelator integration time T_a and the estimated flow velocity. The last two experiments were carried out with a commercial ultrasound machine when shear wave frequency and amplitude condition to observe binary pattern on the CDI are not satisfied.

4.5.1 Vibration amplitude correction

In the sub-chapter 4.3, I have stated that the observed flow velocity under Doppler measurement is changed by the factor of β_v. This experiment is aimed to proof this theory by measuring the velocity of a vibrating phantom by different autocorrelator integration time T_a. The hardware setup for this experiment is shown in Figure 4.7. A sinusoid vibration was generated by MATLAB® software and delivered to a 3-watt wireless vibration speaker (EWA A106 Pro) with a 15 mm × 40 mm hemisphere shaped actuator head. The vibration source is attached to the surface of the 6% Polyvinyl Alcohol (PVA) phantom on the same line with a 7.6 MHz 128 channel array linear probe. A research purpose ultrasound system (Verasonics, The Vantage 256™, Kirkland, USA) is used for ultrasound acquisition. The resulting IQ data are processed with MATLAB® script to reconstruct the vibration and analyze the velocity by pulsed Doppler method. As a comparing data, the amplitude of vibration is measured by speckle tracking B-mode image of the IQ data. In this experiment, the vibration frequency is set to 150 Hz and the PRF is 3000 Hz.

The PVA phantoms are made from mixture of Polyvinyl Alcohol (PVA) granules (JF-17, Japan Vam & Poval Co., Ltd.), water (H_2O) and the Dimethyl Sulfoxide (DMSO) liquid (043-07211, Fujifilm Wako Pure Chemical Industries, Ltd.) by weight ratio of $\frac{w}{100} : 0.2(1 - \frac{w}{100}) : 0.8(1 - \frac{w}{100})$, where w is total weight of the phantom. 1 g cellulose powder (036-22225, Fujifilm Wako Pure Chemical Industries, Ltd.) is added for every 100 g of phantom as reflector. The vibration velocity on the target is estimated by different value of autocorrelator integration time (T_a).

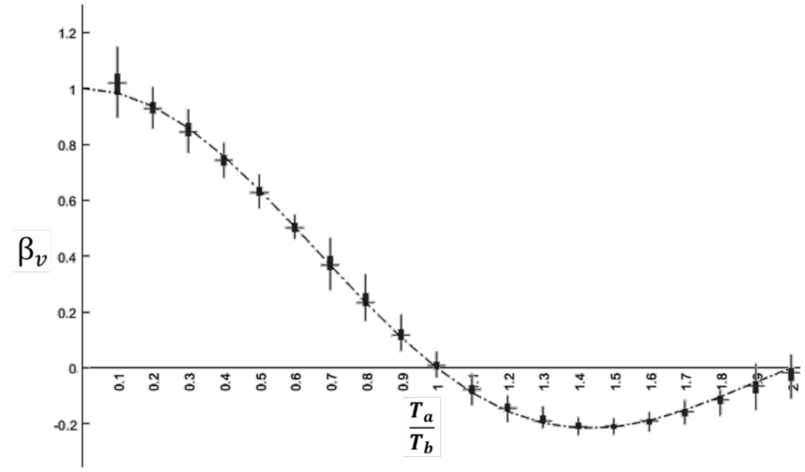

Figure 4.10. Estimated to real velocity ratio

In practice, the measurement may be performed once, and the various value of T_a are obtained by varying the number of samples from 3 to 41 to get different packet size value. The calculation was repeated to 60 different ROIs which are chosen randomly on the image to measure velocity correction factor β_v with different normalized autocorrelator integration time (T_a/T_b).

It can be seen in Figure 4.10 that the measured value of β_v with different T_a/T_b follows a theoretical curve. The real flow velocity for each ROI can be recovered accordingly. By considering velocity correction factor β_v, the real flow velocity is estimated.

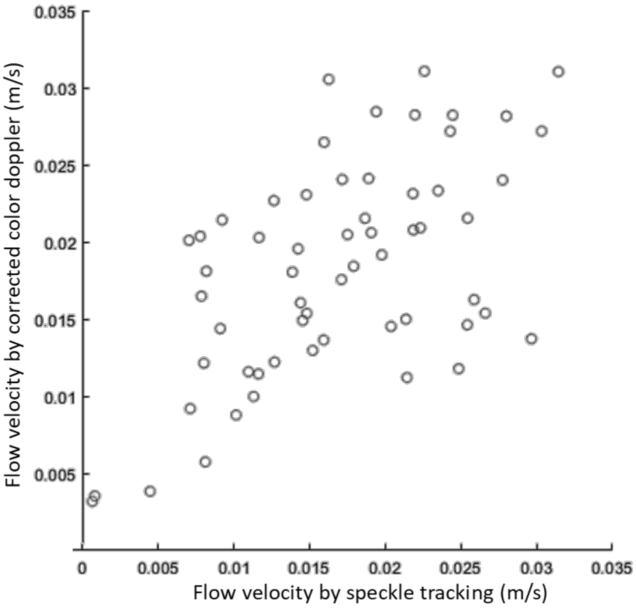

Figure 4.11. Flow velocity by corrected pulse Doppler and speckle tracking

I compared the corrected flow velocity with speckle tracking of B-mode image on the 60 different locations. It can be seen in Figure 4.11 that the flow velocity by corrected pulse Doppler are very similar with the measurement by B-mode image speckle tracking. The deviation may exist due to the inacuracy of measurement. However, this image indicate that the sinusoid flow velocity estimation by pulsed Doppler method could be improved by taking account the autocorrelator integration time (T_a) to the calculation.

4.5.2 Binary pattern simulation

A simulation is performed to visualize the effect of changing shear wave amplitude in the binary pattern color Doppler elastography. An ultrasonic frequency f_0 = 7.6 MHz and sound speed c = 1540 m/s are used. To follow the frequency condition, PRF = 800 Hz, and shear wave frequency f_b =200 Hz are chosen. Figure 4.12 shows binary pattern in color Doppler elastography with different amplitudes of shear wave. A cycle of shear wave at amplitude of λ/4 is plotted in Figure 4.12 (a) with the simulated binary pattern of different amplitudes as in Figure 4.12 (b). It can be seen from the image that each period of shear wave with suggested amplitude produced four cycles of binary pattern in the color flow estimation. However, it possible to expand the range of amplitude such up to $\xi_0 = \lambda$. The binary pattern appears more frequent with higher shear wave amplitude and the duty ratio is altering.

By calculation from Eq. 52, the maximum velocity in this simulation is 0.0405 m/s. Figure 4.13 shows a simulation result of a shear wave with a propagating speed of 5.353 m/s at an angle of 15.524° traveling in a 2 x 4 cm phantom. Figure 4.13 (a) shows the shear wave when ξ_0 is λ/4. Figure 4.13 (b), (c) and (d) shows the resulting binary pattern by color Doppler image when the ξ_0 is λ/4, λ/2, and 13λ/16, respectively. It can be clearly seen that the binary pattern changes due to the change of shear wave amplitude.

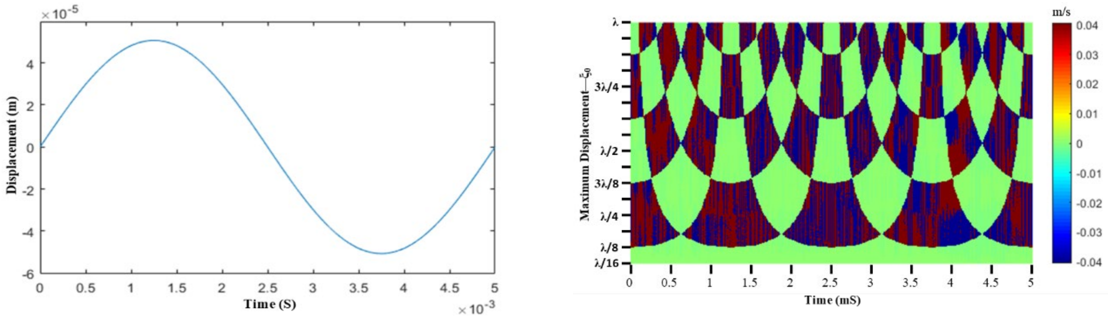

(a) (b)

Figure 4.12. Effect of shear wave amplitude in color Doppler pattern

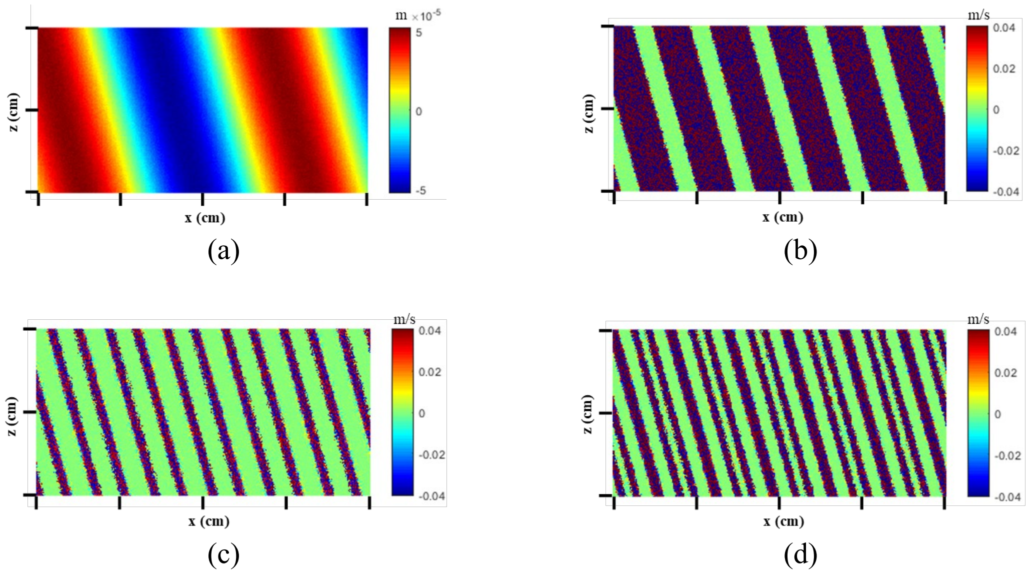

(a) (b) (c) (d)

Figure 4.13. Binary pattern of a shear wave with different amplitude

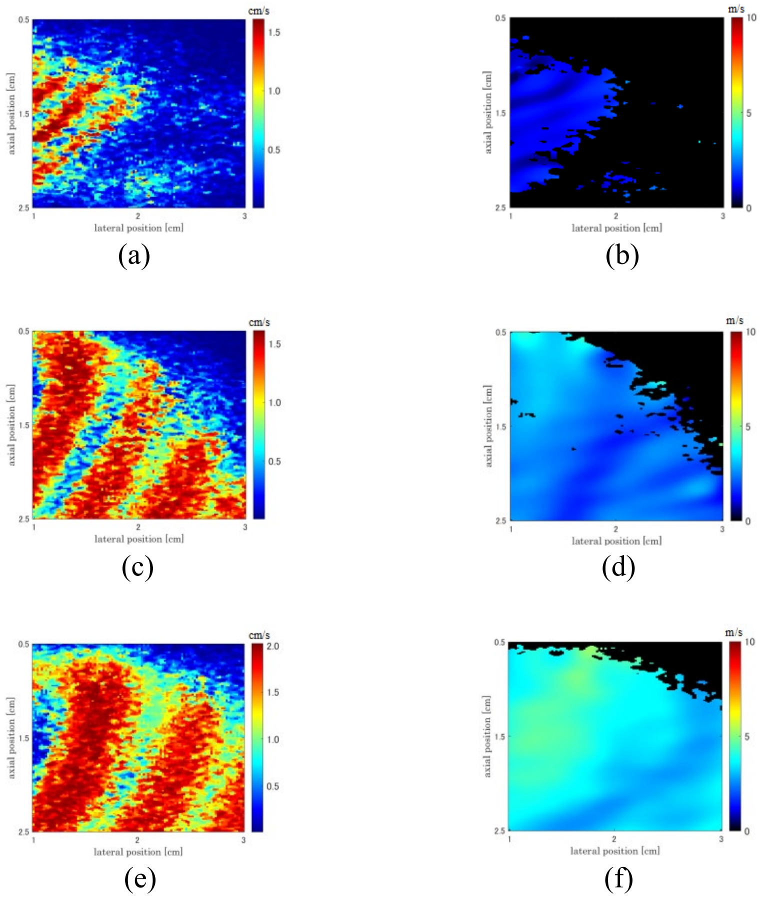

(a) (b) (c) (d) (e) (f)

Figure 4.14. Phantom experiment footage

4.5.3 Binary pattern elastography of homogeneous phantoms [42]

An experiment was performed by exciting 100 Hz vibration from a speaker with an actuator head to PVA phantoms. An ultrasonic imaging system with a 7.6 MHz linear probe of 128 channel array is adopted to observe CDI with Pulse Repetition Frequency (PRF) is set to 400 Hz. The binary pattern footage and shear wave velocity maps by measurement of 4%, 6%, and 8% phantoms are shown in Figure 4.14 (a, c, and e).

4.5.4 Shear wave velocity mapping of homogeneous phantoms

On the other experiments, I have measured shear wave velocity of 6%, 8% and 10% PVA phantoms by a Xario 100 (Canon, Japan) ultrasound machine with a 7 MHz linear array transducer (PLU-704 BT). The shear wave vibration frequency is 300 Hz. The 1 cm × 2.4 cm Region of Interest (ROI) is selected 1 cm below the phantom surface. The PRF is 17.1 KHz with a frame rate of 11 giving flow velocity scale of ±12.9 cm/s. All built in filtering configuration is set to minimum.

The exact scanning delay is unknown and always changed following the CDI configuration change. Therefore, a setting with the best visual is calibrated by the measurement of the same phantom with a synchronized Doppler (Verasonics, The Vantage 256™, Kirkland, USA) and is saved in a user preset for the other phantom measurements. The measurement result is saved as a DICOM formatted file and moved to the PC for subsequent processing with a MATLAB® software. The shear wave propagation velocity and direction were calculated accordingly based on the phase spectrum analysis.

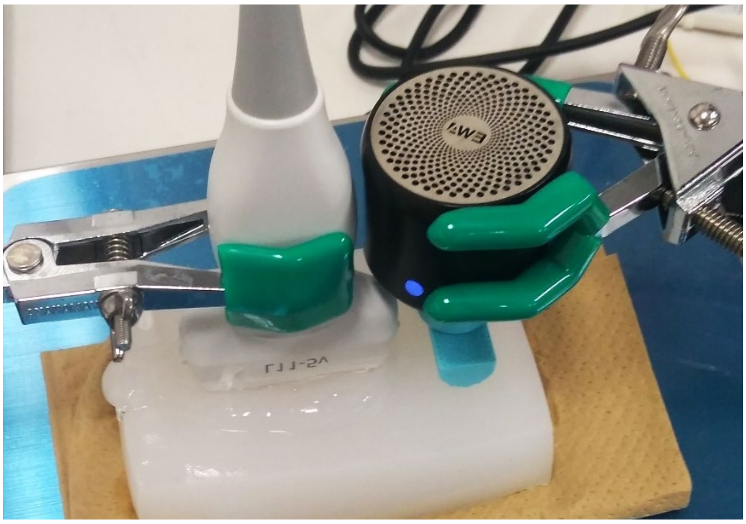

Figure 4.15. Photograph of shear wave elastography measurement

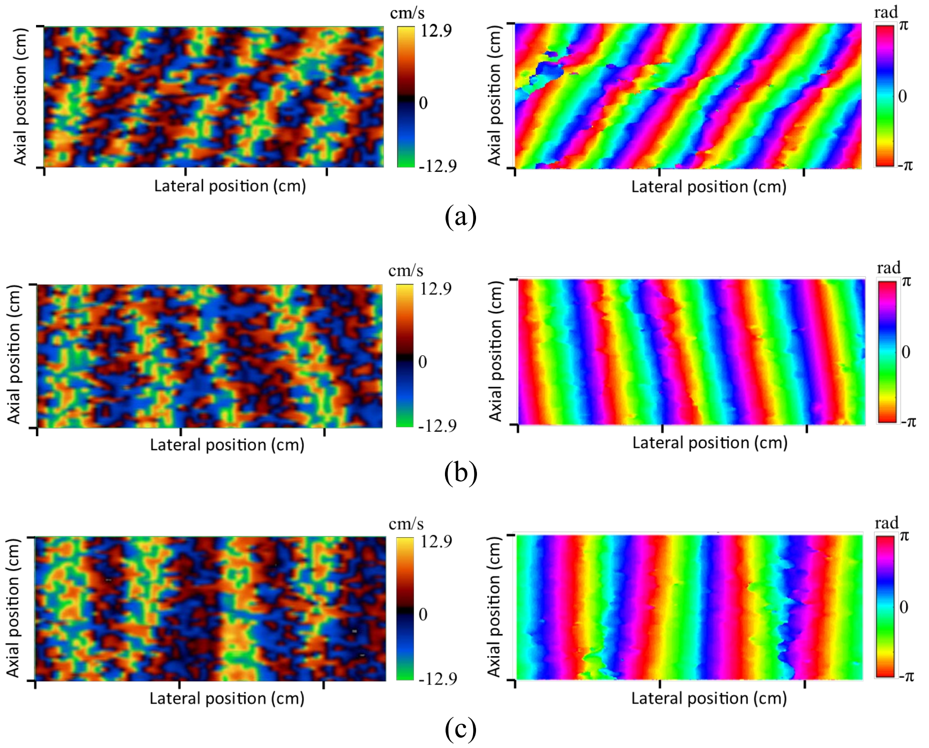

(a)

(b)

(c)

Figure 4.16. Color flow image and phase map of a shear wave

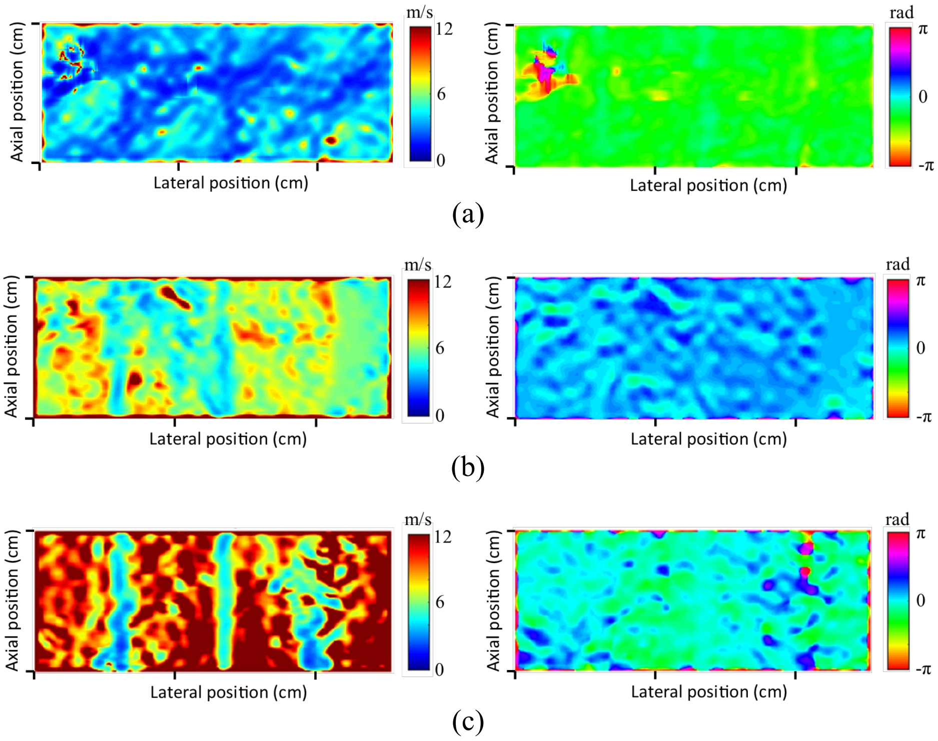

(a)

(b)

(c)

Figure 4.17. Shear wave velocity and propagation direction in PVA phantoms

Figure 4.16 shows volor flow image (left) and phase map (right) of a shear wave in 6% (a) 8% (b) and 10% (c) PVA phantoms by a commercial ultrasound machine. As the PVA phantom increase, the color flow image displays longer wavelength. After the phase spectrum analysis is performed, a shear wave velocity and propagation direction map are produced.

The Figure 4.17 shows shear wave velocity (left) and propagation direction (right) in 6% (a) 8% (b) and 10% (c) PVA phantoms respectively. It is demonstrated that the method correctly displays the stiffer phantom with the higher shear wave velocity. I compared the method which uses a commercial ultrasound (US) machine with measurement by a research purpose US machine (Verasonics, The Vantage 256™, Kirkland, USA), where lateral delay is set absent. A measurement set-up is shown in Figure 4.15. Table 3 shows that the method is capable to determine the shear wave velocity with a small error.

Table 3. Comparison of shear wave velocity in three different phantoms

Phantom concentration	Measurement by research purpose US machine	Proposed method	Error
6.00%	3.44 ± 0.09 m/s	3.54 ± 0.41 m/s	0.1 m/s
8.00%	5.91 ± 0.64 m/s	5.71 ± 0.15 m/s	-0.2 m/s
10.00%	7.25 ± 0.74 m/s	7.19 ± 0.37 m/s	-0.06 m/s

4.5.5 Shear wave velocity mapping of a non-homogeneous phantom

This experiment is carried out to show that the mechanically induced shear wave elastography can be used to image non-homogeneous phantom. In the experiment, an 8% PVA phantom is molded inside a softer 6% phantom. Figure 4.18 is an illustration of how the phantom is fabricated. An 8% PVA phantom is cut in a close to spherical shape with a diameter of 1.5 cm. By a small hook, the phantom ball is hooked inside a phantom mold. The 6% PVA liquid is poured into the mold, and then the 8% PVA phantom immersed in it. After saving in a freezer for about 1 day, the 6% PVA liquid has hardened, and the hook can be removed from the mold. The stiff 8% PVA phantom can be distinguished under B-mode sonography image as in figure Figure 4.18 (d).

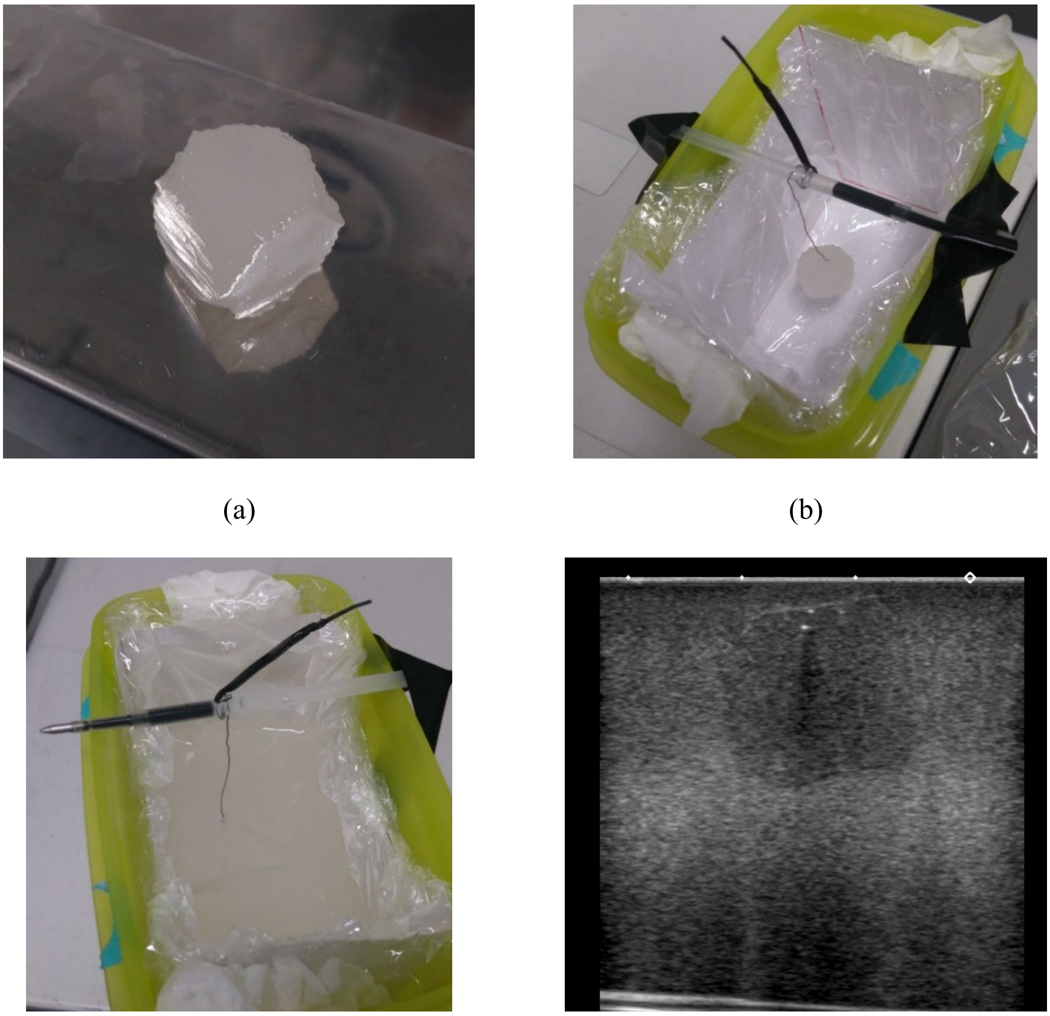

(a) (b)

(c) (d)

Figure 4.18 Fabrication of non-homogeneous PVA phantom

A similar setup of shear wave elastography is used in this experiment, except for the transducer with higher center frequency, PLU-1204BT 18L7 as shown in Figure 4.19. The non-homogeneous phantom was observed under a 12 MHz linear array transducer, and a vibration speaker with a vibration head was attached. In the experiment, 150 MHz sinusoid wave is transmitted via Bluetooth from a PC with a volume level of 30%.

The result of experiment is shown in Figure 4.20. A 10°steering angle was applied to the Color Doppler Imaging. The 8% PVA phantom appears on the upper left of the B-mode image in Figure 4.20 (a). When the shear wave was induced, the captured shadow shows a larger wavelength on the area with stiffer elasticity as shown by Figure 4.20 (b).

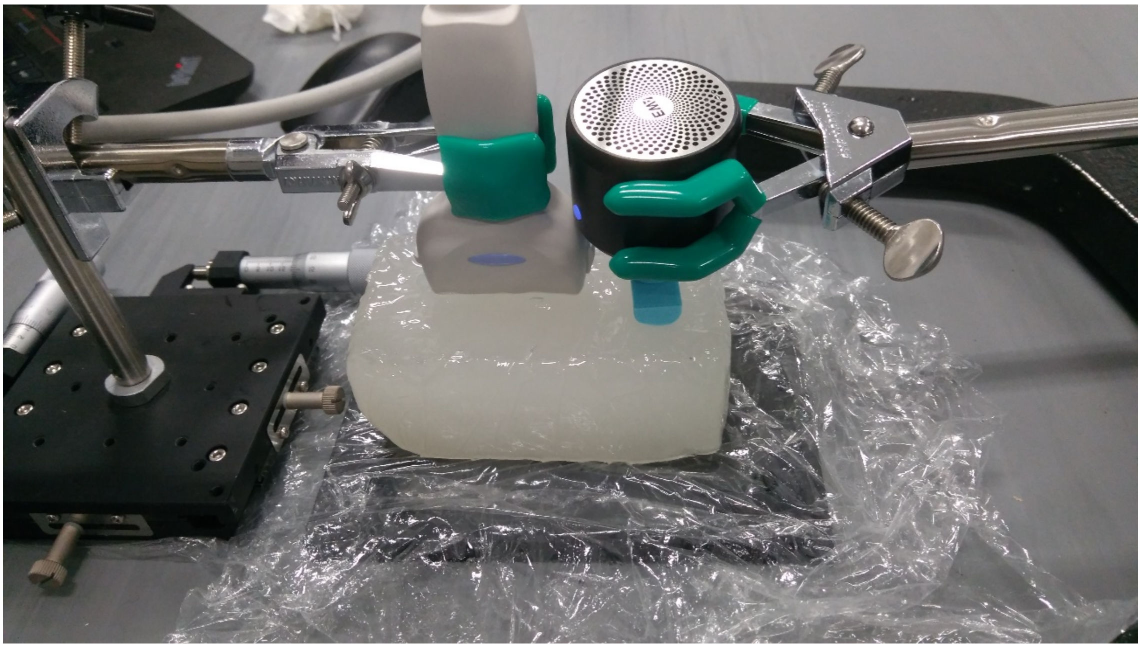

Figure 4.19 Experiment set-up for non-homogeneous phantom measurement

The phase map at fundamental frequency of this color Doppler shadow is shown in the Figure 4.20 (c). By calculating the slope of phase map, the shear wave velocity and direction are reconstructed as seen in the Figure 4.20 (d) and (e) respectively. In the Figure 4.20 (d), the area with higher concentration, which has higher stiffness can be correctly represented with the higher velocity of shear wave.

4.6 Discussion

I have demonstrated a method and experiment to resolve shear wave velocity map by a commercial ultrasound machine. In contrast to the binary pattern method [37], there is no need to satisfy shear wave frequency and amplitude conditions to obtain the maps.

Current day ultrasound machine has a sufficiently high PRF. However, a key parameter to observe the shear wave such as auto correlator packet size and the scanning speed as well as the detailed image processing algorithm of the built-in software remain confidential. Somehow, by adjusting the available setting of a commercial ultrasound machine, the shear wave shadow can be observed. My derivation to the pulsed Doppler formula explained the shadow formation and suggested that any number of PRF can be used to observe sinusoid vibration, except in some precise condition. Eventually the relation between the appearing image pattern and the real shear wave parameters is explained.

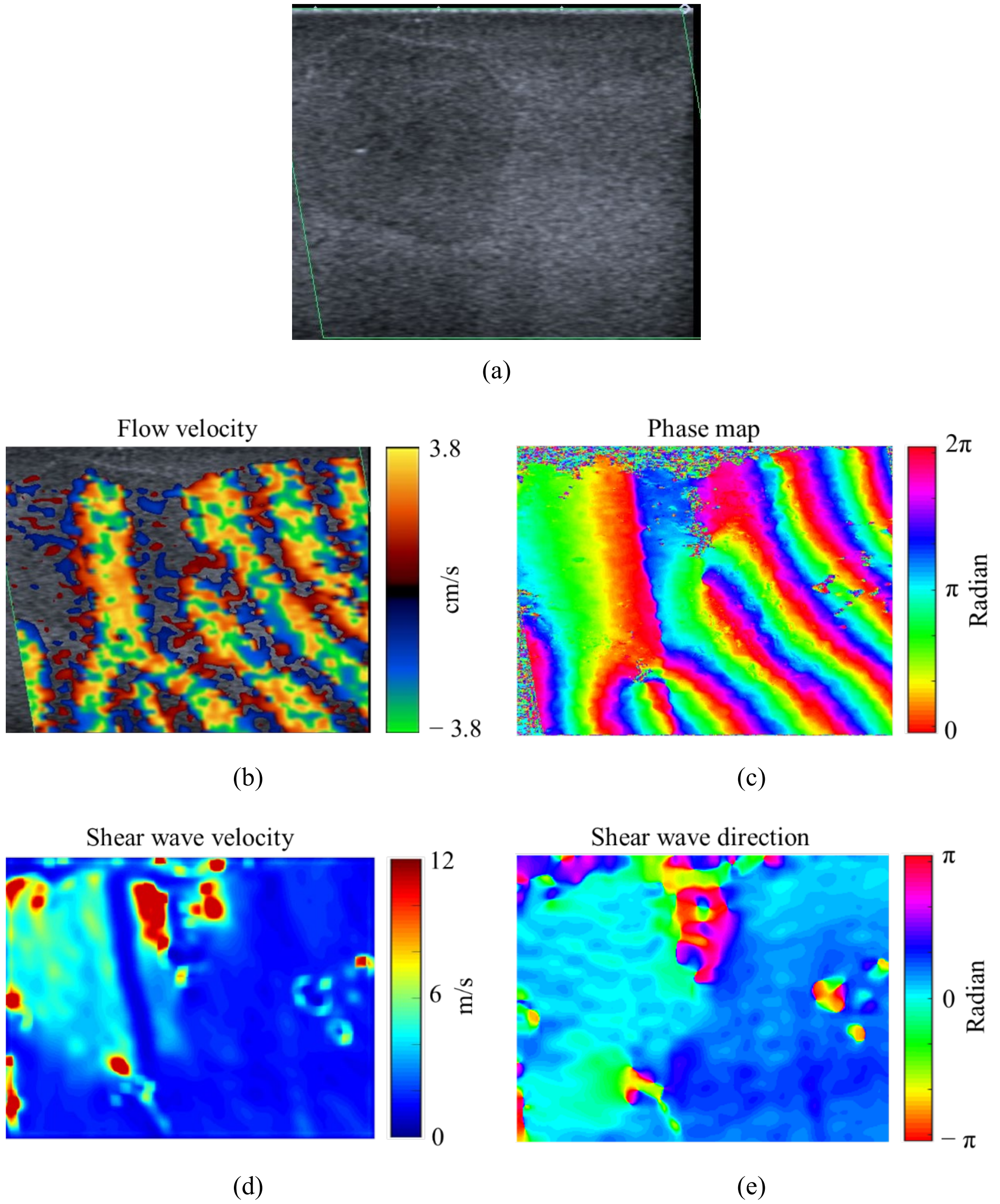

(a) (b) (c) (d) (e)

Figure 4.20 Shear wave map of non-homogeneous PVA phantom

The measurement result is a convincing evidence that the appearing color flow image in the commercial ultrasound machine is not the binary pattern since the probability of matching a precise condition by random choice is low and the small vibration amplitude is used. Nevertheless, the used PRF of Color Doppler Imaging (CDI) is much higher than the tested shear wave frequency. It is obvious that the measurement results by a commercial ultrasound machine do not appear as binary pattern as suggested by the previous method [37]. It is not a sinusoid surface as expected from original small displacement method as the measurement by a research purpose ultrasound machine either. In fact, it appears as a mixture of positive and negative velocity with a sinusoid envelope. This result can be understood since the frame rate the imaging system is not high enough to catch up the vibration frequency. However, the shadow of the shear wave is still captured by the CDI system. The built-in algorithm of the ultrasound machine might combine two subsequent frames to produce a better image to display. In this case, image registration algorithm may work to determine the correct position of two images which lead to ambiguity. It has been demonstrated that in a certain condition, the color flow image appears as a mixed two sinusoid with the same frequency. The frequency of this interference pattern is proportional to the shear wave wavenumber. However, the correct value of shear wave wavenumber is only known after the scanning delay is given. In this case, the logical scanning delay is obtained by calibration.

Basically, the method is developed from the small displacement method, so that, a small amplitude vibration source which is a universal vibration speaker is used. The novelty in this research is the resolving interference pattern captured by commercial ultrasound machine to obtain the real shear wave velocity, and thus, tissue elasticity.

On the other hand, when the binary pattern method employed with a given amplitude, the appeared pattern is four time denser than the shear wave original wavelength. It means that a lower vibration frequency will give the same number of wave pattern than with a direct Doppler elastography. In the experiment of binary pattern color Doppler elastography, the wavelength of the shear wave increases as the phantoms become harder following the PVA concentration increase. The larger the wavelength of the shear wave, the faster the propagation, which means, the higher the elastic modulus. Therefore, this result reflects the difference in the elastic modulus of the phantom. By looking at all measurement data, it is demonstrated that imaging the stiffness of the phantom is possible.

I have completed an investigation of general principles of shear wave velocity shadow forming in a Color Doppler Imaging (CDI) system. This finding has enabled a shear wave velocity to be measured by a commercial ultrasound machine. The experiment has shown that proposed method is capable to differentiate soft material with hard material. It has been tested to measure PVA phantoms with average error of 2.37%.

In the other experiment, I have shown the result of imaging non-homogeneous phantom by the color Doppler elastography method. It is demonstrated that the method is capable of distinguishing stiff area inside a softer phantom. This result might lead to the clinical implementation of clinical elastography to non-homogeneous tissue, such as distinguishing ligament with muscle.

4.6.1 Clinical Values

Color Doppler shear wave elastography is preferable for clinical application for the reason of its non-invasiveness. Since it uses an external vibrator to induce a shear wave, the estimation of elasticity could be considered more accurate and may penetrate deeper into the tissue. The result of experiments may lead to clinical application of this method as a diagnostic tool for tissue stiffness related diseases such as diffuse liver disease, breast cancer, thyroid nodules, renal fibrosis, prostate gland, lymph nodes and AC.

The Chronic Liver Disease (CLD) occurs everywhere around the world. The treatment recommendation relies on the accuracy of lived fibrosis/cirrhosis staging. Due to accumulative collagen deposition, the fibrosis progresses resulting in a stiffer liver. The US elastography method can be used to monitor this change of stiffness non-invasively. In a measurement of the stiffness, a standardized procedure is critical to guaranty the result accuracy and reliability. More specifically, when ARFI SWE techniques are used, the maximum measurement depth is limited to hinder it from the pulse refraction. With a 1D Transient Elastography (TE), it is found that liver stiffness values are correlated with histopathologic fibrosis stages in CLD patients. This result is compared with liver biopsy with a significant agreement. On the other hand, by a Point Shear Wave Elastography (pSWE) method, an assessment of liver fibrosis shows a good result. The assessment of fibrosis by 2D-SWE is considered more accurate than 1D-TE. However, a precise comparison is difficult due to different terminology, shear-wave frequency, reported parameters, or other technical factors for each technique, such as the using of elasticity units by m/s or kPa. The US elastography of the liver has a limitation in which the measurement may show ambiguity due to pathologic and normal physiologic processes. More specifically the surrounding capsule and the increasing volume of liver may affect elasticity measurement with increasing stiffness [43]. Overall, the US elastography has a limited capability in differentiating fibrosis stages. The future work in this area includes improving accuracy of differentiating fibrosis stages and standardizing techniques such as measurement units to enable results comparison across studies from different sites.

With an implementation of US elastography in the breast cancer, Tsukuba score (elasticity score) can be determined based on the stiffness map of the tissue in and around breast lesion [44].

The Tsukuba score has been a standard measure to differentiate benign from malignant breast lesions. Current applications of ultrasound elastography for clinical breast analysis call attention to the World Federation for Ultrasound in Medicine and Biology (WFUMB), where Shear Wave Imaging (SWI) is recommended only as a supplement of B-mode US when identifying abnormality. As a result, it is possible to downgrade lesions with soft elasticity which is obtained by strain imaging or Shear Wave Imaging (SWI). On the other hand, if Shear Wave Elastography or Shear Wave Imaging detect a malignancy, it is possible to upgrade lesion to a biopsy [45].

The US elastography is used in endocrinology to distinguish benign from malignant thyroid nodules. There is also an evidence that of follicular malignancy diagnosis can be helped by shear wave imaging [46]. Although the preliminary studies have shown various results, the promising future application could be gained by further validation and techniques standardization.

In the detection of chronic kidney disease (CKD), the ultrasound elastography is considered as a promising alternative to renal biopsy, due to its low cost and non-invasiveness. The reliability of US elastography is not good enough in the use for CKD stages differentiation or transplanted kidneys fibrosis grading. Many improvements in this field are still required in understanding the fibrosis progress and kidney elasticity relationship. Furthermore, the usage of US for focal renal mass characterization did not give a satisfactory result [47].

The use of US elastography in prostate cancer detection has a prospective as a complement or even replacement of biopsy. Studies on transrectal ultrasonography (TRUS) for cancer prostate detection shows good results, even though some prospective studies need to confirm the clinical values. Multimodal imaging has shown its superiority beyond the conventional single mode imaging [48]. However, future capability of USE in differentiating aggressive from non-aggressive prostate cancer should be investigated.

A preliminary result in a research has shown that US elastography can be used to identify the malignancy of superficial lymph nodes as well as in deep lymph nodes. In this method, the combination of B-mode US with elastography is used to increase the accuracy of diagnosis [49]. However, the existing studies on elastography of lymph nodes are restricted to small sample sizes, thus, research with larger sample sizes and avoided selection bias towards malignant lymph nodes should give clearer description on the disease [50].

In addition to the aforementioned diseases, the method of color doppler elastography has a potential for implementation for detection of AC which indicate a distinct elasticity on the ligament [11]. Also, it can be combined with other modality such as ligament velocity difference method to further improving the presentation of the disease [10].

Chapter 5
Conclusion

In this dissertation, I have presented two methods of quantitative tissue assessments as well as a clinical application in orthopedics for identifying Adhesive Capsulitis (AC) disease. The summarize of all findings of the research is described in this chapter.

5.1 Summary

A sonography method-based software to evaluate AC is implemented. The software is a speckle tracking algorithm implemented in MATLAB® 2019a code and the App Designer GUI. By measurement of a subject with a commercial ultrasound machine, shoulder ligament displacement and layers of tissue is visualized based on their velocity.

In addition, a novel measure of subscapularis adhesion is introduced as Adhesion Index (AdI), which can be calculated from the velocity difference between subscapularis and the deltoid muscle. It is shown that patient with restricted motion encounter a noticeable adhesion on the subscapularis, quantified by AdI. A relationship between AdI with the Range of Motion (ROM) and the AC is shown. The experiment results suggested that the origin of motion limitation could be explained by the AdI. Therefore, AdI could be a promising candidate as substitute or complement to the existing physical ROM examination, as it rules out the effect of pain in the motion limitation.

To the best of my knowledge, this implementation first quantitative method in orthopedics that uses speckle tracking to analyze the AC disease. The merit of using method includes non-invasiveness nature of the sonography, and that the data is obtainable by a common ultrasound machine. However, the subscapularis AdI value cannot distinguish secondary from idiopathic AC without introducing additional modality. This issue is tolerable since the AdI is not aimed to replace other modality to recognize the associated stiff and painful shoulder source such as MRI for Rotator Cuff Tears (RCT).

On the other part, a method of color Doppler elastography by mechanically induced shear wave with commercial US is described. The method is tested to resolve elasticity map of homogeneous and non-homogeneous phantom. The novelty of this method is, that it reconstructs elasticity without necessity for precise control of ensemble size to the ultrasound machine as well as shear wave frequency and amplitude condition. As an advantage, since it does not need a precise control, it can be implemented in a common commercially available ultrasound machine. The measurement results suggested that the method is capable to obtain the accurate estimation of the shear wave velocity, thus elasticity. However, it has a limitation in a still low imaging resolution.

5.2 Future Works

The method of measuring Subscapularis AdI as quantity that is linked to the AC disease has a limitation in that it cannot distinguish idiopathic and secondary AC. Therefore, it cannot be used alone in the specific diagnosis of AC without involving additional data. A future research that involves additional motions other than 1st ER as well as examining different region of interest should be considered, since shoulder adhesion may occur in different part of the shoulder.

On the other hand, the imaging resolution of mechanically induced color Doppler elastography is relatively low. In our experiment, the method is still capable differentiate the elasticity of 1.5 cm harder phantom, inside a softer phantom. The result of measuring smaller object, as well as application to the human shoulder still needs an investigation, more specifically, the effect of using different type of vibrating source to induce the shear wave in a shoulder. Eventually, mechanically induced shear wave elastography could be tested for use in combination of the speckle tracking method to give more clear description of the stiff and painful shoulder disease.

Cited References

[1] P. R. Hoskins, "Peak velocity estimation in arterial stenosis models using colour vector Doppler," *Ultrasound in Medicine & Biology,* vol. 23, no. 6, pp. 889-97, 1997.

[2] G. E. Trahey, J. W. Allison and O. T. v. Ramm, "Angle independent ultrasonic detection of blood flow," *IEEE Trans Biomed Eng,* vol. 34, no. 12, pp. 965-7, 1987.

[3] J. A. Jensen, "A new estimator for vector velocity estimation," *IEEE Trans Ultrason Ferroelectr Freq Control,* vol. 48, no. 4, pp. 886-94, 2001.

[4] K. Walker-Bone, K. P. Palmer, I. Reading, D. Coggon and C. Cooper, "Prevalence and Impact of Musculoskeletal Disorders of the Upper Limb in the General Population," *Arthritis & Rheumatism,* vol. 51, no. 4, pp. 642-651, 2004.

[5] K. Mezian and K.-V. Chang, "Shoulder, Frozen," National Taiwan University Hospital, 2018.

[6] R. Dias, S. Cutts and S. Massoud, "Frozen shoulder," *BMJ,* vol. 331, pp. 1453-1456, 2005.

[7] A. Tandon, S. Dewan, S. Bhatt, A. K. Jain and R. Kumari, "Sonography in diagnosis of adhesive capsulitis of the shoulder: a case–control study," *Ultrasound,* vol. 20, p. 227–236, 2017.

[8] A. Ando, Y. Hagiwara, Y. Onoda, K. Hatori, H. Suda, E. Chimoto and E. Itoi, "Distribution of Type A and B Synoviocytes in the Adhesive and Shortened Synovial Membrane during Immobilization of the Knee Joint in Rats," *The Tohoku Journal of Experimental Medicine,* vol. 221, no. 2, pp. 161-8, 2010.

[9] W. H. Akeson, D. Amiel, M. F. Abel, S. R. Garfin and S. L.-Y. Woo, "Effects of Immobilization on Joints," *Clinical Orthopaedics and Related Research,* vol. 219, pp. 28-37, 1987.

[10] N. Hermawan, M. Fujiwara, Y. Hagiwara and Y. Saijo, "Visualization of Shoulder Ligaments Motion by Ultrasound Speckle Tracking Method," in *42nd Annual International Conference of the IEEE Engineering in Medicine & Biology Society (EMBC)*, Virtual, 2020.

[11] C.-H. Wu, W.-S. Chen and T.-G. Wang, "Elasticity of the Coracohumeral Ligament in Patients with Adesive Capsulitis of the Shoulder," *Radiology,* vol. 278, no. 2, pp. 458-464, 2016.

[12] B. K. Horn and B. G. Schunck, "Determining Optical Flow," *Artificial Intelligence,* vol. 17, pp. 185-203, 1981.

[13] B. D. Lucas and T. Kanade, "An Image Registration Technique with an Application to Stereo Vision," in *7th Intl Joint Conf on Artificial Intelligence (IJCAI)*, Vancouver, 1981.

[14] J. D'hooge, "Principles and Different Techniques for Speckle Tracking," in *Myocardial Imaging: Tissue Doppler and Speckle Tracking*, Malden, Oxford, Carlton, Blackwell Publishing, 2007, pp. 17-25.

[15] T. Koga, K. Linuma, A. Hirano, Y. Iijima, T. Ishiguro-OOnuma, Y. Lijima, M. Hirano and T. Ishiquro, "Motion-compensated interframe coding for video conferencing," in *Proc. Nat. Telecommun. Conf.*, 1981, 1981.

[16] L.-K. Liu and E. Feig, "A Block-Based Gradient Descent Search Algorithm for Block Motion Estimation in Video Coding," *IEEE Transaction on Circuits and Systems for Video Technology,* vol. 6, no. 4, pp. 419-22, 1996.

[17] S. Zhu and K.-K. Ma, "A New Diamond Search Algorithm for Fast Block-Matching Motion Estimation," *IEEE Transaction on Image Processing,* vol. 9, no. 2, pp. 287-90, 2000.

[18] J. A. Nelder and R. Mead, "A Simplex Method for Function Minimization," *The Computer Journal,* vol. 7, no. 4, pp. 308-313, 1965.

[19] H.-C. Fei, C.-J. Chen and S.-H. Lai, "Enhanced Downhill Simplex Search for Fast Video Motion Estimation," in *Advances in Multimedia Information Processing – PCM 2005. Lecture Notes in Computer Science, vol 3767.*, Berlin, Heidelberg, Springer, 2005, pp. 512-523.

[20] K. N. Ryu, S. W. Lee, Y. G. Rhee and J. H. Lim, "Adhesive Capsulitis of the Shoulde Joint: Usefulness of Dynamic Sonography," *J Ultrasound Med,* vol. 12, pp. 445-9, 1993.

[21] A. S. Neviaser and R. J. Neviaser, "Adhesive Capsulitis of the Shoulder," *Journal of the American Academy of Orthopaedic Surgeons,* vol. 19, pp. 536-542, 2011.

[22] D. S. Moore, G. P. McCabe and B. A. Craig, Introduction to the Practice of Statistics, New York: W. H. Freeman and Company., 2009.

[23] D. Giavarina, "Understanding Bland Altman analysis," *Biochemia Medica,* vol. 25, no. 2, p. 141–51, 2015.

[24] A. Yamamoto, K. Takagishi, T. Osawa, T. Yanagawa, D. Nakajima, H. Shitara and T. Kobayashi, "Prevalence and risk factors of a rotator cuff tear in the general population," *Journal of Shoulder and Elbow Surgery,* vol. 19, pp. 116-20, 2010.

[25] R. M. Lerner, K. J. Parker, J. Holen, R. Gramiak and R. C. Waag, "Sono-Elasticity: Medical Elasticity Images Derived from Ultrasound," in *Acoustical Imaging*, Boston, Springer, Boston, MA, 1988, pp. 317-327.

[26] Y. Yamakoshi, J. Sato and T. Sato, "Ultrasonic imaging of internal vibration of soft tissue under forced vibration," *IEEE Transactions on Ultrasonics, Ferroelectrics, and Frequency Control,* vol. 32, no. 2, pp. 45-53, 1990.

[27] Y. Zheng, A. Yao, K. Chen, E. Zheng, T. Wang and S. Chen, "Impacts of the Capsule on Estimation of Shear Viscoelasticity of Livers," in *IEEE International Ultrasonics Symposium Proceedings*, 2011.

[28] H. L. Oestreicher, "Field and impendence of an oscillating sphere in a viscoelastic medium with an application to biophysics," *Journal of Acoustical Society of America,* vol. 23, pp. 707-14, 1951.

[29] D. C. Giancoli, Physics Principles with Applications 6th Ed., Upper Saddle River: Pearson Education, Inc., 2005.

[30] A. Anderson, "Doppler reflections," *Physics Education,* vol. 24, pp. 154-6, 1989.

[31] K. K. Shung, Diagnostic Ultrasound Imaging and Blood Flow Measurements, Boca Raton: CRC Press, 2006.

[32] J. A. Jensen, Estimation of Blood Velocities Using Ultrasound, A Signal Processing Approach, New York: Cambridge University Press, 1996.

[33] P. M. Embree and W. D. O'Brien, "The accurate ultrasonic measurement of the volume flow of blood by time domain correlation," in *Ultrasonics Symposium Proceedings*, 1985.

[34] P. M. Embree and W. D. O'Brien, "Volumetric blood flow via time-domain correlation: experimental verification," *IEEE Transactions on Ultrasonics, Ferroelectrics, and Frequency Control,* vol. 37, no. 3, pp. 176-89, 1990.

[35] O. Bonnefous and P. Pesqué, "Time Domain Formulation of Pulse-Doppler Ultrasound and Blood Velocity Estimation by Cross Correlation," *Ultrasonic Imaging,* vol. 8, no. 2, pp. 73-85, 1986.

[36] C. Kasai, K. Namekawa, A. Koyano and R. Omoto, "Real-Time Two-Dimensional Blood Flow Imaging Using an Autocorrelation Technique," *IEEE Transactions on Sonics and Ultrasonics,* Vols. su-32, no. 3, pp. 458-464, 1985.

[37] Y. Yamakoshi, T. Kasahara, T. Iijima and Y. Yuminaka, "Shear Wave Wavefront Mapping Using Ultrasound Color Flow Imaging," *Ultrasonic Imaging,* vol. 37, no. 4, pp. 323-340, 2015.

[38] Z. Wu, L. S. Taylor, D. J. Rubens and K. J. Parker, "Sonoelastographic imaging of interference patterns for estimation of the shear velocity of homogeneous biomaterials," *Physics in Medicine & Biology,* vol. 49, no. 6, pp. 911-922, 2004.

[39] K. Hoyt, K. J. Parker and D. J. Rubens, "Real-time Shear Velocity Imaging Using Sonoelastographic Techniques," *Ultrasound in Medicine & Biology,* vol. 33, no. 7, pp. 1086-1097, 2007.

[40] M. S. T. G. Nightingale K, "Shear-wave generation using acoustic radiation force: in vivo," *Ultrasound Med Biol.,* vol. 29, pp. 1715-23, 2003.

[41] S.-R. Huang, R. M. Lerner and K. J. Parker, "Time domain Doppler estimators of the amplitude of vibrating targets," *The Journal of the Acoustical Society of America,* vol. 91, no. 2, pp. 965-974, 1992.

[42] N. Hermawan, A. Sato, M. Fujiwara, T. Ishii, Y. Hagiwara, Y. Yamakoshi and Y. Saijo, "Binary Pattern Color Doppler Shear Wave Elastography (Accepted)," in *43rd Annual International Conference of the IEEE Engineering in Medicine and Biology Society*, Virtual, 2021.

[43] H. Morikawa, K. Fukuda, S. Kobayashi, H. Fujii, S. Iwai, M. Enomoto, A. Tamori, H. Sakaguchi and N. Kawada, "Real-time tissue elastography as a tool for the noninvasive assessment of liver stiffness in patients with chronic hepatitis C," *Journal of gastroenterology,* vol. 46, pp. 350-8, 2011.

[44] A. Itoh, E. Ueno, E. Tohno, H. Kamma, H. Takahashi, T. Shiina, M. Yamakawa and T. Matsumura, "Breast disease: clinical application of US elastography for diagnosis," *Radiology,* vol. 239, pp. 241-50, 2006.

[45] R. G. Barr and e. al., "WFUMB guidelines and recommendations for clinical use of ultrasound elastography: Part 2: breast," *Ultrasound in medicine & biology,* vol. 41, pp. 1148-60, 2015.

[46] A. E. Samir, M. Dhyani, A. Anvari, J. Prescott, E. F. Halpern, W. C. Faquin and A. Stephen, "Shear-Wave Elastography for the Preoperative Risk Stratification of Follicular-patterned Lesions of the Thyroid: Diagnostic Accuracy and Optimal Measurement Plane," *Radiology,* vol. 277, pp. 565-73, 2015.

[47] R. M. S. Sigrist, J. Liau, A. E. Kaffas, M. C. Chammas and J. K. Willmann, "Ultrasound Elastography: Review of Techniques and Clinical Applications," *Theranostics,* vol. 7, no. 5, pp. 1303-29, 2017.

[48] J.-M. Correas, A.-M. Tissier, A. Khairoune, G. Khoury, D. Eiss and O. Hélénon, "Ultrasound elastography of the prostate: state of the art," *Diagn Interv Imaging,* vol. 94, no. 5, pp. 551-60, 2013.

[49] S. Paterson, F. Duthie and A. J. Stanley, "Endoscopic ultrasound-guided elastography in the nodal staging of oesophageal cancer," *World J Gastroenterol,* vol. 18, no. 9, pp. 889-95, 2012.

[50] K. S. Bhatia, Y. Y. Lee, E. H. Yuen and A. T. Ahuja, "Ultrasound elastography in the head and neck. Part II. Accuracy for malignancy," *Cancer Imaging,* vol. 13, no. 2, pp. 260-76, 2013.

Acknowledgements

Praise be to Allah, Lord of the universe. Prayers and greetings to the prophet Muhammad SAW.

I would like to express my sincere thanks to Prof. Yoshifumi Saijo for all his advice and supervision as well as uncountable support for the completion of my study. I have learned a lot of knowledges and passed 3 years in the laboratory with a wonderful experience. My deep appreciation is for dissertation judges, Prof. Ryoichi Nagatomi and Assoc. Prof. Shin Yoshizawa.

This dissertation is written with a great help from Mizuki Fujiwara who has provided me very valuable data from patient measurement and overwhelming explanation of clinical aspects.

My deep gratitude is also to the Institut Teknologi Sepuluh Nopember (ITS) for assigning me to this doctoral study and Tohoku University Data Science Program (DSP) II for providing an opportunity to join the program. I would repeat my great thanks to Prof. Takuro Ishii for every awesome discussion and useful suggestions for my research; Prof. Yoshihiro Hagiwara for teaching clinical application of ultrasonography; Aoi Sato for helping me with shear wave measurement; and Morino Taisuke who has helped a lot with administrative needs during my early days in Sendai. I also thank Akira Sato, Ryo Shintate, Syahril Siregar, Sri Oktamuliani, Rebecca Anna Plant, Anam Bhatti, Naoya Kanno, Hayoto Ikeda, Jo Oyama and all member of Saijo laboratory for the wonderful cooperation; the graduate academic affairs, Ms. Haruko Watanabe; and the GSIS International Liaison Office staff, Ms. Ikumi Koyama.

My special thank is dedicated to Pak Achmad Arifin for his priceless trust and motivation as well as Prof. Mohammad Nuh and Pak Tri Arief Sardjono for the recommendation to the study. I deeply appreciate all the administrative staffs of ITS Surabaya and all my colleagues in Biomedical Engineering Department of ITS.

I must convey countless thanks to my beloved wife Oktaviany Irma Wiputri for her great support during this study and the rest of my life. Our journey was full of joy and unexpected surprises, but only with her I can go this far. Of course, I am so grateful for every delicious food and the birthday cake she has cooked for me. I am blessed with the birth of my children Amzar Wikan Baiquni and Sinan Hideo Ranugati to color my life. They are really nice children, my future and the successor of my dream pursuit.

My deep thanks to Mbak Etik, Ima and Ifa, Mbak Ade, Alif, Mbak Miftah, Adam and Mila, Akung Papa Wiyanto, Uti Mama Kurniawati, Pakpoh Iwan as well as all my family and relatives.

With all my respect, thanks to all member of Keluarga Muslim Indonesia di Sendai (KMIS) and the small recitation group, all member of Persatuan Pelajar Indonesia di Sendai (PPIS), teachers, colleagues, friends and whoever has contributed to the completion to this dissertation that is too many to mention all.

One day when I was child, my mother Sri Ruchanah came during break time at kindergarten to hand a glass of milk which I forgot to drink that morning. Back then, just a milk was so precious, but I remember she always put her best for me and my future no matter in any situation. At that time, I was so obsessed with electronic stuffs and tinkering. Not only my late brother Mas Hari has introduced me to the first circuit with a battery, cable, and lamp; he also helped me with study and almost every other thing. When I was at the beginning of 6th grade of elementary school, my brother Mas Arif bought me a replacement for the burned Silicon Controlled Rectifier (SCR) for my running light circuit. He said that the knowledge is expensive yet the cost for every of it is nothing compared to the experience that I will get. When I was at junior high school, my brother Mas Ihwan enrolled me to the 'Persahabatan' English course with his visionary thought. I just realized the wonderful advantage of studying English when I took a double degree master program in Germany, after 13 years later. His study in mechanical engineering was an inspiration to my passion in engineering too.

I remember a message about how valuable a knowledge is. Now, I almost complete 22 years of formal study, and every morning I still say the same prayer *"Robbi Zidni Ilma Warzuqni Fahma, Aamiin"*.

This dissertation is dedicated to my late father

Djabir Sjamsudiwijoto

for all his love and devotion

Research Achievements

Research Achievements Related to Dissertation

[1]. Norma Hermawan, Aoi Sato, Mizuki Fujiwara, Takuro Ishii, Yoshihiro Hagiwara, Yoshiki Yamakoshi and Yoshifumi Saijo, "Binary Pattern Color Doppler Shear Wave Elastography", 2021 43rd Annual International Conference of the IEEE Engineering in Medicine and Biology Society (EMBC 2021), *[Accepted]*.

[2]. Norma Hermawan, Takuro Ishii, Yoshiki Yamakoshi and Yoshifumi Saijo, "Large Amplitude Harmonic Vibration under Pulse Doppler Measurement", International Conference on Biomedical Engineering (ICoBE 2021), *[Accepted]*.

[3]. Norma Hermawan, Mizuki Fujiwara, Yoshihiro Hagiwara, Yoshifumi Saijo, "Visualization of Shoulder Ligaments Motion by Ultrasound Speckle Tracking Method", 2020 42nd Annual International Conference of the IEEE Engineering in Medicine & Biology Society (EMBC 2020), pp. 2084-2087, July 2020.

Other Research Achievements

[1]. Norma Hermawan, Achmad Arifin, Fauzan Arrofiqi, Mohammad Nuh, Yoshifumi Saijo, "Wireless ECG Electrode to Improve Tele-cardiac Monitoring Usability", 11th Asian-Pacific Conference on Medical and Biological Engineering (APCMBE 2020), IFMBE Proceedings 82, pp. 332-339, 2021.

[2]. Ryo Hirano, Makoto Kanzaki, Mototaka Arakawa, Norma Hermawan, Kazuto Kobayashi, Yoshifumi Saijo, "Biomechanics of C2C12 Cells Observed with Cellular Resolution Scanning Acoustic Microscope Combined with Optical Microscope", 2019 41st Annual International Conference of the IEEE Engineering in Medicine and Biology Society (EMBC), pp. 4828-4831, July 2019.

[3]. Norma Hermawan, Achmad Arifin, Muhammad Farid Retistianto, “Sistem Pelaporan Telecardiac Monitoring Melalui Layanan Pesan Singkat (SMS)”, Jurnal Nasional Teknik Elektro (JNTE), Vol. 7, No. 3, pp. 183-190, November 2018.

Appendix A

Ligament Velocity Analyzer User Guide

Veloc Interface v10.7

User Guide

1. Interface

➢ Home

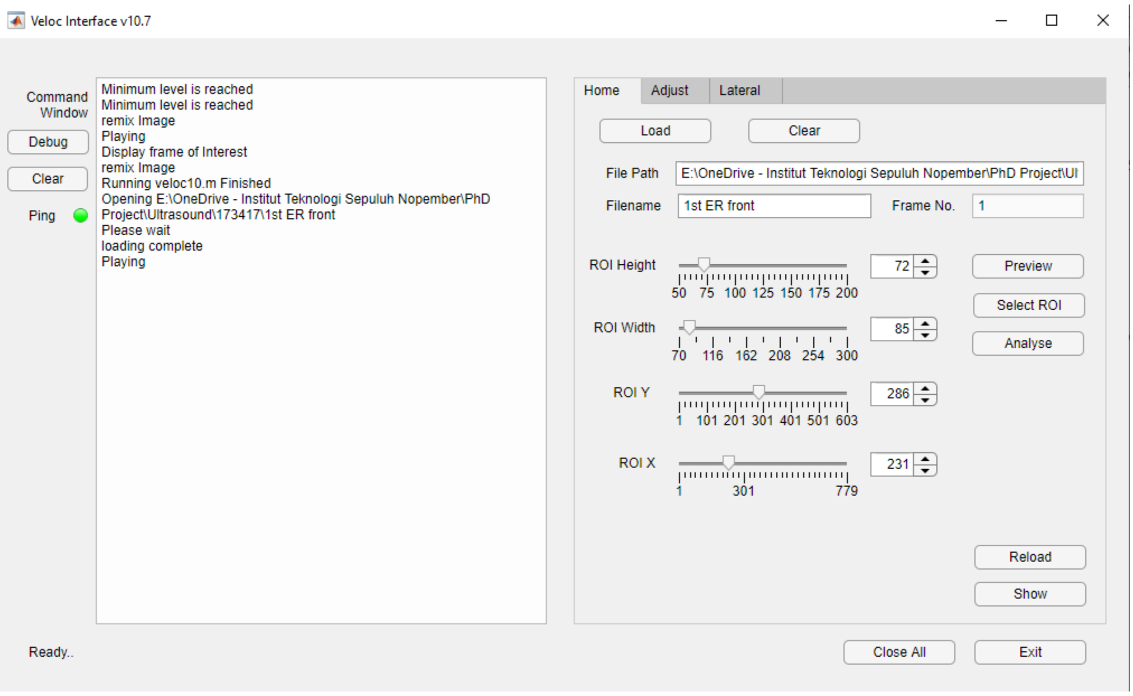

```
Minimum level is reached
Minimum level is reached
remix Image
Playing
Display frame of Interest
remix Image
Running veloc10.m Finished
Opening E:\OneDrive - Institut Teknologi Sepuluh Nopember\PhD
Project\Ultrasound\173417\1st ER front
Please wait
loading complete
Playing
```

File Path: E:\OneDrive - Institut Teknologi Sepuluh Nopember\PhD Project\UI

Filename: 1st ER front

Frame No.: 1

ROI Height: 72

ROI Width: 85

ROI Y: 286

ROI X: 231

Ready..

➢ Adjust

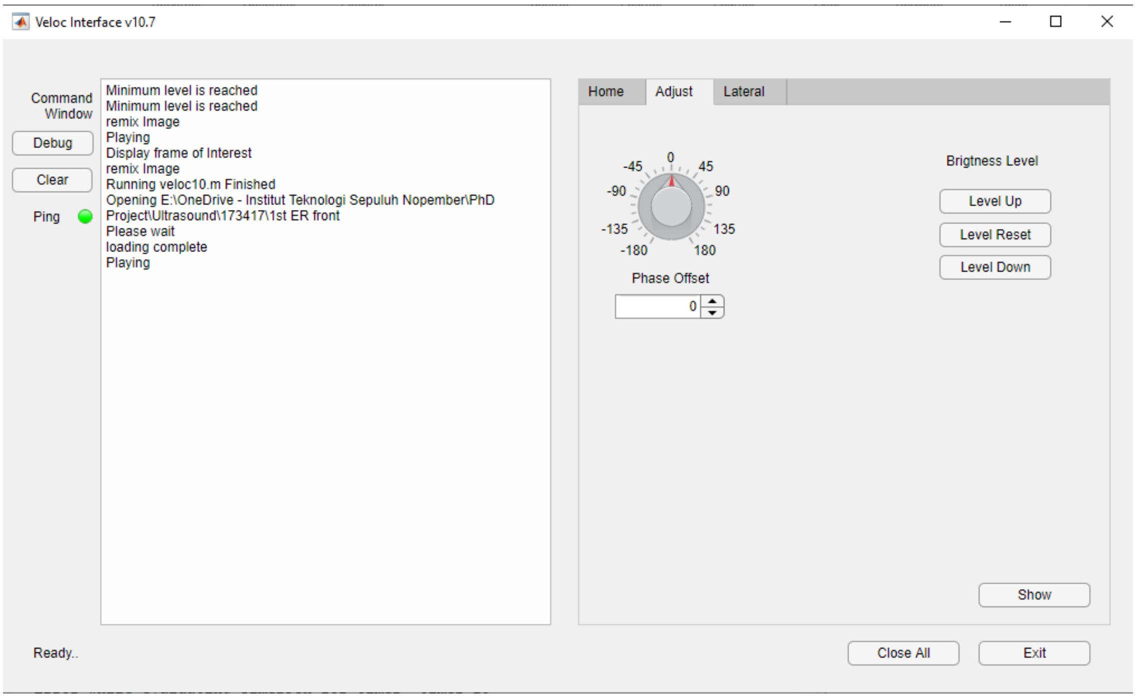

```
Minimum level is reached
Minimum level is reached
remix Image
Playing
Display frame of Interest
remix Image
Running veloc10.m Finished
Opening E:\OneDrive - Institut Teknologi Sepuluh Nopember\PhD
Project\Ultrasound\173417\1st ER front
Please wait
loading complete
Playing
```

Phase Offset: 0

Ready..

➢ Lateral Cut

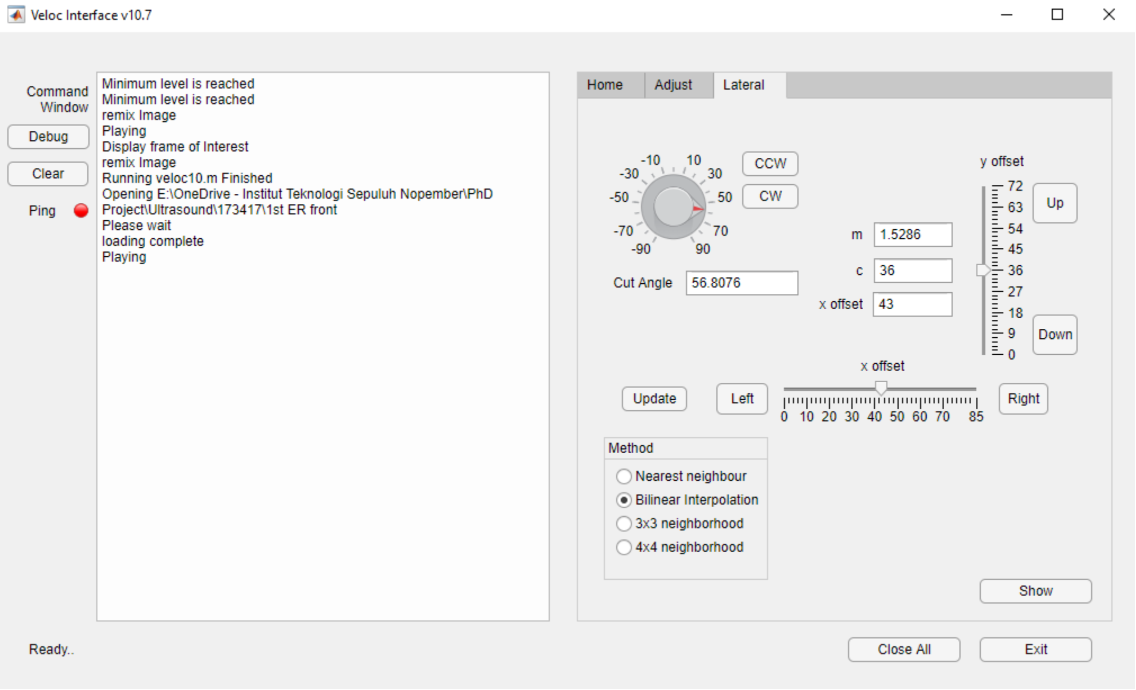

```
Minimum level is reached
Minimum level is reached
remix Image
Playing
Display frame of Interest
remix Image
Running veloc10.m Finished
Opening E:\OneDrive - Institut Teknologi Sepuluh Nopember\PhD
Project\Ultrasound\173417\1st ER front
Please wait
loading complete
Playing
```

Cut Angle: 56.8076

m: 1.5286

c: 36

x offset: 43

Method:
- ○ Nearest neighbour
- ● Bilinear Interpolation
- ○ 3x3 neighborhood
- ○ 4x4 neighborhood

2. New Features

- ➢ Velocity vectors reload
  - ✧ Click this button to reload previous velocity analysis result and variables without restarting new analysis from the beginning.
- ➢ Debug button
  - ✧ Click debug button to display all global variables used in veloc10.m (for development purpose only)
- ➢ 4 Cut methods
  - ✧ Choose any cut method to display different lateral view.
- ➢ Saved cut angle and offset last values
  - ✧ Cut angle and offset values are saved when exit button is clicked. The variables are reloaded on the next program start.
- ➢ Reliable status and ping indicator
  - ✧ Status label displays ‘busy’ when the program is busy, please wait for a while. The ping/connect indicator stop blinking when the program is busy or encounter an error.

Veloc Interface v10.4

User Guide

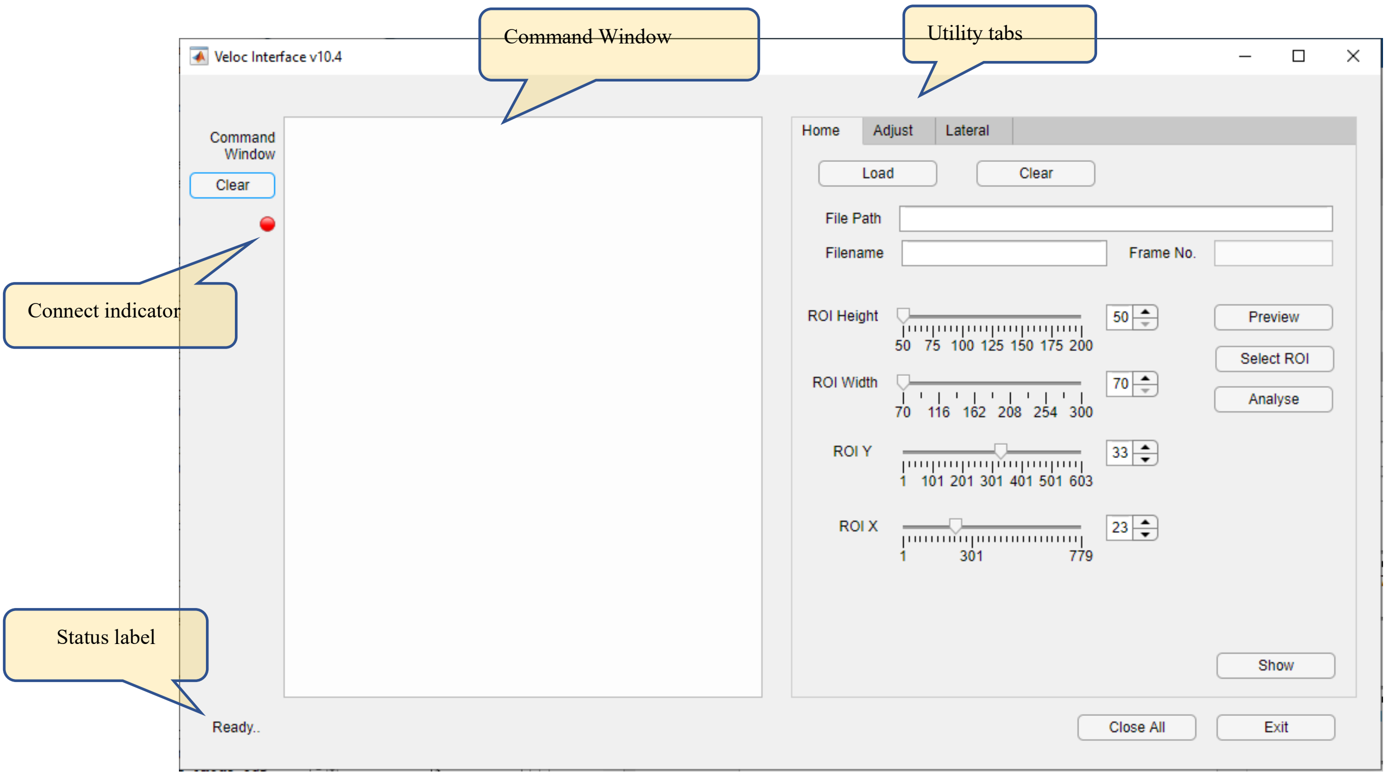

1. Open the Veloc Interface v10.4 with 'run' matlab script.
2. The Veloc Interface v10.4 GUI opened. The connect indicator blinks in 1 second period. Wait until the label on the lower left side change to 'Ready'.
3. The 'command window' displays the executed Matlab commands.
4. Click 'Load' button.

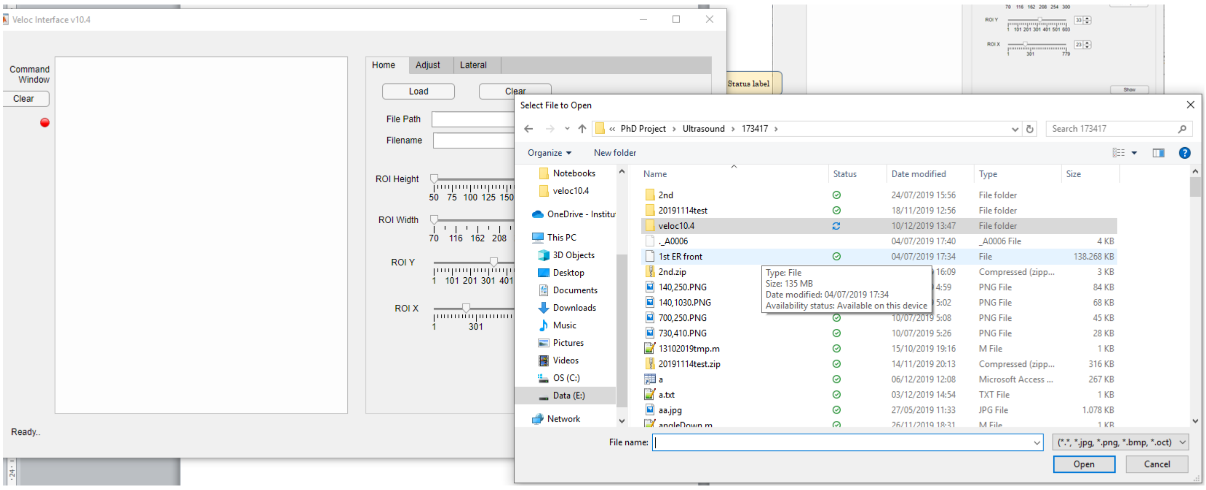

Name	Status	Date modified	Type	Size
2nd	✓	24/07/2019 15:56	File folder	
20191114test	✓	18/11/2019 12:56	File folder	
veloc10.4	↻	10/12/2019 13:47	File folder	
._A0006		04/07/2019 17:40	_A0006 File	4 KB
1st ER front	✓	04/07/2019 17:34	File	138.268 KB
2nd.zip		16:09	Compressed (zipp...	3 KB
140,250.PNG		4:59	PNG File	84 KB
140,1030.PNG		5:02	PNG File	68 KB
700,250.PNG	✓	10/07/2019 5:08	PNG File	45 KB
730,410.PNG	✓	10/07/2019 5:26	PNG File	28 KB
13102019tmp.m	✓	15/10/2019 19:16	M File	1 KB
20191114test.zip	✓	14/11/2019 20:13	Compressed (zipp...	316 KB
a	✓	06/12/2019 12:08	Microsoft Access ...	267 KB
a.txt	✓	03/12/2019 14:54	TXT File	1 KB
aa.jpg	✓	27/05/2019 11:33	JPG File	1.078 KB
angleDown.m	✓	26/11/2019 18:31	M File	1 KB

Type: File
Size: 135 MB
Date modified: 04/07/2019 17:34
Availability status: Available on this device

File name:
(*.*, *.jpg, *.png, *.bmp, *.oct)

5. Choose a DICOM formatted file. It could be a file without an extension.
6. Click ‘Preview’ button. Wait until a movie player displays.

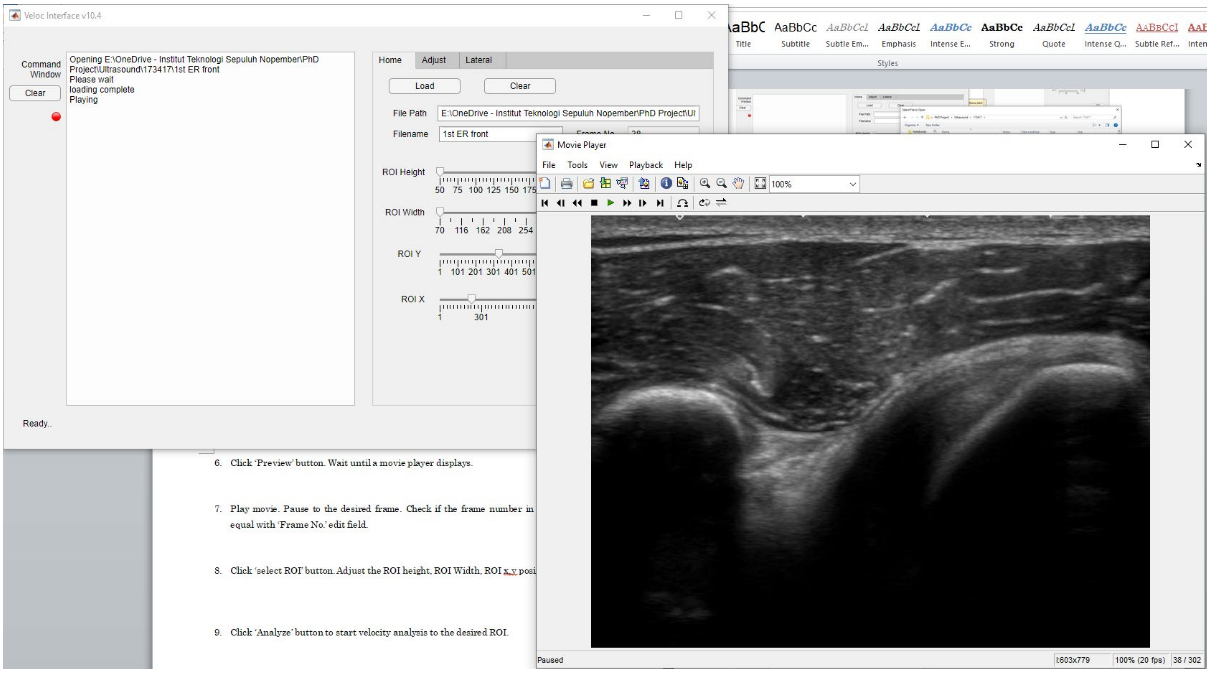

Opening E:\OneDrive - Institut Teknologi Sepuluh Nopember\PhD Project\Ultrasound\173417\1st ER front
Please wait
loading complete
Playing

File Path: E:\OneDrive - Institut Teknologi Sepuluh Nopember\PhD Project\UI

Filename: 1st ER front

Ready..

6. Click ‘Preview’ button. Wait until a movie player displays.

7. Play movie. Pause to the desired frame. Check if the frame number in equal with ‘Frame No.’ edit field.

8. Click ‘select ROI’ button. Adjust the ROI height, ROI Width, ROI x,y posi

9. Click ‘Analyze’ button to start velocity analysis to the desired ROI.

Paused

1603x779

100% (20 fps)

38 / 302

7. Play movie. Pause to the desired frame. Check if the frame number in movie player is equal with ‘Frame No.’ edit field.
8. Click ‘select ROI’ button. Wait until desired frame displays ROI in a green rectangle. Adjust the ROI height, ROI Width, ROI x,y position.

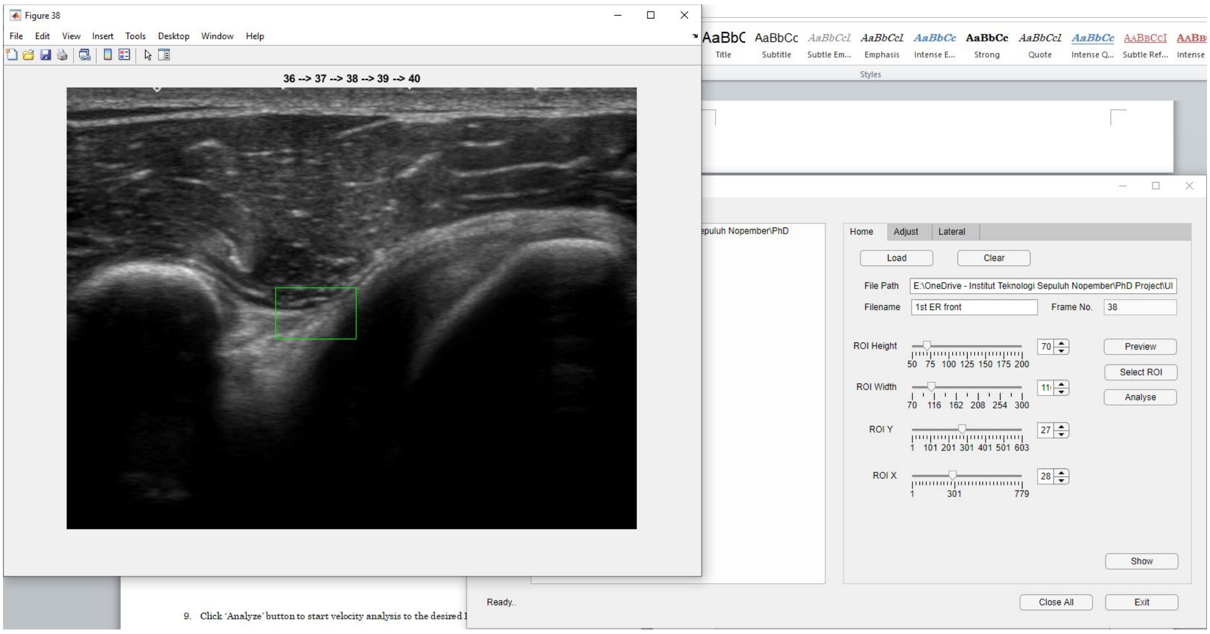

36 --> 37 --> 38 --> 39 --> 40

File Path: E:\OneDrive - Institut Teknologi Sepuluh Nopember\PhD Project\UI

Filename: 1st ER front

Frame No.: 38

ROI Height: 70

ROI Width: 11

ROI Y: 27

ROI X: 28

Ready..

9. Click ‘Analyze’ button to start velocity analysis to the desired I

9. Click ‘Analyze’ button to start velocity analysis to the desired ROI.
10. Wait for some moments until analysis result appear in the screen.

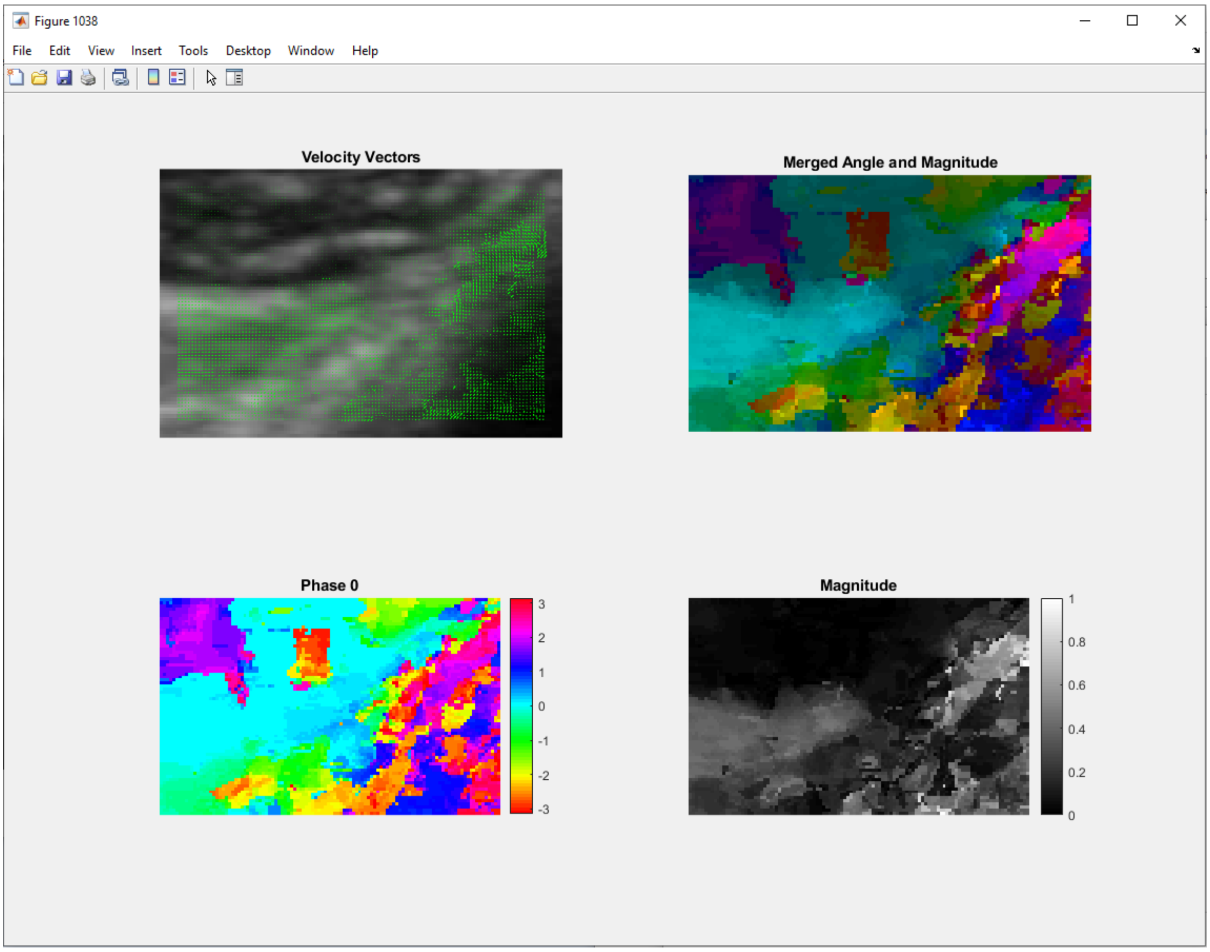

- Velocity vectors display on the top left in green arrows with a proportional length and angle representing velocity scale and direction of tissue in particular points.
- The magnitude and angle (phase) of the velocity vectors are plotted on the separated images on the bottom left and right.
- The phase image and the magnitude image are merged in a new image on the top right.

11. Move to ‘adjust’ tab.

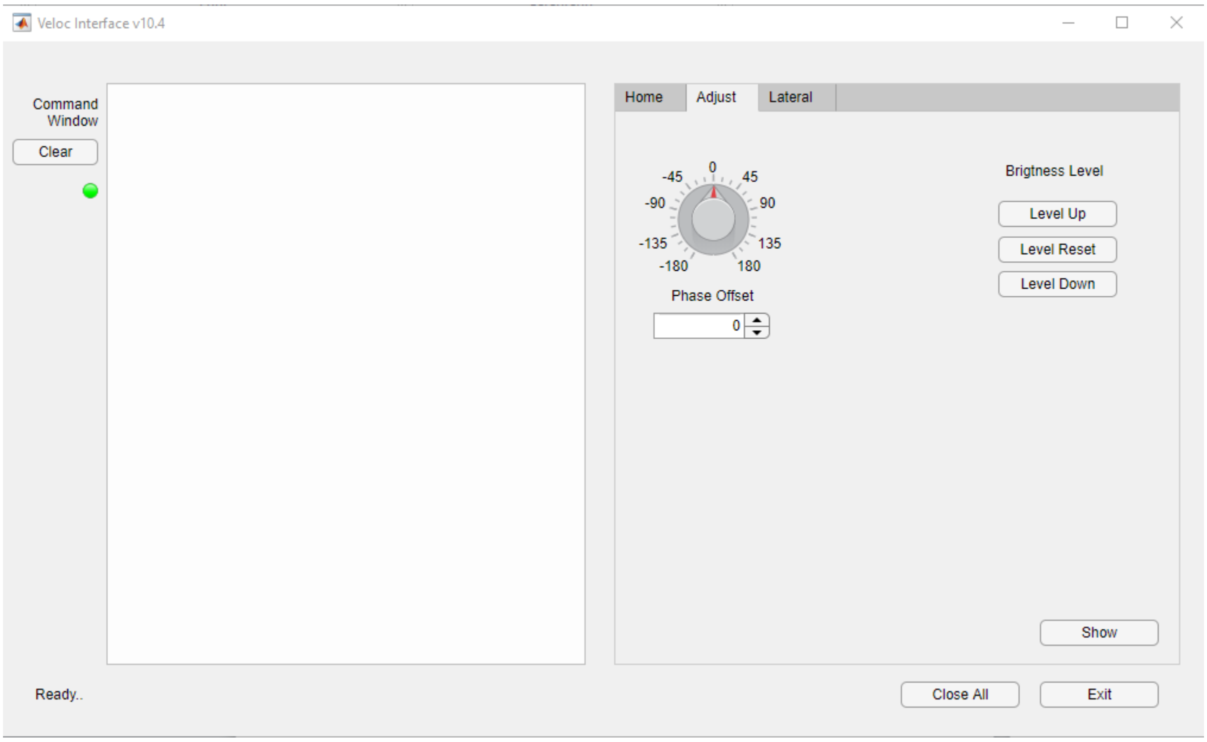

12. Adjust the brightness level and phase offset to obtain the best velocity map image.
13. Move to ‘Lateral’ tab.

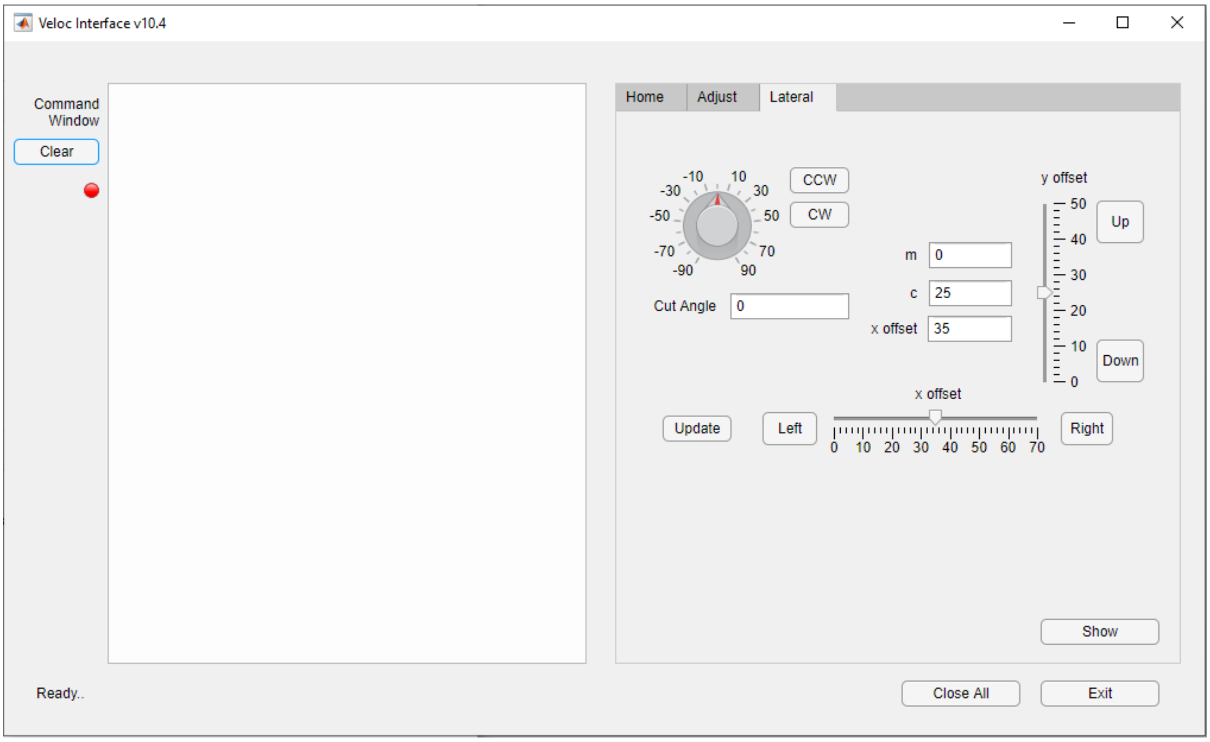

14. Click ‘Update’ button.

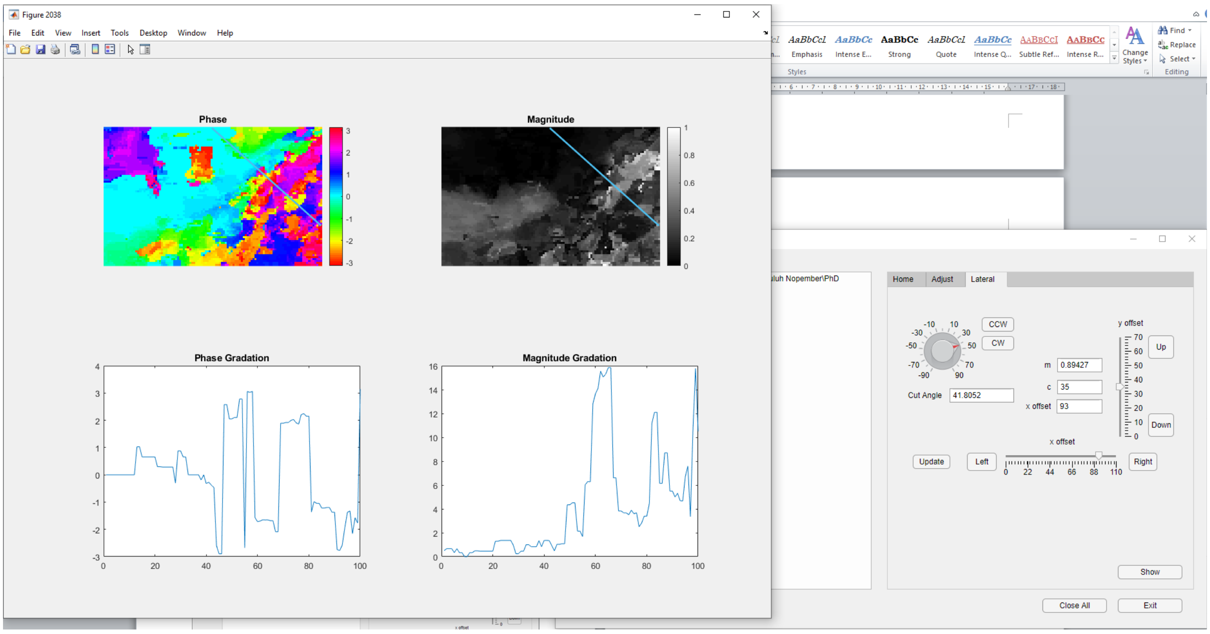

m 0.89427

c 35

x offset 93

Cut Angle 41.8052

15. Adjust angle and the position of the image cut. Phase gradation and the magnitude gradation of velocity vectors displayed on the screen.
16. Click ‘Close all’ button to close all images.
17. Click ‘Exit’ button to exit from the Veloc Interface v10.4 application.

Appendix B

Muscle Adhesion Analyzer User Guide

Strain Interface v1.5

User Guide

1. Interface

➢ Interface

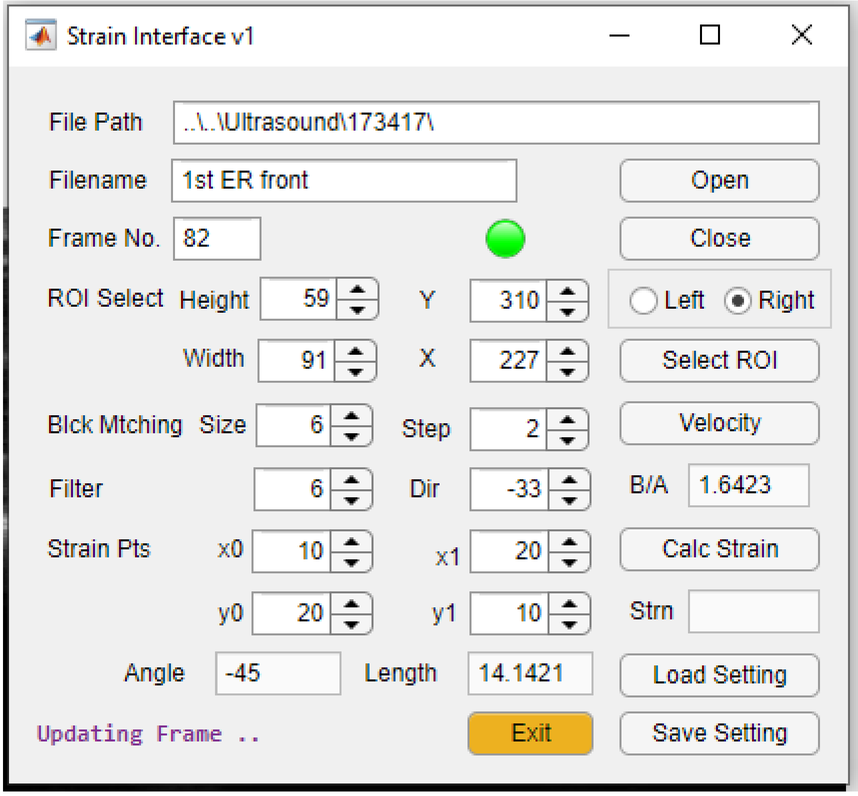

Strain Interface v1

File Path: ..\..\Ultrasound\173417\

Filename: 1st ER front

Frame No. 82

ROI Select Height 59 Y 310 ○ Left ● Right

Width 91 X 227

Blck Mtching Size 6 Step 2

Filter 6 Dir -33

B/A 1.6423

Strain Pts x0 10 x1 20

y0 20 y1 10

Strn

Angle -45 Length 14.1421

`Updating Frame ..`

➢ Main Window

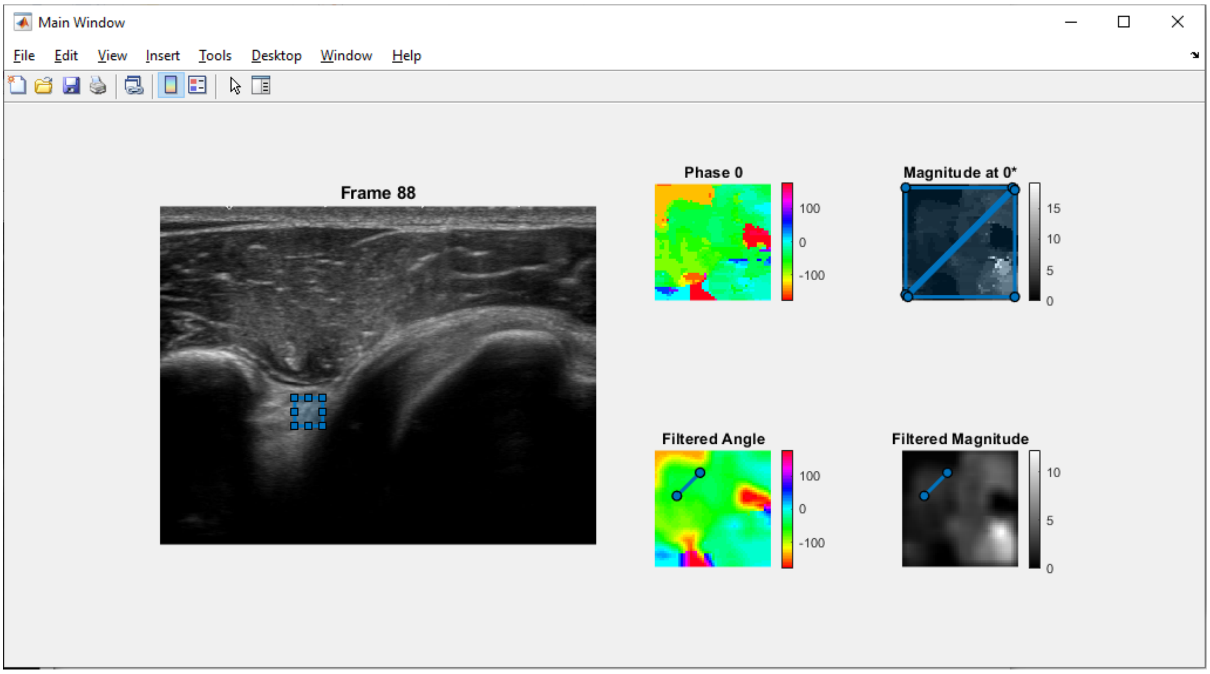

- **Movie Player**

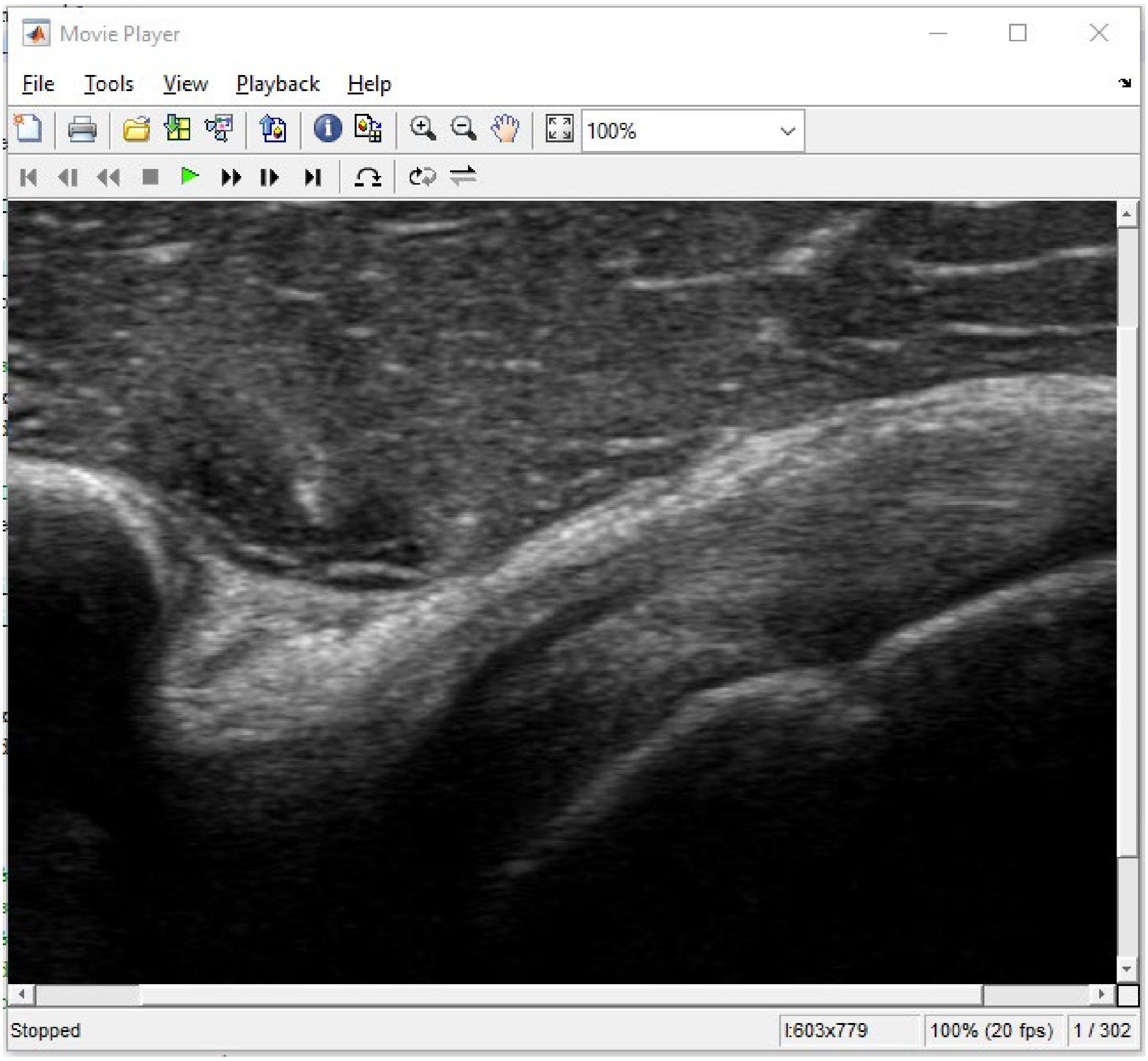

2. User Guide

18. Extract the *.zip file to a folder
19. Open Matlab, navigate to the extracted folder

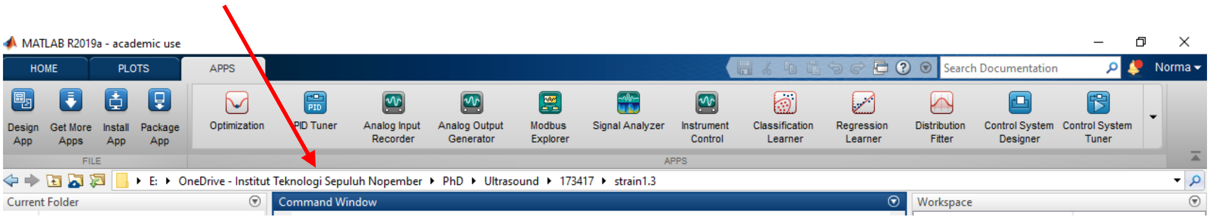

E: ▸ OneDrive - Institut Teknologi Sepuluh Nopember ▸ PhD ▸ Ultrasound ▸ 173417 ▸ strain1.3

20. Open the Strain Interface v1.5 by typing command

    ```
    strainIFC1
    ```

    The GUI window is displaying Strain Interface v1, but this is version 1.5.
21. Depending on the running PC, it might be necessary to rebuild the *.mex file by `‘mex fastCPlotVelocVect.c’` or `‘mex fastCPlotVelocVect.c -R2018a’`.
22. The Strain Interface v1 GUI and a main figure window are opened. Wait until the label on the lower left side change to ‘**Ready**’.
23. Click ‘Open’ button.
24. Choose a *.dicom file to analyze
25. Click ‘**Preview’** button. Wait until a movie player displays.
26. Play movie. Pause to the desired frame. Check if the frame number in movie player is equal with ‘**Frame No.**’ edit field on the GUI.
27. Select default ROI from radio box, either **left** or **right** position.
28. Click ‘**select ROI**’ button. Move and resize rectangular ROI to the desired position. Click ‘**select ROI**’ button again.
29. Move and resize two A and B triangles to compare in magnitude window. The default position is left or right diagonal, but it is changeable.

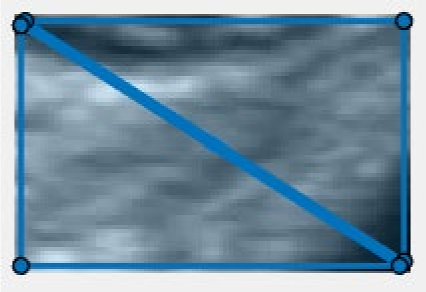

Left

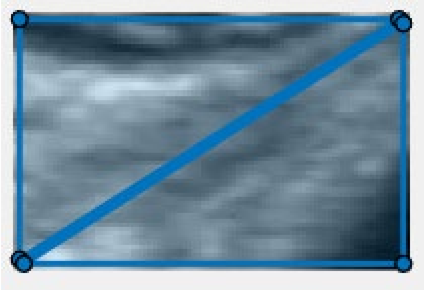

Right

30. Select direction angle of velocity. In our software, 0° is motion to the right, **90°** is **down** motion, **-90** is **up** motion and 180 is motion to the left, and so on.

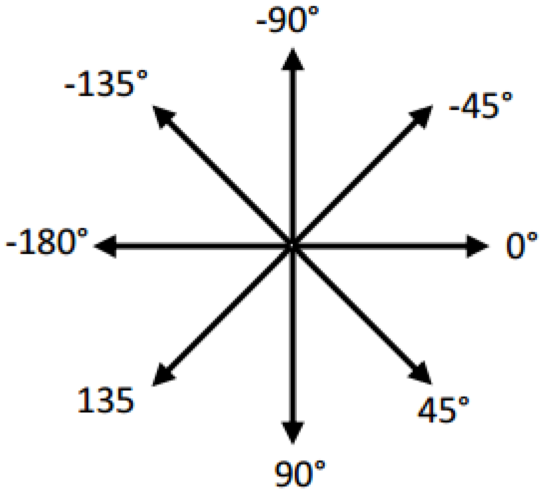

31. Adjust block size, frame step and filter size parameters
32. Click ‘**Velocity**’ button to start velocity analysis to the desired ROI.
33. Wait for some moments until analysis result will appear to the screen.
34. The B/A value appears on the interface window
35. Repeat step 14 until the desired result is obtained
36. Repeat to step 11 until the desired result is obtained
37. Move and resize the line on the **Filtered Angle** window with mouse, this line is the desired ROI for strain calculation. The line on **Filtered Magnitude** is moving, following line change on **Filtered Angle** window.
38. Click **Calc Strain** to get strain value on the ROI.
39. Repeat step 20 until the desired result is obtained.
40. Click Save Setting to save all GUI setting to a *.mat file.
41. Click Load Setting to load a *.mat file to GUI setting.
42. Click ‘Exit’ button to exit from the Strain Interface v1.5 application.

3. Strain Interface v1.5 Change Log

```
1.5       - Put most used default ROI
1.4       - Avarege velocity in a ROI
1.3       - Add inteactive ROI selection
   - Calculate strain
1.0       - Forking from veloc11
11.10     - Add strain analysis feature
11.9      - split processing and ploting veloc vect

   - forced LS regression to estimate ROI track
11.8      - splitted ROI track processing and plotting

11.7      - using ROI as landmark instead of different region with offset

   - corrected anglOfset (vectors orientation) value
```

Appendix C

Vector Projection and Comparison

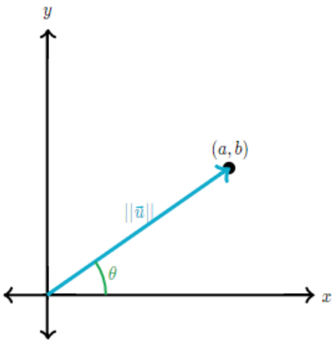

Illustration of a vector

1. A vector is characterized by magnitude and direction. The magnitude of a vector gives the length of the line segment, while the direction gives the angle the line forms with the positive x-axis. The magnitude of vector is usually written as |v|.
2. A particle velocity is an example of a vector.
3. Comparing velocity of two vectors (or more) is only possible if the direction is the same. If the directions are different, all vectors must be projected to the same direction so called ‘orientation’

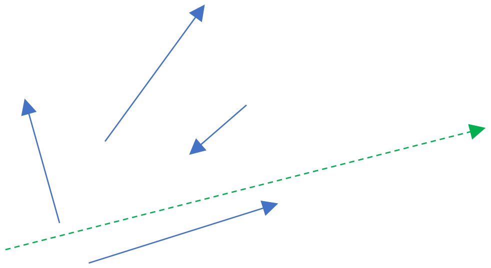

Velocity vectors in different directions

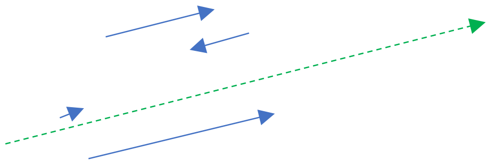

velocity vectors projected to a same direction

4. The vector projection of a vector a on a nonzero vector b, is the orthogonal projection of a onto a straight line parallel to b. The scalar projection of a on b is a scalar equal to $a_1 = \|\mathbf{a}\| \cos\theta,$, where θ is the angle between a and b. A scalar projection can be used as a scale factor to compute the corresponding vector projection.

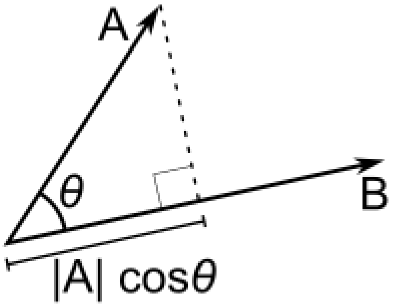

Projection of vector A to the direction of B

5. In the software, the projection direction of velocity vectors can be specified from ‘dir’ spinner of the UI. In our case,

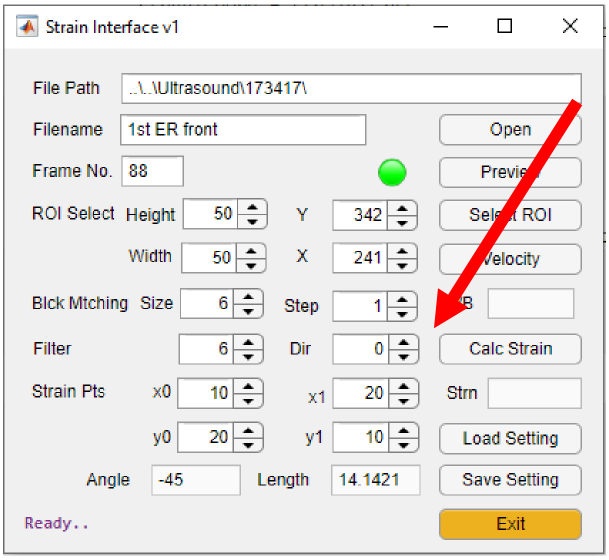

File Path ..\..\Ultrasound\173417\
Filename 1st ER front
Frame No. 88
ROI Select Height 50 Y 342
Width 50 X 241
Blck Mtching Size 6 Step 1 B
Filter 6 Dir 0
Strain Pts x0 10 x1 20 Strn
y0 20 y1 10
Angle -45 Length 14.1421
Ready..

‘dir’ spinner on the UI

6. In our software, 0° is motion to the right, 90° is down motion, -90 is up motion and 180 is motion to the left.

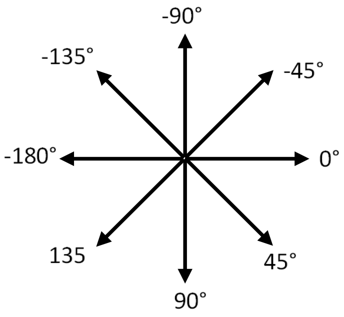

Angle of direction used in our software

Appendix D

Derivation of Pulsed Doppler for Sinusoid Velocity

Suppose a color Doppler imaging system is estimating a flow velocity of a propagating sine wave in a medium with packet size N = 4. For $-\pi/2 < \Delta\phi_i < \pi/2$, the estimated velocity is calculated by

$$\hat{v} = \frac{4c}{4\pi f_0 T_a}\tan^{-1}\left(\frac{I_{-2}Q_{-1} - I_{-1}Q_{-2} + I_{-1}Q_0 - I_0 Q_{-1} + I_0 Q_1 - I_1 Q_0 + I_1 Q_2 - I_2 Q_1}{I_{-1}I_{-2} + Q_{-1}Q_{-2} + I_0 I_{-1} + Q_0 Q_{-1} + I_1 I_0 + Q_1 Q_0 + I_2 I_1 + Q_2 Q_1}\right)$$

By trigonometric decomposition,

$$\hat{v} = \frac{4c}{4\pi f_0 T_a}\tan^{-1}\left(\frac{\sin(B - D)\cos(C - A) + \sin(D)\cos(C - Z)}{\cos(B - D)\cos(C - A) + \cos(D)\cos(C - Z))}\right) \quad ,$$

where

$$A = \phi_0 + \frac{4\pi f_0}{c}\xi_m \sin(\omega_b t + \phi_b)\cos\left(\omega_b \frac{T_a}{2}\right) \quad ,$$

$$B = \frac{4\pi f_0}{c}\xi_m \cos(\omega_b t + \phi_b)\sin\left(\omega_b \frac{T_a}{2}\right) \quad ,$$

$$C = \phi_0 + \frac{4\pi f_0}{c}\xi_m \sin(\omega_b t + \phi_b)\cos\left(\omega_b \frac{T_a}{4}\right) \quad ,$$

$$D = \frac{4\pi f_0}{c}\xi_m \cos(\omega_b t + \phi_b)\sin\left(\omega_b \frac{T_a}{4}\right) \quad \text{and}$$

$$Z = \phi_0 + \frac{4\pi f_0}{c}\xi_m \sin(\omega_b t + \phi_b) \quad .$$

If shear wave frequency is much smaller than PRF, the approximation is

$$\lim_{\frac{f_b}{PRF}\to 0}\frac{\cos C - A}{\cos C - Z} = \lim_{\frac{f_b}{PRF}\to 0}\frac{\cos\left(\frac{4\pi f_0}{c}\xi_m \sin(\omega_b t + \phi_b)\,(\cos\left(4\pi\frac{f_b}{PRF}\right) - \cos\left(2\pi\frac{f_b}{PRF}\right)\right)}{\cos\left(\frac{4\pi f_0}{c}\xi_m \sin(\omega_b t + \phi_b)\,(\cos\left(2\pi\frac{f_b}{PRF}\right) - 1)\right)}$$

$$= \frac{\cos\left(\frac{4\pi f_0}{c}\xi_m \sin(\omega_b t + \phi_b)\,(\cos(0) - \cos(0)\right)}{\cos\left(\frac{4\pi f_0}{c}\xi_m \sin(\omega_b t + \phi_b)\,(\cos(0) - 1)\right)} = 1 \quad .$$

In this condition, the velocity is approximated by

$$\hat{v} \cong \frac{4c}{4\pi f_0 T_a}\tan^{-1}\left(\frac{\sin B - D + \sin D}{\cos B - D + \cos D}\right)$$

$$\cong \frac{4c}{4\pi f_0 T_a} \tan^{-1} \tan\left(\frac{B - D + D}{2}\right)$$

$$\cong \frac{2c}{4\pi f_0 T_a} B \qquad . \tag{A1}$$

On the other hand,

$$\lim_{\frac{f_b}{PRF}\to 0} \frac{B}{D} = \lim_{\frac{f_b}{PRF}\to 0} \frac{\frac{4\pi f_0}{c} \xi_p \cos(\omega_b t + \phi_b) \sin\left(4\pi \frac{f_b}{PRF}\right)}{\frac{4\pi f_0}{c} \xi_p \cos(\omega_b t + \phi_b) \sin\left(2\pi \frac{f_b}{PRF}\right)}$$

$$= \lim_{\frac{f_b}{PRF}\to 0} \frac{2\cos\left(4\pi \frac{f_b}{PRF}\right)}{\cos\left(2\pi \frac{f_b}{PRF}\right)} = 2 \quad .$$

Therefore

$$D \cong \frac{B}{2} \quad .$$

In this approximation, the similar result is obtained by

$$\hat{v} \cong \frac{4c}{4\pi f_0 T_a} \tan^{-1}\left(\frac{\sin B - \frac{B}{2} \cos C - A + \sin \frac{B}{2} \cos C - Z}{\cos B - \frac{B}{2} \cos C - A + \cos \frac{B}{2} \cos C - Z)}\right)$$

$$\cong \frac{4c}{4\pi f_0 T_a} \tan^{-1}\left(\frac{(\cos C - A + \cos C - Z) \sin \frac{B}{2}}{(\cos C - A + \cos C - Z) \cos \frac{B}{2})}\right)$$

$$\cong \frac{2c}{4\pi f_0 T_a} B \quad . \tag{A2}$$

If packet size is reduced to N = 2 by removing second and fourth pulse from the calculation, the velocity estimation is

$$\hat{v} = \frac{2c}{4\pi f_0 T_a} \tan^{-1}\left(\frac{I_{-2} Q_0 - I_0 Q_{-2} + I_0 Q_2 - I_2 Q_0}{I_0 I_{-2} + Q_0 Q_{-2} + I_2 I_0 + Q_2 Q_0}\right)$$

$$= \frac{2c}{4\pi f_0 T_a} \tan^{-1}\left(\frac{2a \sin B\,(\sin A \sin Z + \cos A \cos Z)}{2a \cos B\,(\cos A \cos Z + \sin A \sin Z)}\right)$$

$$= \frac{2c}{4\pi f_0 T_a} \tan^{-1}(\tan B)$$

$$= \frac{2c}{4\pi f_0 T_a} B \qquad . \tag{A3}$$

If it is reduced further to a single packet size, leaving only first and last pulse on the calculation, the velocity estimation becomes

$$
\begin{aligned}
\hat{v} &= \frac{c}{4\pi f_0 T_a}\tan^{-1}\left(\frac{I_{-2}Q_2 - I_2Q_{-2}}{I_2I_{-2} + Q_2Q_{-2}}\right) \\
&= \frac{c}{4\pi f_0 T_a}\tan^{-1}\left(\frac{a^2 2\cos B\sin B}{a^2(\cos^2 B - \sin^2 B)}\right) \\
&= \frac{c}{4\pi f_0 T_a}\tan^{-1}\left(\frac{\sin 2B}{\cos 2B}\right) \\
&= \frac{2c}{4\pi f_0 T_a}B \qquad .
\end{aligned}
\tag{A4}
$$

This derivation implies that omitting the ultrasound pulse other than the first and the last signal does not affect the estimation of sinusoid flow velocity significantly.